Experimental Investigation of Seismic Velocity Dispersion in Cracked Crystalline Rock

by

Heather Schijns

A thesis submitted in partial fulfillment of the requirements for the degree of

Doctor of Philosophy

in

Geophysics

Department of Physics
University of Alberta

© Heather Schijns, 2014

Abstract

Seismic velocity dispersion in crystalline rock is investigated through experimental measurements on two natural quartzite specimens. The quartzites are thermally damaged to induce low aspect ratio cracks and the shear and Young's moduli are measured across a range of effective pressures, from 10-150 MPa, under dry, argon saturated and water saturated conditions. High frequency measurements (1 MHz) are made using the standard pulse transmission technique, while low frequency (0.01-1 Hz) shear measurements are made by forced torsional oscillation with the Australian National University apparatus. Low frequency Young's modulus measurements are made using the innovative forced flexural method. Dry moduli do not show significant differences between low and high frequency results. Stiffening of argon saturated moduli is observed at high frequency, however, the low amplitude means it is not possible to confirm dispersion when compared to low frequency measurements. Both water saturated specimens display substantial dispersion, particularly at lower effective pressures when crack porosity is higher. Experimental results from one of the quartzites are compared to Gassmann and a combination of Biot and squirt flow elastic theories. Experimental low frequency shear moduli are invariant to pore fluid saturation as predicted by Gassmann, and Biot and squirt flow theory accurately describes the high frequency argon saturated shear modulus of the quartzite. Neither theory, however, adequately describes the behaviour of the Young's modulus. The high frequency water saturated shear and Young's moduli of the quartzites are substantially stiffer than is predicted by theory.

Preface

Some of the research conducted for this thesis forms part of an international research collaboration between Dr. I. Jackson at the Australian National University and Dr. D.R. Schmitt at the University of Alberta. The body of the thesis and Appendix A are my original work.

Appendix B of this thesis has been published as I. Jackson, H. Schijns, D. R. Schmitt, J.J. Mu and A. Delmenico "A versatile facility for laboratory studies of viscoelastic and poroelastic behaviour of rocks," *Review of Scientific Instruments*, vol. 82, issue 6, 064501. I assisted with some of the data acquisition and analysis and contributed to manuscript edits. I. Jackson designed the technical apparatus and was responsible for the concept formation, manuscript composition, data acquisition and analysis. D.R. Schmitt assisted with the concept formation and manuscript edits. J.J. Mu and A. Delmenico contributed to the data analysis.

Acknowledgements

My supervisor Dr. Doug Schmitt and co-supervisor Dr. Ian Jackson introduced me to the idea of studying seismic dispersion for my doctoral research after I completed my master's degree in 2008. During my years of study I have had numerous opportunities to meet other people working in academia and industry, exchange ideas with them and gain close friends. I have had a chance to travel the world for conferences and the luck to work in some of the most stunning and unique places on the planet, all while pursuing my interest in seismic research. I am incredibly grateful to both of my supervisors for the experiences afforded to me.

Doug Schmitt spent countless hours teaching, mentoring and guiding me and always had time to discuss my research with me. Perhaps more importantly, he and Cheryl Schmitt were a constant source of encouragement during times when I struggled to find the motivation to continue with the project. I have shared a beer or two with Doug over the nine years I have worked with him as well as seismic adventures spanning three continents and five countries. I still learn something new every time I speak with him and hope I have caught even a small amount of the enthusiasm he brings to geophysics and to field work in particular. Ian Jackson welcomed me to Australia, and without his support and expertise the laboratory work in this thesis would not have been possible. He has been a source for reasoned, well thought out discussion throughout this research and for that I am appreciative.

Although I eventually left the university to gain a broader range of experience, while I was there my research was supported by numerous funding agencies. Without this financial support it would have been more difficult to pursue my interest in seismic methods. I am grateful for the funding I received from the Alberta Innovates – Technology Futures graduate scholarship, the University of Alberta Doctoral Prize of Distinction, the government of Alberta Queen Elizabeth II doctoral scholarship and the Natural Sciences and Engineering Research Council of Canada Alexander Graham Bell Canada doctoral scholarship and Michael Smith Foreign Study Supplement.

I surely wouldn't have lasted as long at the University of Alberta if I didn't have such great friends and colleagues there. Christine Dow, Hannah Mills, Lucas Duerksen, Andrew Fagan and Rebecca Feldman gave me great advice and assistance over the years, as well as fantastic company and good memories.

A lot of people have made small but important impacts along the way, and I feel privileged to know Lindsay Brouse, who is in more of my best memories than I can count, Ryan Daley, who was always ready for a dance party, Ryan Halton, who inspired me see what was waiting after Edmonton and Jackie Clarke, who was my partner in

crime for most of the adventures I had while I was still there. Jackie – let's never do karaoke again.

I am most thankful for the unfailing support, encouragement and understanding of my family.

In Vancouver, 30.07.14.

Heather Schijns

Table of Contents

List of tables

List of Figures

List of variables

A	wave amplitude, permeability rate constant
A_s	cross-sectional area
a	major crack axis
α	aspect ratio
b	polarization direction
C	elastic stiffness
c	minor crack axis
D	distance
d	displacement, thickness
Δ	Biot model term
E	Young's modulus
η	viscosity
ε	strain, crack density
f	frequency
Γ	Christoffel symbol
h	discretization length
I	moment of inertia
J	Hudson model term
K	Bulk modulus
κ	permeability
L	length
l	distance along beam
λ	Lamé parameter
M	bending moment
μ	shear modulus/second Lamé parameter
N	number density

n	directional unit vector
υ	Poisson ratio
ω	angular frequency
P	pressure, Biot model term
ϑ	volumetric proportion of a mineral
ϕ	porosity
Q	Biot model term
R	reaction force, radius of curvature, Biot model term
ρ	density
S	elastic compliance, storage capacity, normalized modulus
σ	stress
t	time
T	torque
τ	tortuosity
u	displacement
V	voltage
v	flexural displacement
v_P	P-wave velocity
v_S	S-wave velocity
x	position

1.0 Introduction

Seismology is a geophysical technique used to map the acoustic properties of the Earth at all scales. The seismic signal travels as a wave through the Earth; the velocity, attenuation and phase of the wave at the receiver can be used to measure the properties of the medium it travelled through. Seismic waves are sensitive to rock properties at a scale proportional to their wavelength. Low frequency teleseismic waves generated by earthquakes (<10 Hz) can provide information on the depth and composition of the Earth's mantle and core (e.g. Dziewonski and Anderson, 1981). Higher frequency seismic surveys, typically with artificially generated sources (~10-300 Hz) are used to map the structure of the crust (e.g. Hammer *et al.* 2010), or localized properties of an area at the ore deposit or oil field scale (e.g. Schijns *et al.* 2012). Sonic logging (kilohertz) can be used to measure properties at a still more localized borehole scale (e.g. Liner and Fei, 2006). Finally, ultrasonic measurements (megahertz) can be used to measure the seismic properties of core in the laboratory (e.g. Lassila *et al.* 2010).

It is often desired to compare localized seismic properties to a broader region, or vice versa. This is problematic, however, as much of the Earth's crust is anticipated to have fluid-filled fractures (Crampin and Lovell, 1991) and saturated cracks or pores in rock cause the rock to behave fundamentally differently depending on the frequency of the measurement. The behaviour of fluid within the rock is dependent on the timescale of the applied stress, or frequency of the propagating seismic wave. As the seismic waves sample the bulk properties of the rock, they are sensitive to the behaviour of

fluid within the rock. This dependence of seismic velocity on frequency is called dispersion.

1.1 Motivation

Joint interpretation of seismic measurements acquired at different frequencies is a common occurrence (e.g. De *et al.*, 1994, Lüschen *et al.*, 1996, Dey-Barsukov *et al.*, 2000, Smithson *et al.*, 2000, Prioul and Jocker, 2009, Elbra *et al.*, 2011), but in order for it to be sucessful it is necessary to account for dispersion. The problem is a well known one within the geophysical community, and numerous theoretical models have been developed to allow an estimation of the effects of fluid saturation and frequency of measurement on seismic properties (e.g. Gassmann, 1951, Biot, 1956, Geertsma and Smit, 1961, Walsh, 1965, Kuster and Toksoz, 1974, O'Connell and Budiansky, 1974, Hudson, 1981, Schoenberg, 1980). Very few dispersion measurements have been acquired, however, and the theoretical models largely remain unconstrained experimentally. The accuracy of the models is therefore poorly known and it is currently not possible to gauge the uncertainty in predicted dispersion for a given rock type or frequency regime.

In order to avoid effects of heterogeneity, it is necessary to make dispersion measurements in the laboratory on core scale samples through which an ultrasonic wave can propagate. The lack of widespread dispersion measurements remains an unsolved problem as a result of the difficulty of making low frequency measurements on

such small specimens. Low frequency measurements require extremely specialized equipment and only a very few laboratories worldwide currently have this capability.

1.2 Content

This thesis seeks to partially address the lack of experimental constraint on dispersion models through seismic dispersion measurements on two natural, cracked quartzite samples and subsequent comparison to theoretical models. The thesis begins with a theoretical review of elastic wave theory and some popular theoretical dispersion models. A literature review of the experimental work completed to date follows in Chapter Two.

The third chapter of the thesis includes a characterization of the physical properties of the two quartzite specimens used in the study, with an examination of the mineralogy, porosity, permeability and crack shape and distribution within the samples. The chapter presents shear modulus measurements across a range of frequencies to allow quantification of dispersion in the shear modulus and shear-wave velocity of the quartzites. The shear modulus measurements are compared to theoretical models and predictions.

The Young's modulus chapter, Chapter Four, introduces the newly adapted low frequency flexural measurement apparatus of the Australian National University (ANU). As the apparatus had not previously been used to make flexural measurements, the calibration process for the low frequency measurements is documented prior to the presentation of Young's modulus dispersion measurements on the two quartzites. With

the acquisition of two independent elastic moduli, it was possible to conduct a more thorough comparison of experimental data with theoretical predictions. This comparison is included within the chapter as well.

Chapter Five summarizes and reaches conclusions about the dispersion measurements and their relationship with current theory. Future work is proposed to continue with the study of experimentally measured dispersion. Each chapter is intended to be somewhat capsular in nature which results in some limited repetition of key concepts, ideas and background.

Two appendices are included within the thesis; pulse transmission measurement is a relatively commonly used technique that is not documented within the body of the thesis, but which nonetheless forms an important component of the dispersion measurements contained herein. Appendix A comprises a description of the ultrasonic pulse transmission technique used to make high frequency measurements in the laboratory. The low frequency measurements are more specialized as the ANU apparatus is unique. Numerous low frequency torsional measurements have been acquired historically and the technique is well described by numerous scientific papers (Jackson *et al.*, 1984, Jackson and Paterson, 1993), but the low frequency flexural measurements are a new adaptation of the apparatus. Appendix B describes the apparatus and method, and presents some of the earlier work on fused quartz which demonstrates the technique's viability.

Although this thesis focuses on measurements of seismic velocity dispersion, significant work has been completed during the course of these studies on seismic

velocity anisotropy, including a refereed paper (Schijns *et al.* 2012) and numerous extended abstracts (Schijns *et al.*, 2009a, Schijns *et al.*, 2009c, Schijns *et al.*, 2009d, Schijns *et al.*, 2010, Schijns *et al.*, 2013). In addition, further extended abstracts have been published on contributions to work in hard rock seismology, including zero offset vertical seismic profiles (VSP) and reflection seismic profiles across the Outokumpu, Finland volcanogenic massive sulphide deposit (Duo *et al.*, 2009, Duo *et al.*, 2010, Heinonen *et al.*, 2009) and the New Zealand Alpine fault (Kovacs *et al.*, 2011).

2.0 Background

This thesis presents velocity dispersion measurements made on two low porosity quartzite specimens with thermally induced low aspect ratio microcracks. This chapter serves as a qualitative and quantitative introduction to the topic of seismic velocity dispersion. The causes of dispersion and theoretical models are described, in addition to methods of measuring dispersion and a summary of some of the previous work on this topic. Finally, a brief outline of the dispersion study undertaken is presented.

2.1 Elastic wave theory

Exploration seismology is an important geophysical technique commonly used to map the subsurface. In its simplest form, seismic waves produced by a source at surface travel downwards until they are reflected back up to the surface at a lithological boundary. Various types of seismic receivers (accelerometers, geophones, seismometers) on the surface record the motions of the ground in response to the arriving seismic waves. The traveltime of the seismic wave from source to receiver is interpreted from these seismic records; this time is converted to a depth to a lithological boundary with knowledge of the wave velocity.

There are two types of seismic body waves: the P- and the S-wave. Both are linearly polarized in an isotropic medium. Measurements of both body waves, when combined with measurement of the rock density, allow the rock to be described in terms of its elastic moduli. The P-wave is the first arriving wave, and travels as a

longitudinal mode wave with the particles oscillating in the direction of propagation. Exploration geophysics predominantly makes use of the P-wave; since it is the first arriving wave its signal is undistorted by superposition with other seismic waves. The S-wave is a transverse wave, with particles oscillating perpendicular to the direction of propagation. The S-wave is made up of two perpendicular components. In an isotropic earth, seismologists consider the SV-wave to travel with particle motions in the vertical plane, and the SH-wave to travel with motions in the horizontal plane. In an isotropic medium the SV- and SH-waves travel at the same speed and arrive simultaneously.

The velocity of a seismic wave is governed by the bulk density of the rock and the rock's effective elastic stiffness modulus. The elastic stiffness, C_{ijkl}, relates stress, σ, and strain, ε, as illustrated by Hooke's Law using the Einstein summation convention (Auld, 1973):

$$\sigma_{ij} = C_{ijkl}\varepsilon_{kl} \qquad \text{i,j,k,l=1,2,3} \qquad (2.1)$$

The infinitesimal strain can be described by

$$\varepsilon_{kl} = \frac{1}{2}\left(\frac{\partial u_k}{\partial x_l} + \frac{\partial u_l}{\partial x_k}\right), \qquad \text{k,l=1,2,3} \qquad (2.2)$$

and combined with the time derivative of the equation for linear momentum

$$\frac{\partial \sigma_{ij}}{\partial x_j} = \rho \frac{\partial^2 u_i}{\partial t^2} \qquad \text{i,j=1,2,3} \qquad (2.3)$$

to give the full elastic wave equation:

$$\rho \frac{\partial^2 u_i}{\partial t^2} - \frac{\partial}{\partial x_j}\left[\frac{1}{2} C_{ijkl}\left[\frac{\partial u_k}{\partial x_l} + \frac{\partial u_l}{\partial x_k}\right]\right] = 0. \qquad \text{i,j,k,l=1,2,3} \qquad (2.4)$$

Here *u* is displacement, *x* is position, ρ is rock density and *t* is time. Symmetries within C_{ijkl}, where:

$$C_{ijkl} = C_{jikl} = C_{ijlk} = C_{klij}, \qquad \text{i,j,k,l=1,2,3} \qquad (2.5)$$

allow the reduction of Equation 2.4 to:

$$\rho \frac{\partial^2 u_i}{\partial t^2} - \frac{\partial}{\partial x_j}\left[C_{ijkl} \frac{\partial u_k}{\partial x_l} \right] = 0 . \qquad \text{i,j,k,l=1,2,3} \qquad (2.6)$$

If *u* can be described by harmonic oscillation,

$$u_i = A b_i \exp\left[i\omega \left(\frac{n_j}{|v|} x_j - t \right) \right], \qquad \text{i,j=1,2,3} \qquad (2.7)$$

where *A* is the wave amplitude, *b* the polarization direction, ω the angular frequency and *v* the velocity, the equations can be combined to yield a system of linear equations:

$$\left(C_{ijkl} n_j n_l - \rho v^2 \right) b_k = 0 . \qquad \text{i,j,k,l=1,2,3} \qquad (2.8)$$

The variable *n* is a direction cosine. If, and only if, the determinant of the coefficient matrix is zero, the solution is non-trivial. This allows seismic velocities to be related to the elastic stiffness using the Christoffel equations

$$\det \begin{vmatrix} \Gamma_{11} - \rho v^2 & \Gamma_{12} & \Gamma_{13} \\ \Gamma_{21} & \Gamma_{22} - \rho v^2 & \Gamma_{23} \\ \Gamma_{31} & \Gamma_{32} & \Gamma_{33} - \rho v^2 \end{vmatrix} = 0 \qquad (2.9)$$

where Γ is the Christoffel symbol, with $\Gamma_{ij} = C_{ijkl} n_j n_l$. The symmetry of the elastic stiffness tensor ensures that Γ is both symmetric and real, and the determinant results in three

distinct phase velocities, the P-wave and two S-waves. Further, the symmetries in *C* mean that, while as a fourth order tensor *C* has 81 variables, only 21 of these are independent. This allows C_{ijkl} to be represented as a 6 x 6 matrix, C_{IJ}, in Voigt notation. The indices of elastic stiffness relate to each other as (Nye, 1985):

ij, kl =	11	22	33	23,32	31,13	12,21
I, J =	1	2	3	4	5	6

This indices relationship holds for the elastic stiffness and the stress, but a factor of two is introduced in some of the strains when moving to Voigt notation:

$$\sigma_I = \begin{bmatrix} \sigma_{11} \\ \sigma_{22} \\ \sigma_{33} \\ \sigma_{23} \\ \sigma_{31} \\ \sigma_{12} \end{bmatrix} \qquad \text{I=1,2,3 … 6} \qquad (2.10)$$

$$\varepsilon_J = \begin{bmatrix} \varepsilon_{11} \\ \varepsilon_{22} \\ \varepsilon_{33} \\ 2\varepsilon_{23} \\ 2\varepsilon_{31} \\ 2\varepsilon_{12} \end{bmatrix} \qquad \text{J=1,2,3 … 6} \qquad (2.11)$$

$$C_{IJ} = \begin{bmatrix} C_{1111} & C_{1122} & C_{1133} & C_{1123} & C_{1131} & C_{1112} \\ C_{2211} & C_{2222} & C_{2233} & C_{2223} & C_{2231} & C_{2212} \\ C_{3311} & C_{3322} & C_{3333} & C_{3323} & C_{3331} & C_{3312} \\ C_{2311} & C_{2322} & C_{2333} & C_{2323} & C_{2331} & C_{2312} \\ C_{3111} & C_{3122} & C_{3133} & C_{3123} & C_{3131} & C_{3112} \\ C_{1211} & C_{1222} & C_{1233} & C_{1223} & C_{1231} & C_{1212} \end{bmatrix} \qquad \text{I,J=1,2,3 … 6} \qquad (2.12)$$

It is important to note that the Voigt representation, C_{IJ}, only represents a fourth order tensor, and does not itself transform as a second order tensor. The notation does, however, simplify the notation of some of the relationships. Using the Voigt representations of the stress, σ, strain, ε, and elastic stiffness, C, tensors defined in Equations 2.10 through 2.12, Hooke's law can be simplified:

$$\begin{bmatrix} \sigma_1 \\ \sigma_2 \\ \sigma_3 \\ \sigma_4 \\ \sigma_5 \\ \sigma_6 \end{bmatrix} = \begin{bmatrix} C_{11} & C_{12} & C_{13} & C_{14} & C_{15} & C_{16} \\ C_{21} & C_{22} & C_{23} & C_{24} & C_{25} & C_{26} \\ C_{31} & C_{32} & C_{33} & C_{34} & C_{35} & C_{36} \\ C_{41} & C_{42} & C_{43} & C_{44} & C_{45} & C_{46} \\ C_{51} & C_{52} & C_{53} & C_{54} & C_{55} & C_{56} \\ C_{61} & C_{62} & C_{63} & C_{64} & C_{65} & C_{66} \end{bmatrix} \begin{bmatrix} \varepsilon_1 \\ \varepsilon_2 \\ \varepsilon_3 \\ \varepsilon_4 \\ \varepsilon_5 \\ \varepsilon_6 \end{bmatrix} \tag{2.13}$$

In the case of an isotropic medium, the velocities of the two S-wave components will be equal and the elastic stiffness requires only two physical moduli to describe it. In terms of the shear modulus, μ, and the Young's modulus, E, the elastic stiffness can be defined as:

$$C_{IJ} = \begin{bmatrix} \frac{\mu(4\mu - E)}{(3\mu - E)} & \frac{\mu(E - 2\mu)}{(3\mu - E)} & \frac{\mu(E - 2\mu)}{(3\mu - E)} & 0 & 0 & 0 \\ \frac{\mu(E - 2\mu)}{(3\mu - E)} & \frac{\mu(4\mu - E)}{(3\mu - E)} & \frac{\mu(E - 2\mu)}{(3\mu - E)} & 0 & 0 & 0 \\ \frac{\mu(E - 2\mu)}{(3\mu - E)} & \frac{\mu(E - 2\mu)}{(3\mu - E)} & \frac{\mu(4\mu - E)}{(3\mu - E)} & 0 & 0 & 0 \\ 0 & 0 & 0 & \mu & 0 & 0 \\ 0 & 0 & 0 & 0 & \mu & 0 \\ 0 & 0 & 0 & 0 & 0 & \mu \end{bmatrix} \quad \text{I,J=1,2,3…6} \tag{2.14}$$

As the complexity of the symmetry of the elastic stiffness and its inverse, the elastic compliance, S, increase, more independent parameters are required to describe the tensor. Transversely isotropic (TI), also known as hexagonal, symmetry requires 5

independent parameters, while 9 are required for orthorhombic symmetry (Nye, 1985). The shear and Young's moduli can be used to determine other important physical moduli and physical parameters including the bulk modulus, *K*, the Poisson ratio, υ, and the first Lamé parameter, λ:

$$K = \frac{\mu E}{3(3\mu - E)} \tag{2.15}$$

$$\upsilon = \frac{E}{2\mu} - 1 \tag{2.16}$$

$$\lambda = \frac{\mu(E - 2\mu)}{3\mu - E} \tag{2.17}$$

The shear modulus, μ, is also known as the second of the two Lamé parameters. These moduli relate back to the P-wave velocity, v_P, and the S-wave velocity, v_S. In an isotropic case:

$$v_P = \sqrt{\frac{\lambda + 2\mu}{\rho}} = \sqrt{\frac{K + \frac{4}{3}\mu}{\rho}} = \sqrt{\frac{\left(\frac{\mu(4\mu - E)}{3\mu - E}\right)}{\rho}} \tag{2.18}$$

$$v_S = \sqrt{\frac{\mu}{\rho}} \tag{2.19}$$

In this thesis the materials were assumed to be mechanically isotropic and hence only two independent elastic moduli were required to describe their behaviour. This is a common assumption in geophysics and is valid for rocks which have minimal aligned cracks, shape or lattice preferred orientation of mineral grains or layering which could

cause anisotropy. Depending on the situation, calculations in this thesis variously employ the Young's modulus, *E*, that relates the ratio of the extensional stress to the extensional strain in a uniaxial stress state,

$$\sigma_{33} = E\varepsilon_{33}, \qquad \sigma_{11} = \sigma_{22} = \sigma_{12} = \sigma_{23} = \sigma_{13} = 0 \qquad (2.20)$$

the shear modulus, μ, which defines the ratio of the shear stress to the shear strain

$$\sigma_{ij} = 2\mu\varepsilon_{ij}. \qquad i \neq j \qquad (2.21)$$

and the bulk modulus, *K*, that essentially defines the relationship between applied pressure or stress and the volumetric change of the material,

$$\sum_{i=1}^{3} \frac{1}{3}\sigma_i = K \sum_{i=1}^{3} \varepsilon_i . \qquad (2.22)$$

The effective elastic stiffness, and therefore seismic velocity through a rock, is strongly affected by the presence of any fractures or cracks. Fluid-filled cracks can cause seismic velocity dispersion, while aligned cracks can additionally cause seismic velocity anisotropy.

2.2 Velocity dispersion

Velocity dispersion refers to the dependence of seismic wave speeds on the frequency of the seismic wave. Seismic velocity measurements are made in a variety of different ways, including passive and active source in-situ seismic, sonic well logs and laboratory measurements. These techniques offer different geophysical insights, and, while it is often desirable to jointly interpret the velocity measurements, comparison is complicated not only by differences in the scale of measurement, but also by

differences in the frequencies used in each method. Passive source seismic is often measured in the millihertz to hertz range, active source seismic in the hertz range, sonic logs in the kilohertz range and laboratory measurements in the megahertz range, with the possibilities spanning nine decades in frequency. While this range in frequency is not expected to have much effect on dry or unfractured rocks, much of the Earth's crust is expected to have fluid-filled fractures that remain open from from deviatoric stress (Crampin and Lovell, 1991). Stress is comprised of a hydrostatic component and a deviatoric component, with deviatoric stress causing distortion of the rock and the accompanying dilation of cracks. The behaviour of fluid within rock pores and fractures is extremely frequency dependent when exposed to the stress of a seismic signal and must be considered when comparing measurements made at different frequencies.

Pore fluids can contribute to the stiffness of a saturated rock and thereby alter the seismic properties of the rock. The behaviour of the pores can be described by one of three regimes (Fig. 2.1): i) saturated isolated, ii) saturated isobaric or iii) drained (O'Connell and Budiansky, 1977). Specifically, these regimes are defined by

i) The high frequency "saturated isolated" regime describes a situation where the viscosity of the pore fluid and the frequency of the acoustic wave are high enough that the pore fluid is not able to flow out of the pore space on the timescale of measurement. This regime is also referred to as "unrelaxed," and laboratory-based ultrasonic measurements conducted on core samples typically fall into this regime.

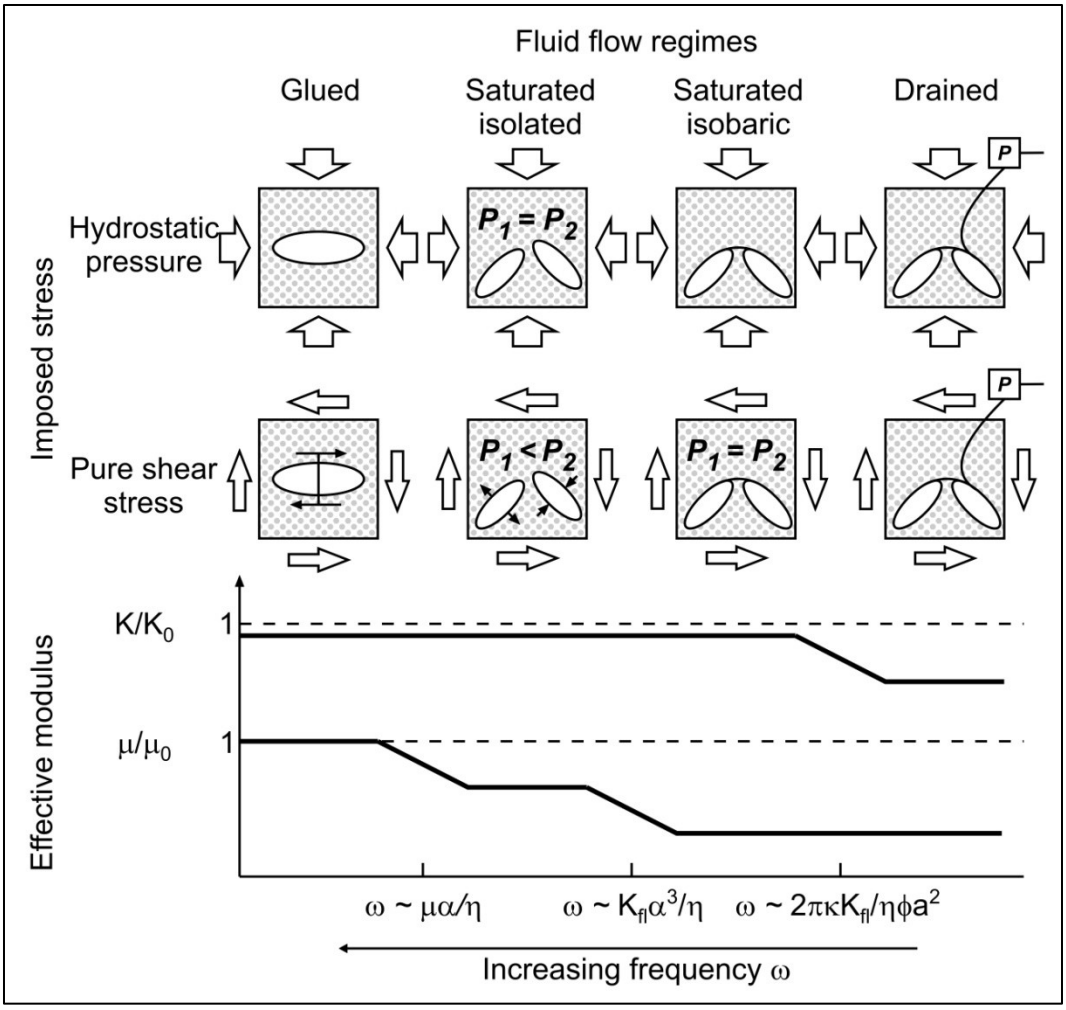

Figure 2.1: Fluid-flow regimes and effective elastic moduli for cracked, fluid saturated rocks (O'Connell and Budiansky, 1977). The upper panels show the response of the crack to hydrostatic (top row) and shear (second row) pressure, while the lower graphs show the expected bulk and shear modulus behaviour in each regime as a function of angular frequency, ω. P_1 and P_2 are the pore pressures in the cracks, with their relationship depending on fluid flow regime and crack orientation. This figure has been modified and reproduced from Figure #1 of the Geological Society of Australia Special Publication Number 17, The Australian Lithosphere, edited by B. Drummond, 1991, page 86, the Petrophysical Basis for the Interpretation of Seismological Models for the Continental Lithosphere, by Ian Jackson, with permission from the Geological Society of Australia Inc.

ii) The mid-range frequency "saturated isobaric" regime describes the behaviour of the pore fluid when sufficient time is allowed for the flow of the pore fluid to eliminate any pressure gradients between pores. While the pores experience isobaric pressure, the timescale is too short to allow bulk migration of the fluid out of the region of interest. Most active-source in-situ seismic and passive source teleseismic measurements are expected to fall into this regime.

iii) The very low frequency "drained" regime is unlikely to occur on the timescales of experimental geophysical measurements. In this regime the rock essentially undergoes consolidation: the pore fluid flows out of the pores and out of the region of interest. While both the "saturated isobaric" and "drained" regimes could be termed "relaxed," the term is usually used to indicate the former regime since most low frequency measurements fall into this regime rather than the latter.

In the transition zone between regimes the pore fluid may display some aspects of both regimes involved. Of course, in the above the transition frequency between high and low will shift from rock type to rock type depending on numerous factors affecting the timescale of fluid flow, including porosity, permeability, fluid viscosity and tortuosity.

2.3 Theoretical Background

If velocity dispersion is present in a rock, it is necessary to estimate the magnitude of the dispersion in order to allow joint interpretation across data sets comprised of measurements at different frequencies. Theoretical modelling is commonly used to

estimate the elastic properties of a rock under different measurement conditions. While most minerals have well characterized elastic moduli, this cannot be the case for all rocks, due to the virtually unique composition of one rock to another. At their most basic, the models allow the estimation of the elastic moduli of rocks if their composition is known. More complex models allow the estimation of the effects of the integration of cracks, pores and fluids into the rock matrix. Ultimately, these models can be used to estimate the magnitude of dispersion and can contribute to successful comparison of measurements made at different frequencies.

2.3.1 Effective media theory

Theoretical models of the effects of cracks on the physical moduli of rocks must, by necessity, make numerous approximations. Rocks are rarely composed of a single mineral and the problem of determining the moduli of the background rock must be addressed before the inclusion of any cracks or fractures into the model. Voigt (1928) and Reuss (1929) first estimated the elastic moduli of polycrystalline aggregates by averaging the elastic stiffnesses and compliances, respectively, of the component minerals. The Voigt average is the equivalent of assuming a boundary condition of uniform strain,

$$C^V = \sum_{i=1}^{N} \vartheta_i C_i , \tag{2.23}$$

while the Reuss average assumes uniform stress at the boundary,

$$C^R = \left[\sum_{i=1}^{N} \frac{\vartheta_i}{C_i} \right]^{-1} , \tag{2.24}$$

where N is the number of minerals present and ϑ is the volumetric proportion of each mineral.

Hill (1952) showed that these two methods form the upper and lower boundaries on the moduli. Hashin and Shtrikman (1962, 1963) developed bounds on the elastic moduli of aggregates which are much closer together and which are not limited by the assumption that the anisotropy of the constituent mineral crystals is small. When there are only two constituents, the Hashin-Shtrikman bounds are:

$$K^{HS} = K_1 + \frac{\vartheta_2}{(K_2 - K_1)^{-1} + \vartheta_1\left(K_1 + \frac{4}{3}\mu_1\right)^{-1}} \tag{2.25}$$

$$\mu^{HS} = \mu_1 + \frac{\vartheta_2}{(\mu_2 - \mu_1)^{-1} + 2\vartheta_1(K_1 + 2\mu_1)/\left[5\mu_1\left(K_1 + \frac{4}{3}\mu_1\right)\right]}. \tag{2.26}$$

The upper and lower bounds are computed by interchanging the index of the two constituents, where K_1 and μ_1 belong to one constituent, and K_2 and μ_2 to the other.

The Voigt-Reuss-Hill and Hashin-Shtrikman formulations are simply bounds on the expected solid mixture's properties. They can, of course, be applied to cracked minerals but the results, particularly for the shear properties, are not very useful if we want to understand the physics of the fluid motions induced by deformation; more sophisticated approaches that incorporate some of the geometry of the pore space must be used. These attempts to model cracked media mostly by the introduction of an inclusion using one scheme or another are briefly reviewed here.

Effective media theory for cracks is predicated on the assumption that the problem is in the limit where seismic waves are large compared to the size of the inclusions in a rock; the seismic wave does not "see" the inclusions individually, and the elastic stiffness of a rock with inclusions can be replaced by an effective elastic stiffness that is representative of the properties of the media as a whole. MacKenzie (1950) assumed an isotropic and homogeneous host rock and developed approximations for the effective bulk and shear moduli of a rock with dry spherical pores. Eshelby (1957) extended this theory to ellipsoidal pores. Walsh (1965a) examined the elastic stiffness of dry penny-shaped cracks and ellipsoidal cracks in uniform strain and in uniform stress. Walsh (1965a) found that the differences between regimes of uniform strain and hydrostatic stress are negligible and for the most part can be ignored, however, uniaxial compression causes significant differences in the Young's modulus compared with hydrostatic compression due to frictional sliding between crack faces (Walsh, 1965b). These initial theoretical forays made use of the non-interaction approximation (NIA), which requires the cracks to be sufficiently 'dilute' (i.e. far enough apart) that any interactions between the cracks are minimal. The accuracy of the NIA assumption continues to be debated (e.g. Grechka and Kachanov, 2006b, Saenger *et al.*, 2004). In one attempt to overcome this problem, O'Connell and Budiansky (O'Connell and Budiansky 1974, 1977, Budiansky and O'Connell 1976) used a self-consistent method where an approximation of crack interaction was accounted for; additionally they developed solutions for fully and partially saturated isolated cracks. Their solution is appropriate for the high-frequency regime due to the isolated nature of the cracks.

2.3.2 Theoretical models of velocity dispersion

A theoretical model of the behaviour of saturated fluids at low frequency had previously been developed by Gassmann (1951). Gassmann's relation is one of the most commonly used theories to predict the effects of saturation, or of fluid substitution within a saturated rock:

$$K_{sat} = K_{dry} + \frac{\left(1 - K_{dry}/K_0\right)^2}{\phi/K_{fl} + \left(1-\phi\right)/K_0 - K_{dry}/K_0^2} \tag{2.27}$$

where K_{sat} is the bulk modulus of the saturated rock, K_{dry} is the modulus of the dry rock with no pore fluids, K_0 is the modulus of the constituent mineral of the rock, K_{fl} is the bulk modulus of the pore fluid, and ϕ is the porosity of the rock. The theory requires the shear modulus to be invariant to saturation, which is widely held to be true at low frequencies:

$$\mu_{sat} = \mu_{dry} \tag{2.28}$$

Gassmann's equation assumes fluid is able to flow between pores on the timescale of a half-seismic wavelength and that pore pressure is therefore in equilibrium throughout the rock. For this reason, it is generally held in the geophysical community that the theory performs best for low frequency seismic wave propagation in the Earth below about ~200 Hz. Gassmann theory further assumes that the rock is seismically isotropic and is composed of a single mineral. Brown and Korringa (1975) expanded on Gassmann's equation to allow for mixed mineralogy. Neither the formulations of Gassmann nor of Brown and Korringa assume that the shear modulus remains unchanged upon saturation of the rock, however Berryman (1999) demonstrated that

the constant shear modulus tenet is intrinsic to the theory and is a result of the derivation. In fact, this assumption may not always hold. In some real cases, the shear modulus is not always static between dry and saturated conditions. Baechle *et al.* (2009) experimentally measured that water saturation causes weakening of the shear modulus in some carbonates which results in poor predictions of saturated P- and S-wave velocities by Gassmann theory; such saturation effects on the shear modulus are examples of a chemical mineral-fluid interaction occurring, which violates the theoretical assumption of an invariant shear modulus.

Biot (1956) developed a model to predict frequency dependent velocities of saturated rocks. In the low frequency limit Biot's theory reduces to Gassmann's equation. In the high frequency limit, the equations (in the notation of Johnson and Plona (1982)) give v_p and v_s as:

$$v_P = \left[\frac{\Delta \pm \left[\Delta^2 - 4\left(\rho_{11}\rho_{22} - \rho_{12}^2\right)\left(PR - Q^2\right)\right]^{\frac{1}{2}}}{2\left(\rho_{11}\rho_{22} - \rho_{12}^2\right)} \right]^{\frac{1}{2}} \tag{2.29}$$

$$v_S = \left[\frac{\mu_{dry}}{\rho - \phi\rho_{fl}\tau^{-1}} \right]^{\frac{1}{2}} \tag{2.30}$$

$$\Delta = P\rho_{22} + R\rho_{11} - 2Q\rho_{12} \tag{2.31}$$

$$P = \frac{\left(1-\phi\right)\left(1-\phi-K_{dry}/K_0\right)K_0 + \phi K_0 K_{dry}/K_{fl}}{1-\phi-K_{dry}/K_0 + \phi K_0/K_{fl}} + \frac{4}{3}\mu_{dry} \tag{2.32}$$

$$Q = \frac{\left(1-\phi-K_{dry}/K_0\right)\phi K_0}{1-\phi-K_{dry}/K_0 + \phi K_0/K_{fl}} \tag{2.33}$$

$$R = \frac{\phi^2 K_0}{1 - \phi - K_{dry} / K_0 + \phi K_0 / K_{fl}} \tag{2.34}$$

$$\rho_{11} = (1 - \phi)\rho_0 - (1 - \tau)\phi\rho_{fl} \tag{2.35}$$

$$\rho_{22} = \phi\tau\rho_{fl} \tag{2.36}$$

$$\rho_{12} = (1 - \tau)\phi\rho_{fl} \tag{2.37}$$

$$\rho = \rho_0(1 - \phi) + \rho_{fl}\phi \tag{2.38}$$

where μ_{dry} is the shear modulus of the dry rock, ρ_0 is the mineral density, ρ_{fl} is the pore fluid density and τ is the tortuosity (≥1). As a result of the multiple solutions to the equation for the P-wave velocity (Eq. 2.29), Biot theory predicts a slow P-wave as well as the regular, fast P-wave. This Biot slow-wave has been observed in the laboratory (Johnson and Plona, 1982, Bouzidi and Schmitt, 2009), but has yet to be observed in-situ. Biot theory assumes attenuation results only from the motion of the pore fluid with respect to the solid rock. When viscous effects within the fluid are accounted for, a slow S-wave is derived in addition to the slow P-wave (Sahay, 2008).

Biot theory assumes cylindrical pores, but in crystalline rocks, where the pore space is more predominantly composed of low aspect ratio cracks and fractures, Biot dispersion is typically not the dominant form of dispersion and it is often necessary to account for 'squirt dispersion' as well. Mavko and Jizba (1991) derived equations to predict the effect of squirt dispersion on the moduli of saturated rocks at high frequency, K_{uf} and μ_{uf}:

$$\frac{1}{K_{uf}} \approx \frac{1}{K_{dry-hP}} + \left[\frac{1}{K_{fl}} - \frac{1}{K_0}\right]\phi_{soft} \tag{2.39}$$

$$\left[\frac{1}{\mu_{uf}} - \frac{1}{\mu_{dry}}\right] = \frac{4}{15}\left[\frac{1}{K_{uf}} - \frac{1}{K_{dry}}\right] \tag{2.40}$$

where ϕ_{soft} is the amount of porosity that closes at high pressure and $K_{dry\text{-}hP}$ is the bulk modulus of the dry rock at high pressure. Generally, both Biot and squirt dispersion must be considered; K_{uf} and μ_{uf} are usually substituted into the Biot equations for K_{dry} and μ_{dry} to account for both fluid saturation effects.

The theories can be combined to account for both squirt flow and Biot dispersion at high frequency by substituting the high frequency saturated moduli calculated using squirt-flow theory into the Biot equations. Good estimates of v_P and v_S in saturated rocks can be obtained by using the combined results of Biot's and Mavko and Jizba's theories, however; it can also be useful to determine whether Biot or squirt dispersion is the dominant effect within the rock as this will affect the characteristic frequency which marks the transition from a high to low frequency regime for pore fluid behaviour. Biot gives the characteristic frequency, f_B, as:

$$f_B = \frac{\eta\phi}{2\pi\kappa\rho_{fl}} \tag{2.41}$$

where η is the viscosity of the pore fluid and κ is the permeability.

The above Biot and squirt flow relations are appropriate for high frequency, but the Biot characteristic frequency can be used to approximate velocities at lower frequencies as well. Geertsma and Smit (1961) developed approximations for Biot's

relations at low and middle frequencies. In the Geertsma and Smit approximation, the P-wave velocity is related to the high frequency Biot P-wave velocity, $v_{P\text{-}hf}$, and low frequency Biot-Gassmann P-wave velocity, v_{P0}, with the frequency, f, and characteristic Biot frequency:

$$v_P = \frac{v_{P-hf}^4 + v_{P0}^4 \left(f_B / f\right)^2}{v_{P-hf}^2 + v_{P0}^2 \left(f_B / f\right)^2} . \tag{2.42}$$

The characteristic frequency for squirt flow differs from that for Biot dispersion, and depends on the aspect ratio, α, of the crack. For squirt flow, O'Connell and Budiansky (1977) give the characteristic frequency as

$$f_{OB} = \frac{K_{dry}\alpha^3}{2\pi\eta} . \tag{2.43}$$

Cracks are commonly approximated to be ellipsoidal in shape, and are then described by their aspect ratio c/a, where a is the length of the two equal semi-axes of the ellipsoid, and c is the length of the third axis, the axis of rotational symmetry (Douma, 1988). As viscosity figures in both equations, if the rocks being studied can be saturated with fluids of different viscosities in the laboratory, the characteristic frequency should vary either directly or inversely with fluid viscosity and thereby allow the determination of the principle cause of dispersion within the rock.

Due to the assumption of cylindrical pores, Biot theory may not be appropriate for low aspect ratio cracks. In these cases, a self-consistent approximation such as that derived by O'Connell and Budiansky (1974, 1977) may yield better results. The self-consistent approximation uses the mathematical solution for the deformation of a single ellipsoidal inclusion and extends it to multiple inclusions by approximating the crack

interactions through the replacement of the background medium with an as-yet unknown effective medium. O'Connell and Budiansky derived an effective Young's modulus, *E**, and shear modulus, μ*:

$$\frac{E^*}{E_0} = 1 - \frac{16}{45}\frac{(1-\upsilon^*)(10-3\upsilon^*)}{(2-\upsilon^*)}\varepsilon \tag{2.44}$$

$$\frac{\mu^*}{\mu_0} = 1 - \frac{32}{45}\frac{(1-\upsilon^*)(5-\upsilon^*)}{(2-\upsilon^*)}\varepsilon, \tag{2.45}$$

where E_0 and μ_0 are the moduli of the uncracked rock, ε the crack density and υ^* the effective Poisson ratio. In order to calculate the effective Young's and shear moduli, it is necessary to first solve for the effective Poisson ratio by relating it back to the crack density and Poisson ratio of the uncracked rock:

$$\varepsilon = \frac{45}{16}\frac{(\upsilon-\upsilon^*)(2-\upsilon^*)}{(1-\upsilon^{*2})(10\upsilon-3\upsilon\upsilon^*-\upsilon^*)}. \tag{2.46}$$

In rocks with dilute cracks, alternate effective media models such as the Hudson (1981) model may be applicable as well. Hudson calculated a first order approximation of the changes to the effective elastic stiffness tensor, *C*, as well as attenuation, resulting from dry and saturated penny-shaped cracks within an otherwise isotropic host:

$$C_{IJ} = C^0_{IJ} + C^1_{IJ}. \qquad \text{I,J=1,2,3,...,6} \tag{2.47}$$

Here C^0 is the isotropic background matrix and C^1 is the first order correction term for the introduction of cracks. Hudson solved for a variety of crack conditions and orientation, but the most applicable for this thesis is the correction for randomly oriented fluid filled cracks. Hudson calculated Lamé parameters, λ_1 and μ_1, which can

be used to solve for E_1 (Eq. 2.17) and substituted into the isotropic elastic stiffness formulation (Eq. 2.14) to give C^1:

$$\mu_1 = -\frac{32}{15} N a^3 \mu \left(\frac{\lambda + 2\mu}{3\lambda + 4\mu} \right) \tag{2.48}$$

$$\lambda_1 = -\frac{2}{3} \mu_1 \tag{2.49}$$

where N is the number density of cracks and a is the crack radius of the penny shaped cracks, linking the correction factor to the number and shape of cracks within the rock. The Lamé parameters λ and μ are from the uncracked nonporous rock.

Hudson model is limited by requiring a low crack density, as crack interactions are not accounted for, and performs best for low aspect ratio cracks. Most metamorphic rocks, which commonly have low aspect ratio cracks, are good candidates for the model. The model has since been extended to include second order crack interaction (Hudson, 1986) and intrinsic anisotropy of the host rock (Hudson, 1994), and remains a relatively popular model.

Schoenberg's (1995) model adds the effect of cracks in elastic compliance to obtain an effective elastic compliance, S:

$$S_{IJ} = S^0_{IJ} + S^1_{IJ} \qquad \text{I,J=1,2,3,...,6} \tag{2.50}$$

where S^0 is the intrinsic compliance of the rock and S^1 is the additional compliance caused by cracks. The authors show that the compliance tensor of a rotationally invariant set of cracks can be determined from the normal, Z_N, and tangential, Z_T, compliance of the cracks (in Voigt notation):

$$S^1 = \begin{bmatrix} Z_N & 0 & 0 & 0 & 0 & 0 \\ 0 & 0 & 0 & 0 & 0 & 0 \\ 0 & 0 & 0 & 0 & 0 & 0 \\ 0 & 0 & 0 & 0 & 0 & 0 \\ 0 & 0 & 0 & 0 & Z_T & 0 \\ 0 & 0 & 0 & 0 & 0 & Z_T \end{bmatrix} \quad (2.51)$$

While this approach is more flexible in that it does not require the cracks to be ellipsoidal in shape or of low aspect ratio, the crack compliance tensor can still be related to the geometry of penny-shaped cracks (Schoenberg and Douma, 1988). Hudson's and Schoenberg's models yield relatively similar results for saturated cracks, but Schoenberg's model has been shown to be superior for dry cracks (Grechka and Kachanov, 2006a).

Biot and squirt flow theory have been expanded upon numerous times to formally combine Biot and squirt dispersion (Dvorkin and Nur, 1993), account for flow between pores and cracks (Chapman *et al.*, 2002) as well as account for anisotropic rocks (Mukerji and Mavko, 1994); numerous other inclusion models exist, such as Brown and Korringa (1975) and Kuster Toksöz (1974). None of these models can yet be considered 'standard' models. The difficulties in measuring velocity dispersion mean that few experimental measurements exist with which to constrain theoretical models.

2.4 Experimental Results

2.4.1 Experimental work in velocity dispersion

There are several approaches to experimentally quantifying dispersion effects. Some research has focused on measuring the elastic properties of the cracks

themselves. The compliance of any cracks or fractures is a necessary input into models like Schoenberg (1980) and this research allows separation of the elastic properties of the cracks and fluid flow effects. Lubbe *et al.* (2008) and Worthington and Lubbe (2007) measured high frequency dry and saturated crack compliances which could be input into theoretical models. They found a correlation between fracture size and compliance for a given aspect ratio and determined that the ratio of normal to tangential compliance is less than was commonly assumed theoretically for gas-filled cracks. Pyrak-Nolte *et al.* (1990) examined the transmission of seismic waves across single natural fractures and quantified the frequency dependent stiffness and attenuation of the cracks. Interestingly, they found that in order to account for their experimental results it was necessary to model the cracks as having a specific viscosity significantly in excess of the viscosity of the saturating fluid, in addition to the more expected necessity of specifying a specific stiffness, indicating that the fundamental behaviour of the cracks themselves may be frequency dependent. Crack compliances on the whole, however, remain largely unconstrained experimentally.

Crack compliance measurements yield important information on crack behaviour, but still require integration with theoretical models to provide values for the effective elastic properties of cracked rocks necessary for seismic interpretation. A more straightforward constraint on theoretical models is direct measurement of effective elastic stiffness. Most such work is laboratory based out of necessity, but some work continues to be done in the field. Low frequency in-situ measurements are on the scale of kilometres, while high frequency ultrasonic measurements are usually made on centimetre scale core samples. Since geological formations are rarely homogeneous

over these large differences in scale it can be difficult to make accurate measurements of velocity dispersion using direct comparison. Field measurements do, nonetheless, provide evidence of dispersion as well as some insights and constraints. Field based studies, such as Sams *et al.* (1997) and Schmitt (1999), usually compare some combination of ultrasonic measurements on core samples from a borehole, sonic logging at kilohertz frequencies and vertical seismic profiles (VSP) at frequencies on the order of 10-100 Hz. Both Sams *et al.* and Schmitt measured dispersion in porous, saturated rocks; Sams *et al.* quantified the observed dispersion as a ~20% increase in the P-wave velocity at high frequency for their experimental site.

Ideally, heterogeneity issues can be eliminated by making measurements on the same sample at both high and low frequencies to avoid scale effects. In practice, ultrasonic waves undergo significant scattering due to their wavelength typically being on the order of the size of the rock's mineral grains or any cracks or pores. It is difficult to propagate ultrasonic waves through more than a few centimetres of rock due to the resulting loss of energy. Avoiding heterogeneity issues therefore requires making low frequency measurements on core samples. High frequency measurements are relatively straightforward on core samples and are commonly made by propagating seismic waves through the sample using piezoelectric transducers in the ultrasonic pulse transmission technique. Developing an apparatus that can measure low frequency elastic moduli of core samples is, however, difficult as a result of the sensitivity of the moduli to strain (e.g. Iwasaki *et al.*, 1978). In order to make measurements comparable to exploration seismic wave propagation, it is necessary to make low frequency measurements on samples at seismic strain amplitudes of ~10^{-7} or less (Batzle *et al.*, 2006). The basic

experimental methods to make low frequency and low strain amplitude measurements are resonance and forced deformation, but it is a challenge to make such small strain measurements.

In the resonance technique long narrow samples are sinusoidally driven into resonant vibration, and the moduli are then determined by the frequency of the resonance. Some of the first laboratory-based low frequency measurements were collected using this technique (Murphy, 1984, Tittmann *et al.*, 1984, Winkler and Nur, 1979, Winkler, 1986). The forced deformation technique, meanwhile, applies very small amplitude stresses to deform the sample in torsion, flexure or axially. The small deformations mean that extremely sensitive measurements must be made, usually with capacitive, magnetic or optical transducers (Batzle *et al.*, 2006). Jackson *et al.* (1984), Peselnick *et al.* (1979), Spencer (1981) and Batzle *et al.* (2006) have conducted some of the first work using this stress-strain method.

As a result of the difficulty in acquiring low frequency measurements on core samples, relatively few dispersion measurements have been made to date, and only a handful of laboratories worldwide are able to work on this. Historically, most have focused on rocks with relatively high porosity and spherical pores. Spencer (1981) reported Young's modulus dispersion in saturated sandstones and limestones across a frequency range of 4-400 Hz. More recently, Adam *et al.* (2009) measured bulk and shear modulus dispersion in carbonates from 10-1000 Hz and David *et al.* (2013) measured bulk modulus dispersion in sandstone samples from 0.02-0.1 Hz. Characterization of porosity distribution is not always simple, and Adelinet *et al.* (2010) measured dispersion in basalt with bimodal porosity composed of both equant pores

and of low aspect ratio cracks. The authors measure the bulk modulus at frequencies 0.01-0.1 Hz and at 1 MHz. Adam and Otheim (2013) characterized bulk and shear modulus dispersion in a basalt with both cracks and vesicles at frequencies 2-300 Hz and at 0.8 MHz. Murphy (1984) provided rare dispersion measurements in a low porosity cracked rock, measuring 5% dispersion in a microcracked granite from 2-7 kHz. Recently, Madonna and Tisato (2013) built a new apparatus for low frequency Young's modulus measurements and completed measurements on Berea sandstone from 0.01-100 Hz.

2.5 Study Overview

Very little experimental research has been conducted on seismic wave propagation in low porosity fractured rock, with the result that the applicability of the necessarily simplified theoretical models remains unknown. There is a necessity to acquire further experimental observations of dispersion in rocks with low aspect ratio cracks, and to assess which, if any, theoretical models are best able to predict observed effects of fluid saturation on these cracked rocks. Models typically make numerous assumptions: the most common are that the frame of the rock is an isotropic, homogeneous medium of known elastic moduli, and that inclusions are evenly distributed. Often, random orientation of the cracks or pores is assumed as well.

Two natural quartzite specimens were selected for the study and low aspect ratio cracks were induced in both samples. The petrophysical properties of the samples were characterized using numerous techniques including SEM and mercury porosimetry, however, timescales of fluid flow and hence dispersion is largely controlled by sample

permeability and fluid viscosity. The permeability of the samples was comprehensively measured across a range of effective pressures, and the elastic moduli were measured with two saturating fluids of differing viscosity, as well as dry. The samples were measured while fully saturated with either argon (viscosity of 0.025 mPa·s at a pressure of 10 MPa and temperature of 20°C) or water (viscosity of 1 mPa·s) pore fluid. The shear and Young's modulus of the samples were measured using ultrasonic pulse transmission across a range of effective pressures and under the different saturating conditions. In order to measure dispersion, low frequency measurements were made using unique equipment (Fig. 2.2) from Australian National University (ANU). Shear modulus measurements were made using torsional forced oscillation (Jackson *et al.*, 1984) and Young's modulus measurements were made with flexural forced oscillation (Jackson *et al.*, 2011) under similar pressures and saturation conditions as the high frequency measurements. The flexural method is an innovative method, and the calibration and measurement methods are described in detail.

An important component of experimental measurement is a comparison with theoretically predicted results. As indicated previously, numerous theoretical models exist and it is not reasonable to compare results with all of them. Commonly used models include Gassmann (1951), Biot (1956) and squirt-flow (Mavko and Jizba, 1991); all the terms in these models were well characterized experimentally for the quartzites and most modeling of the experimental results focused on comparing to the dispersion in the moduli to these theories. In addition, however, some limited aspects of Hudson theory (1981) and the self-consistent theory of O'Connell and Budiansky (1977) relating to characterizing crack density and fluid flow behaviour were examined.

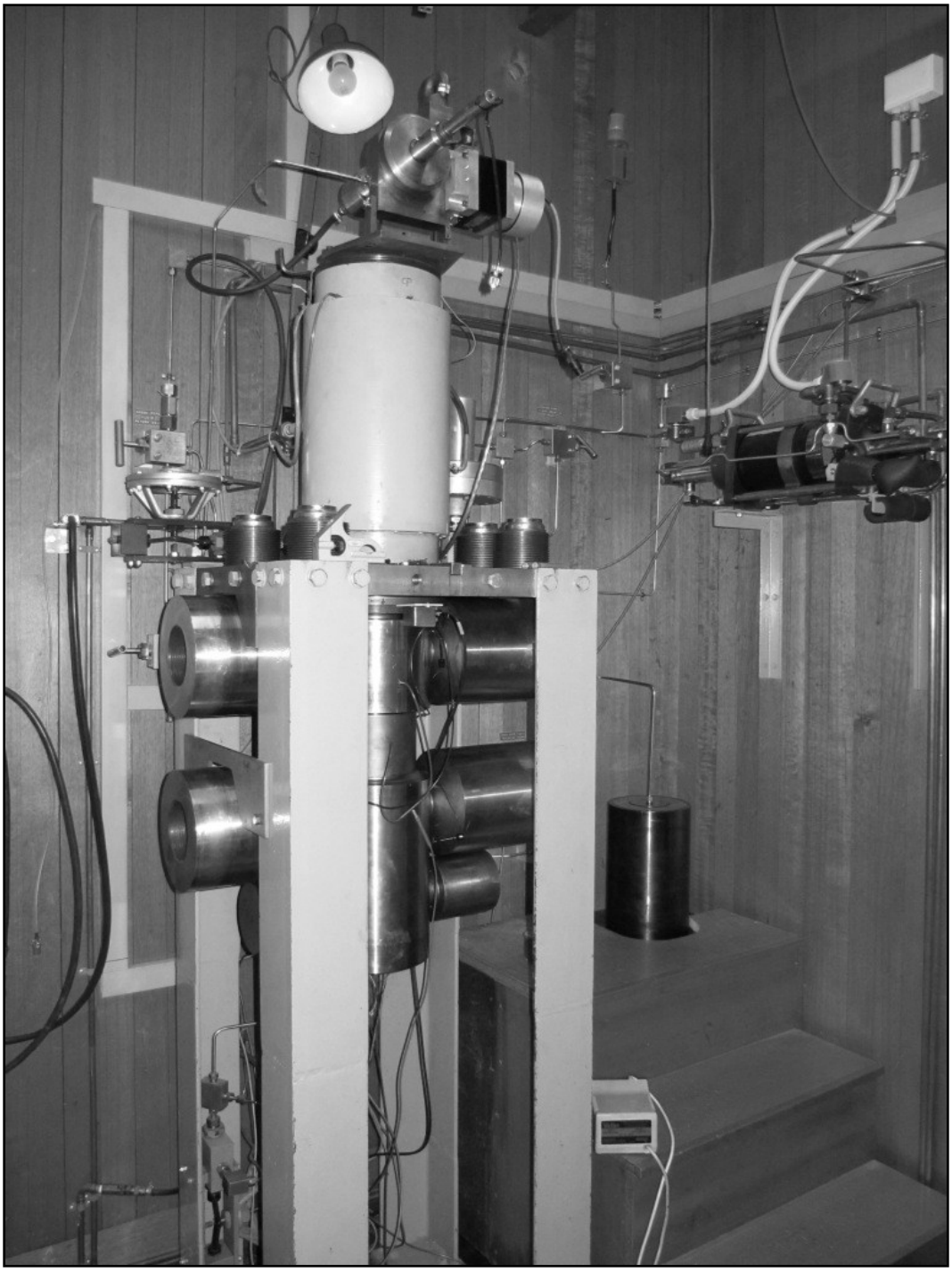

Figure 2.2: Forced oscillation pressure vessel at Australian National University for 0.001-1 Hz shear and Young's modulus measurements.

3.0 Shear Modulus Dispersion

3.1 Introduction

Seismic methods are among the principal tools used in oil and gas exploration, and are commonly used in environmental and engineering studies. Increasingly, the applicability of seismic methods in other areas, such as CO_2 sequestration monitoring and mineral exploration, is being investigated. Numerical modeling of rock acoustic properties can give an indication of the likelihood of successfully imaging subsurface features not historically targeted using seismic methods, however, these physical properties are typically measured in the laboratory or in a borehole.

One complication is that the seismic wave speeds used to do this can depend on frequency. Laboratory or borehole measurements of the acoustic properties of rock in mega- and kilohertz range, respectively, can be subject to seismic velocity dispersion when compared to exploration seismic surveys (typically 10-300 Hz). At high frequencies, when the timescale of measurement is such that fluid does not have sufficient time to flow between pores and cracks, the pores and cracks effectively act as if they are isolated from each other. If the pore fluid is relatively incompressible, this inability to engage in stress-induced flow results in a stiffening of the elastic moduli of the saturated rocks at higher frequencies. Numerous theories have been developed to quantify the magnitude of velocity dispersion that can be expected between different frequency regimes, but experimental measurements with which to constrain these theories are more limited. Due to the prevalent usage of seismic methods in oil and gas exploration, studies have frequently focused on rocks with higher porosities or more equant pores (Adam *et al.*, 2009, Batzle *et al.*, 2006, Spencer, 1981, Winkler and Nur,

1982, Yin *et al.*, 1992). The geometry of the porosity, however, has a significant effect on the amount of dispersion expected: the effect of spherical pores on the overall compressibility of the rock is correlated to the porosity, while bulk compressibility caused by low aspect ratio cracks is correlated to the rate of change of porosity with pressure. At low porosities spherical pores therefore have only a small effect, while highly compressible cracks can still significantly affect the moduli of the rock (Walsh, 1965a). As seismic methods becomes more commonly used in crystalline rocks (e.g. Hajnal *et al.*, 2010, Heinonen *et al.*, 2013, Koivisto *et al.*, 2012, Malehmir *et al.*, 2012, Milkereit *et al.*, 1996, Schijns *et al.*, 2009b, White and Malinowski, 2012), which typically exhibit these low aspect ratio cracks, the importance of quantifying the dispersion caused by cracks increases. However, there have been very few direct experimental observations of dispersion in low porosity rocks with low aspect ratio cracks.

In this study, the shear modulus dispersion of cracked quartzite specimens from Cape Sorell, Australia and Alberta, Canada were measured over the frequency range 0.01-1 Hz and at 1 MHz when the samples were dry, argon saturated and water saturated. The mineralogy of the quartzites was examined using XRD and SEM analysis, while the grain sizes and induced cracks were characterized using thin sections and mercury porosimetry. Additionally, permeability as a function of pressure was measured for a comprehensive quantification of the properties of the quartzite. Dispersion measurements were made at effective pressures of 10-150 MPa to investigate the effects of crack closure.

3.2 Characterization of rock specimens

Two quartzite specimens, one from Cape Sorell, Tasmania, Australia and one from Alberta, Canada were selected for their relative homogeneity and near mono-minerallic nature. In order to aid in understanding the effect of fluid-filled porosity on bulk elastic properties of the rock it was necessary to characterize the matrix material as well as the shape, volume and connectivity of the pore space as thoroughly as possible. Therefore, the samples were characterized using scanning electron microscope (SEM), thin sections, mercury porosimetry, and, for the Alberta quartzite, x-ray diffraction (XRD). Permeability measurements as a function of pressure were also undertaken for both samples.

3.2.1 Density measurements

Both specimens are dominated by quartz grains of ~0.5 mm diameter. The Cape Sorell specimen (Fig. 3.1) is translucent light grey in appearance, and has been shown to be more than 99% quartz by volume, with <1% muscovite at the grain boundaries (Lu and Jackson, 1998). XRD and SEM confirmed that the Alberta quartzite, by comparison, is composed of quartz grains with a thin film of iron oxide at the grain boundaries (Fig. 3.2). The appearance of the Alberta quartzite appears to largely be controlled by the iron; initially the quartzite was an opaque brown-beige colour, but upon heating the sample to induce crack porosity the quartzite changed to a pale pink colour, indicating oxidization of the iron. The volumes of the quartzites were calculated from dimensional measurements made using vernier calipers on the thermally cracked precision ground samples. The sample mass and mercury porosimetry derived porosity were used in conjunction with the measured volume to calculate a grain density of 2708±7 kg/m^3 for

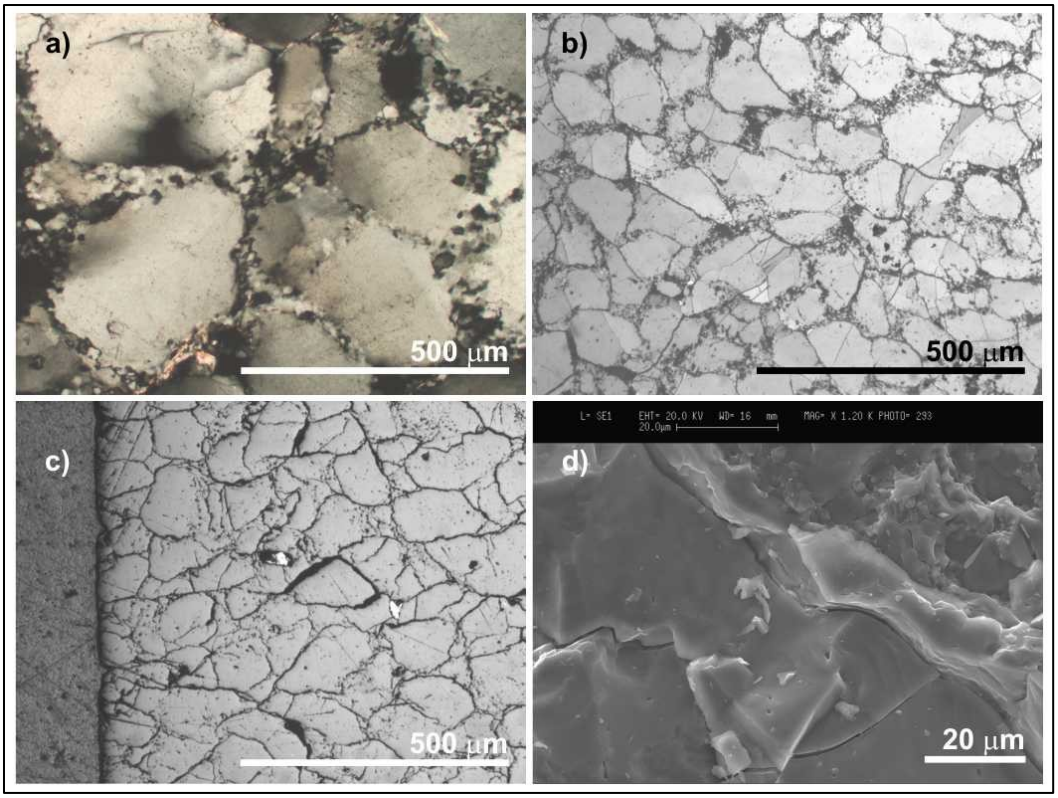

Figure 3.1: Thin section image of the Cape Sorell quartzite under transmitted light with cross polarized filter prior to thermal cracking (a), with transmitted light after thermal cracking (b), with reflected light showing a cross-section of the edge of the core sample after thermal cracking (c) and SEM image of the quartzite after (d) thermal cracking. The muscovite at the grain boundaries is clearly seen in (a), while the relatively random distribution of cracks can be seen in (b) and (c).

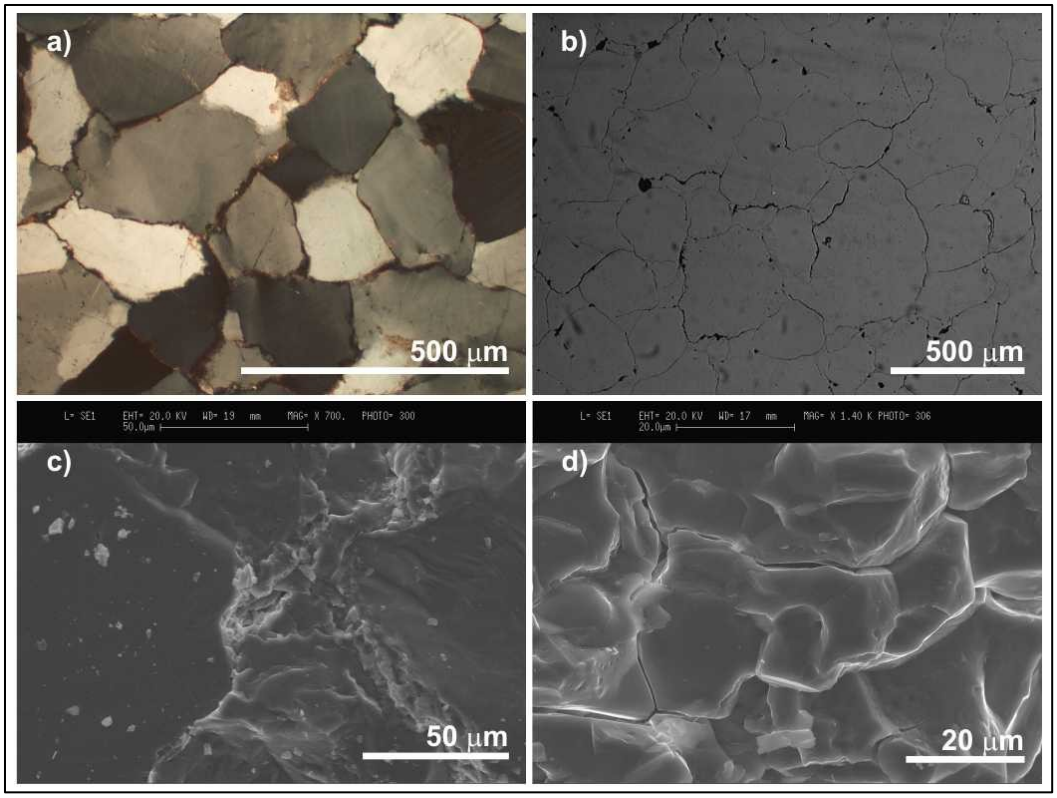

Figure 3.2: Alberta quartzite thin section with transmitted light and cross-polarized filter (a) and reflected light (b), as well as SEM image (c) prior to thermal cracking as well as SEM image after thermal cracking (d). The iron oxide film at grain boundaries is particularly evident in (a) while the low aspect ratio nature of the cracks is highlighted in (d).

the Cape Sorell quartzite; the Alberta sample was measured to have a grain density of 2659±7 kg/m^3. The Alberta sample grain density calculated by dimensional measurement agrees with the grain density measured by mercury porosimetry, 2664 kg/m^3, within error. Mercury porosimetry for the Cape Sorell quartzite, however, returned a grain density of 2644 kg/m^3; similar to the grain density of 2637 kg/m^3 measured by Lu and Jackson (1998) using Archimedes principle but ~2% different from that obtained through caliper measurement here. This small discrepancy may be indicative of local heterogeneity in the porosity or mineralogy of the measured Cape Sorell samples. Comparatively, Smyth and McCormick (1995) measured the x-ray density of pure quartz to be 2648 kg/m^3, similar to the results for both quartzites, again indicating that the quartzites are relatively pure. The quartz dominated mineralogy of the two samples simplifies comparison between experimental and theoretical results.

3.2.2 Porosity measurements

Thin section images of the quartzites showed that they initially did not have significant crack porosity (Figs. 3.1, 3.2); saturating with distilled water in a vacuum measured an initial porosity of 0.3% in the Cape Sorell quartzite (Lu and Jackson, 1998), and mercury porosimetry measured 0.8% initial porosity in the Alberta quartzite. In order to increase the crack porosity and thereby increase the signal to noise of any measurement of dispersion effects in the samples it was necessary to induce additional cracks. The low frequency forced oscillation measurement of the shear modulus used in this study is particularly sensitive to cracks at the outer diameter of a cylindrical sample, as the applied torque of the forced oscillation is related to the shear modulus through the moment of inertia and is therefore proportional to the radius raised to the fourth

power. Meanwhile, the ultrasonic pulse transmission method used for the high frequency measurement is more sensitive to cracks in the centre of the sample as the piezoelectric sources are centred on the axis of the sample. Comparison between measurements of the two frequency regimes would be further complicated by an anisotropic distribution of cracks, and it was therefore desirable to induce a crack distribution as uniformly distributed and as randomly oriented as possible in the quartzites. Both quartzite samples were heated to 1100°C, and then the Cape Sorell quartzite was quenched in liquid nitrogen while the Alberta quartzite was quenched in water. Mercury porosimetry confirmed that this increased the porosities of the samples to 2.3% and 2.4%, respectively. Thin section images showed that the treatment caused significant cracking of the specimens (Figs. 3.1, 3.2), while achieving a relatively isotropic crack distribution with fairly random crack orientation. Mercury porosimetry showed that the low aspect ratio cracks exhibit little variation in pore throat diameter, with a distribution of pore throat sizes centred around 0.4 μm and 0.7 μm, respectively, for each quartzite (Fig. 3.3). SEM images confirmed in a more qualitative sense that the low aspect ratio cracks display little variation in size.

3.2.3 Permeability measurements

Permeability measurements were made on the specimens using the ANU Australian National University) forced oscillation apparatus (Lu and Jackson, 2006). The apparatus allows the independent monitoring and adjustment of pore fluid pressure at either end of a cylindrical sample; when the pressure is increased or decreased in one of the pore fluid reservoirs, the change in pressure with time of the other reservoir can be monitored to measure permeability within the sample using the transient-flow method.

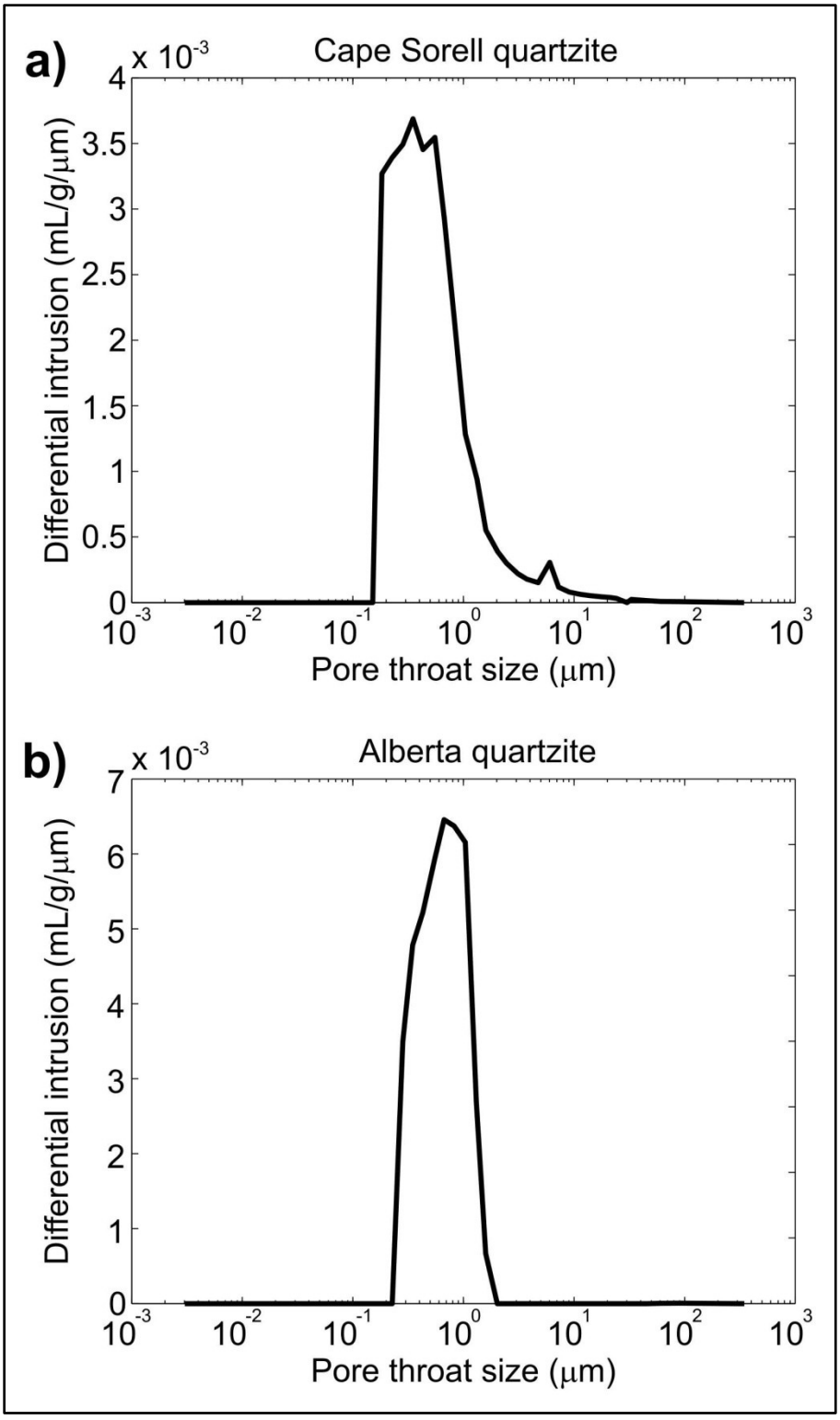

Figure 3.3: Mercury porosimetry of the Cape Sorell and Alberta quartzites shows that the cracks are distributed around a single pore throat size for each quartzite, 0.4 and 0.7 μm, respectively.

In principle, when a state of uniform fluid pressure, P_0, is established throughout both pore pressure reservoirs and the sample, the permeability, κ, and storage capacity of the sample can be measured by perturbing the system by a small pressure increment, ΔP, in the upper reservoir and measuring the decay or growth (depending if loading or unloading measurements are being undertaken) of pressure (Neuzil *et al.*, 1981). In the case of the quartzites, however, the storage capacity of the samples themselves is sufficiently small compared to the capacity of the upper and lower pore pressure reservoirs, S_u and S_d. This allowed permeability to be obtained using the approximation of Hsieh *et al.* (1981) for negligible storage capacity (Lu and Jackson, 2006):

$$\frac{\left(P(t)-P_0\right)}{\Delta P}=\frac{\left[S_u+S_d\exp(-At)\right]}{S_u+S_d} \tag{3.1}$$

where

$$A=\frac{\kappa A_s}{\eta L_S S_u}\left(1+\frac{S_u}{S_d}\right) \tag{3.2}$$

Here A_s is the cross-sectional area of the sample, L_s is the length of the sample, $P(t)$ is the pressure of the upper reservoir and η is the viscosity of the fluid. The ANU apparatus originally only allowed argon gas as a pore fluid but has recently been modified to additionally allow condensed liquid pore fluids such as water (Jackson et al., 2011). As the equation assumes that the fluid properties are constant over the induced pressure gradient, permeability measurements were made when the quartzites were saturated with water rather than argon. Over the pressure increments used the

physical properties of water showed very little change and an approximation of constant properties is reasonable. Equation 3.1 can be rearranged to:

$$\ln\left[\frac{(P(t)-P_0)(S_u+S_d)}{\Delta P S_d}-\frac{S_u}{S_d}\right]=-At \qquad (3.3)$$

Equation 3.3 can be graphed in order to find the slope (*-A*), allowing an experimental measurement of the permeability κ.

Measurements were made by enclosing the specimen in an annealed copper jacket and collapsing the jacket under high effective pressure. In practice this was done with no pore pressure in the system and a confining pressure of >80 MPa. This caused the copper jacket to mold closely to the outside of the sample, preventing fluid flow at the jacket-specimen boundary. Under confining pressure the lower reservoir, with volume 40 000 mm^3 (Lu, 1996), was then pressurized with water and the water was allowed to flow to the upper reservoir (volume 1163 mm^3) until the pressures in each reservoir equilibrated and the specimen was fully saturated. The pore fluid flowed into and out of the 15 mm diameter samples via an opening with diameter 2 mm. Pressure measurements in each reservoir were made using high pressure transducers (Precise Sensors, model 114) with a resolution of 0.1 mV/10 V (equivalent to about 0.02 MPa at the maximum pore pressure used, 150 MPa), which were calibrated against a Bourdon-tube (Heise) pressure gauge. The data was recorded digitally using LabView software (National Instruments) and a multichannel acquisition card. Permeability measurements were then taken by changing the pore pressure in the upper reservoir and monitoring the growth or decay of pressure. It was sometimes necessary to adjust the pressure in the upper or lower reservoir in the middle of this decay/growth in order

to achieve appropriate final effective pressures for the shear modulus measurements; in these instances the data during and after this mid-measurement adjustment was not used in determining the permeability, reducing the overall measurement time. A least-squares fit, constrained to pass through the origin, over the time from the initial adjustment until either equilibrium was reached or the pressures were further manually adjusted, was applied to the data and the permeability was calculated (Fig. 3.4). Only one permeability measurement was made at each reported effective pressure due to time constraints.

Measuring the timescale of pressure equilibration between the two reservoirs by fluid flow through the sample served the dual purpose of allowing a measurement of permeability and ensuring that pore pressure within the sample was equilibrated prior to the commencement of forced oscillation measurements. Further, the required equilibration time was used as a guide to ensure pore pressure was constant throughout the sample prior to the acquisition of any high frequency measurements as well.

3.3 Method

3.3.2 Low frequency measurements

Low frequency measurements (0.01-1 Hz) were made using the ANU forced oscillation apparatus in torsional mode (Jackson et al., 1984, Jackson and Paterson, 1993). The apparatus consists of a long, thin beam which is fixed at one end and free at the other, where it is sinusoidally twisted by a pair of opposing electromagnetic drivers. The cylindrical core sample (15 mm x 150 mm), sandwiched between two polycrystalline

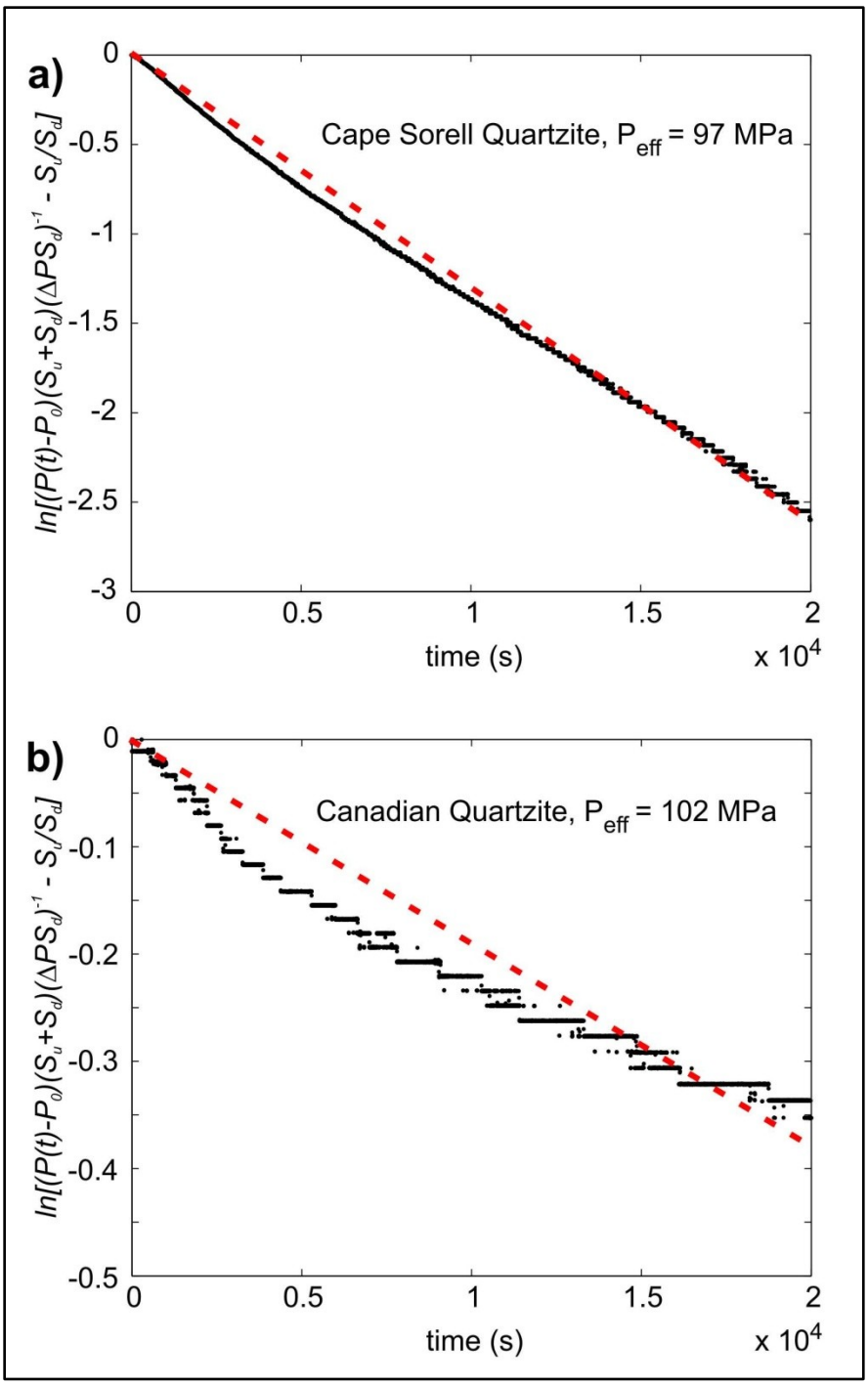

Figure 3.4: Measure of permeability (from Equation 3.4) over nearly 6 hours for the Cape Sorell (a) and Alberta (b) quartzites at ~100 MPa of effective pressure. Note the different y-axis scales in (a) and (b). Measurements of the low permeability (1.16 x 10^{-21} m^2 at this pressure) of the Canadian quartzite are approaching the resolution limit of the pore-pressure transducers as evidenced by the digitization noise apparent in the data. Lines of best fit shown as red dashed lines.

(Duramic) alumina rods and encased in a 0.5 mm thick annealed copper jacket, was placed in the top of the apparatus, above a hollow steel elastic standard. Torsional mode displacements were measured at two locations along the beam: one immediately below the sample, but above the elastic standard, and one below both the sample and the elastic standard. Measurements of the angular displacement caused by the applied force from the electromagnetic drivers were made using parallel plate capacitors mounted at the end of lever arms for mechanical advantage (Fig. 3.5). The measured angular displacement, d_1, above the elastic standard and below the specimen assembly is related to the applied torque, T_0, by the equation

$$d_1 = \frac{D_1 T_0}{\mu_A I_A} \sin(\omega t - \delta) \tag{3.4}$$

where D is the radial length of the parallel plate capacitors from the axis of the beam, ω is the angular frequency, δ is the loss angle, t is the time, μ_A is the shear modulus of the specimen assembly comprised of the copper jacket, alumina rods and quartzite and I_A is the polar moment of inertia of the specimen assembly. Here, the shear modulus of the assembly and the loss angle are unknown; the radial distance is measured and the moment of inertia is calculated from vernier caliper measurements of the specimen assembly. The angular displacement below both the specimen assembly and above the elastic standard, d_2, is measured to determine the magnitude of the applied torque:

$$d_2 = \frac{D_2 T_0}{\mu_S I_S} \sin(\omega t). \tag{3.5}$$

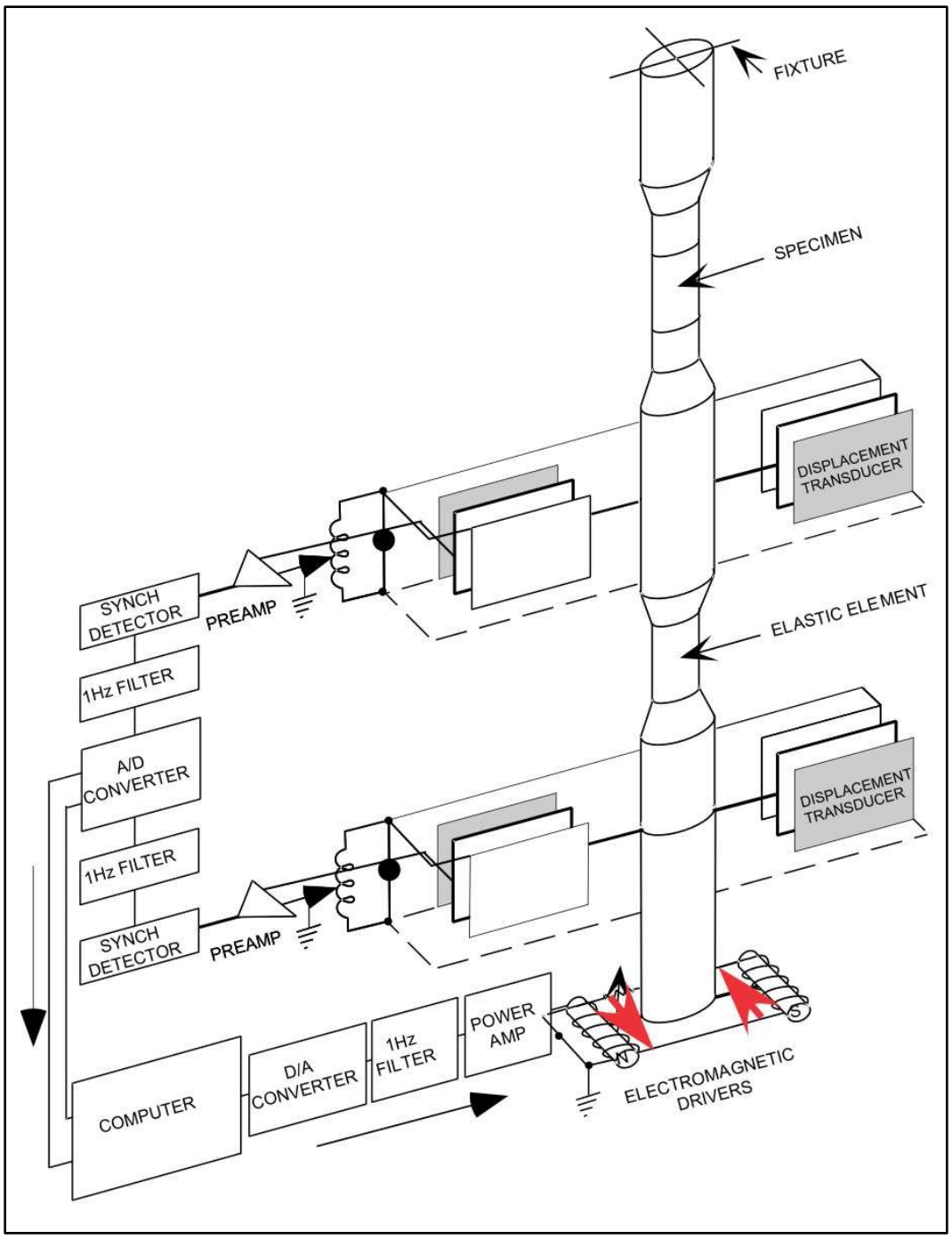

Figure 3.5: Schematic of ANU attenuation apparatus used to make low frequency torsional measurements (modified from Jackson *et al.* (2011), with permission).

The steel elastic standard has a known shear modulus, μ_s, and moment of inertia, I_s, which allows the shear modulus of the specimen assembly to be expressed in terms of known and experimentally measured parameters:

$$|\mu_A| = \left| \frac{\mu_S d_2 D_1 I_S}{d_1 I_A} \right| \tag{3.6}$$

As the contributions of the alumina rods and the annealed copper jacket to the overall shear modulus of the specimen assembly are poorly known at the measured effective pressures, it is necessary to compare the shear modulus of this experimental assembly to that of an assembly with a sample of known shear modulus, μ_{AFQ}. The shear modulus of the rock specimen itself, μ_R, can then be solved

$$\mu_R - \mu_{FQ} = \mu_A - \mu_{AFQ} \tag{3.7}$$

and rearranged

$$\mu_R = \mu_A - \mu_{AFQ} + \mu_{\mathrm{FQ}} . \tag{3.8}$$

Note that while the shear modulus of the standard substituted for the rock specimen, μ_{FQ}, must be known, the shear modulus of the overall assembly comprised of the alumina rods, copper jacket and standard, μ_{AFQ}, is measured experimentally (Jackson and Paterson, 1993).

Fused quartz is frequently used as a standard and has a well known shear modulus (McSkimin *et al.*, 1965). An experimental assembly where the quartzite was replaced with fused quartz was measured over the same effective pressures as the

quartzite assembly to allow the calculation of the shear modulus of the two quartzites at the various pressures under the different saturation conditions.

The low frequency shear moduli of the quartzites were measured over effective pressures from 10-180 MPa while dry, argon saturated and water saturated. During water saturated measurements it was necessary to slightly dilute the water with an anti-rust agent to avoid corrosion of the steel components of the low frequency apparatus.

3.3.2 High frequency measurements

High frequency measurements were undertaken at 1 MHz using ultrasonic pulse transmission (Appendix A). The quartzite shear moduli were again measured dry, argon saturated and water saturated (Tables 3.1 – 3.6). Piezoelectric transducers capable of generating 1 MHz P- and S-waves were affixed to aluminum buffers and the quartzite samples were placed in between the buffers and encased in flexible tubing. They were then subjected to confining hydrostatic pressure only for the dry measurements, and to confining and pore pressure for the argon and water saturated measurements.

In order to calculate the high frequency shear modulus, the S-wave travel time through the sample and buffers was measured. The travel time through the quartzite sample alone, t_s, was determined by measuring the travel time through the two buffers when no sample was present, and subtracting that from the overall time (Fig. 3.6). Pressure effects on the buffers were removed by calibrating the buffers over the same range of pressures as the buffer and sample combination. S-wave travel time was used in conjunction with the sample bulk density to obtain the high frequency shear modulus:

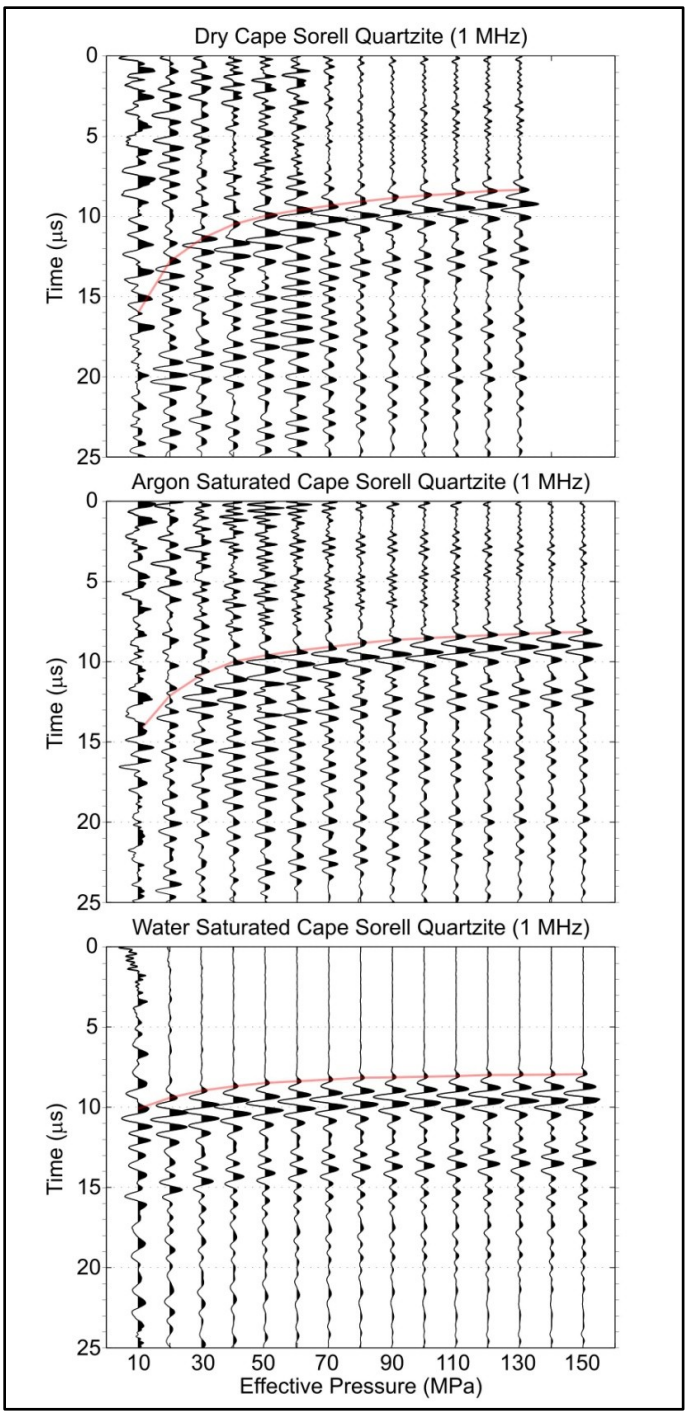

Figure 3.6: At pressures >80MPa, when the cracks are closed, the differences between the water saturated and dry or argon saturated shear wave velocities of the Cape Sorell quartzite are minimal, however, water filled cracks cause significant stiffening of the shear modulus at lower effective pressures.

$$\mu_H(P_{eff}) = \left[\frac{L_S}{t_S}\right]^2 \rho \quad (3.9)$$

where μ_H is the high frequency shear modulus, L_S the sample length, ρ the bulk density and P_{eff} the effective pressure. Volumetric changes of the frame between 0-150 MPa were calculated using the isothermal bulk modulus and pressure derivative values of single crystal quartz (Liu, 1993) as input into the Birch-Murnaghan equation of state (Birch, 1947), but were found to be small, causing a volume change of <0.4% across the range of measured pressures. Volumetric changes resulting from crack closure were more substantial, as the ~2% porosity is anticipated to undergo almost complete closure by 150 MPa of pressure, but still quite small. For the purposes of estimating the volumetric change resulting from crack closure, the cracks were assumed to close logarithmically. The initial sample length was measured at atmospheric pressure using vernier calipers and the effects of the total volumetric changes on both sample length and bulk density were calculated. The P-wave velocities were also measured at high frequency across a similar range of pressure, but presentation of these is delayed until Chapter 4.

Dry measurements were made after the samples were vacuum oven dried overnight, and then left at ambient conditions and atmospheric humidity for several days in an effort to avoid artefacts from being 'over dried' (Cadoret, 1993). During 'dry' measurements from 10-150 MPa of pressure, the pore space was filled with air at atmospheric temperature and pressure.

Argon saturated measurements were made next. Measurements with pore pressure were made by vacuuming the specimens prior to the introduction of pore fluid.

Pore pressure was then introduced through a small diameter hole in the topmost buffer and given time to equilibrate, allowing complete saturation, prior to the shear modulus measurement. The required equilibration time was estimated from the stabilization of the pore fluid pressure gauge as well as from the permeability measurements. The allowed time varied from 15 minutes at the lowest effective pressures (10 MPa) and for the lower viscosity argon pore fluid to >8 hours at the highest effective pressures (140 MPa) for the higher viscosity water pore fluid. As an additional check that sufficient equilibration time had been allotted, the quartzites were measured during loading and unloading, when possible, to ensure repeatability of the measurements. Argon saturated measurements were made over effective pressures from 10-150 MPa. For safety reasons, it was not possible to pressurize the argon pore fluid beyond 10 MPa during the high frequency measurements, so the desired effective pressures were obtained by keeping the argon pore pressure at 10 MPa and varying the confining pressure as necessary. At room temperature, argon is a supercritical fluid at pressures >5 MPa (NIST, 2012); keeping the pore pressure at 10 MPa allowed the high and low frequency measurements to be made with argon in the same phase.

Water saturated measurements were made after saturating the sample with distilled water overnight at an effective pressure <5 MPa. For the quartzites' estimated permeabilities of >1 x 10^{-20} m^2 at this effective pressure, Rice and Cleary (1976) have shown that this should be more than sufficient time to equilibrate the pore pressure gradient across the ~3 cm long samples and achieve complete saturation. During water saturated measurements, the confining pressure was kept constant at 150 MPa and the pore pressure was varied to obtain the appropriate effective pressures of 10-150 MPa.

The low permeabilities of the quartzites meant that equilibration times of >8 hours were required to ensure an even distribution of water pore fluid in the sample at the highest effective pressures.

3.4 Experimental results

Both quartzites showed extremely low permeability (Fig. 3.7), with measurements ranging from 3.05 x 10^{-19} m^2 to 1.16 x 10^{-21} m^2 (309 nD to 1.18 nD). The Cape Sorell quartzite showed a well behaved exponential decrease in permeability with increased effective pressure. The Alberta quartzite permeability, while still showing a clear decrease with effective pressure, did not show a straightforward relationship with effective pressure. The Alberta quartzite underwent a sharp decrease in permeability at effective pressures greater than 50 MPa.

Measurements of the shear moduli of both quartzites showed the shear moduli increasing with effective pressure as the cracks in the samples underwent progressive closure. This effect was quite strong, and the modulus of the dry Alberta quartzite increased from 11.9±0.3 GPa to 34.88±0.08 GPa over confining pressures 10-150 MPa at high frequency; an increase of 193%. Similarly, the shear modulus of the Cape Sorell quartzite increased from 10.9±0.9 GPa to 36.03±0.09 GPa from 10-130 MPa confining pressure (Fig. 3.8). The quartzites both exhibited substantial increases in shear modulus stiffness up to effective pressures of ~80 MPa; above this effective pressure the increase in shear modulus became less rapid and more linear.

The Cape Sorell quartzite was measured at both low and high frequency while

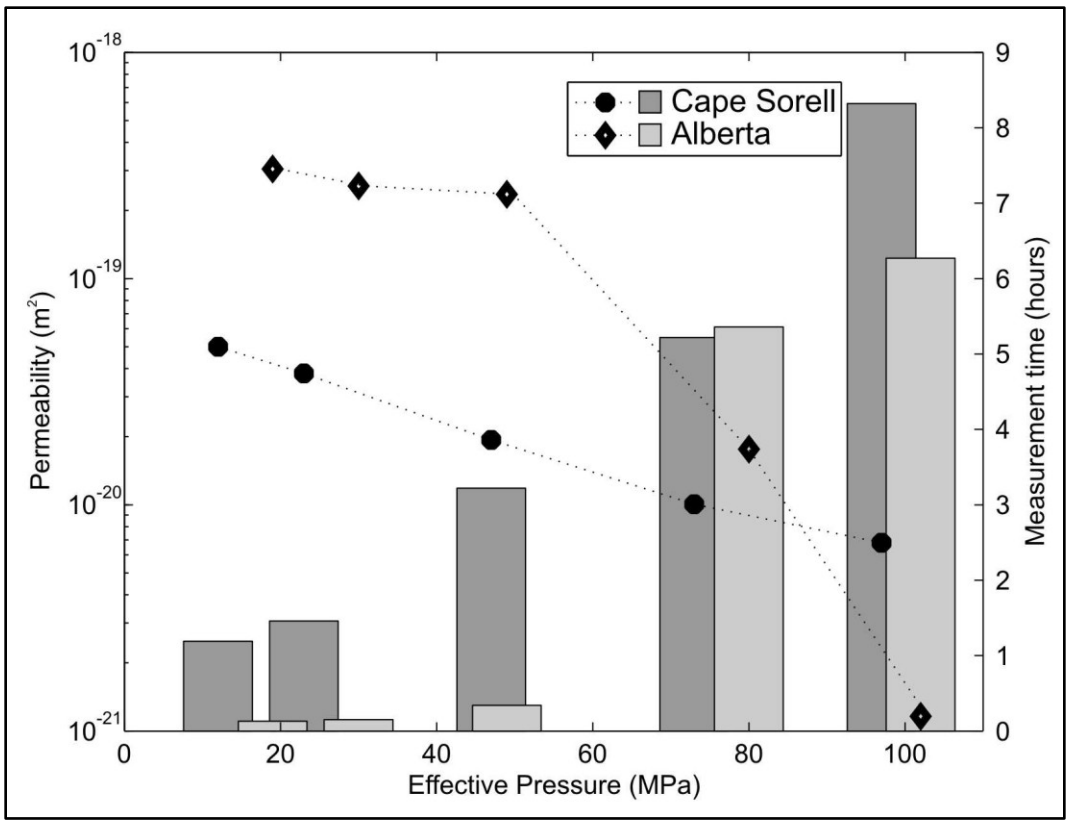

Figure 3.7: Permeability (dotted lines) on the left y-axis and measurement time (bars) on the right y-axis against effective pressure, showing the logarithmic relationship between permeability and pressure for the Cape Sorell quartzite and the more complex pressure dependence of permeability for the Alberta quartzite, possibly partly resulting from differences in the length of the time series available for analysis.

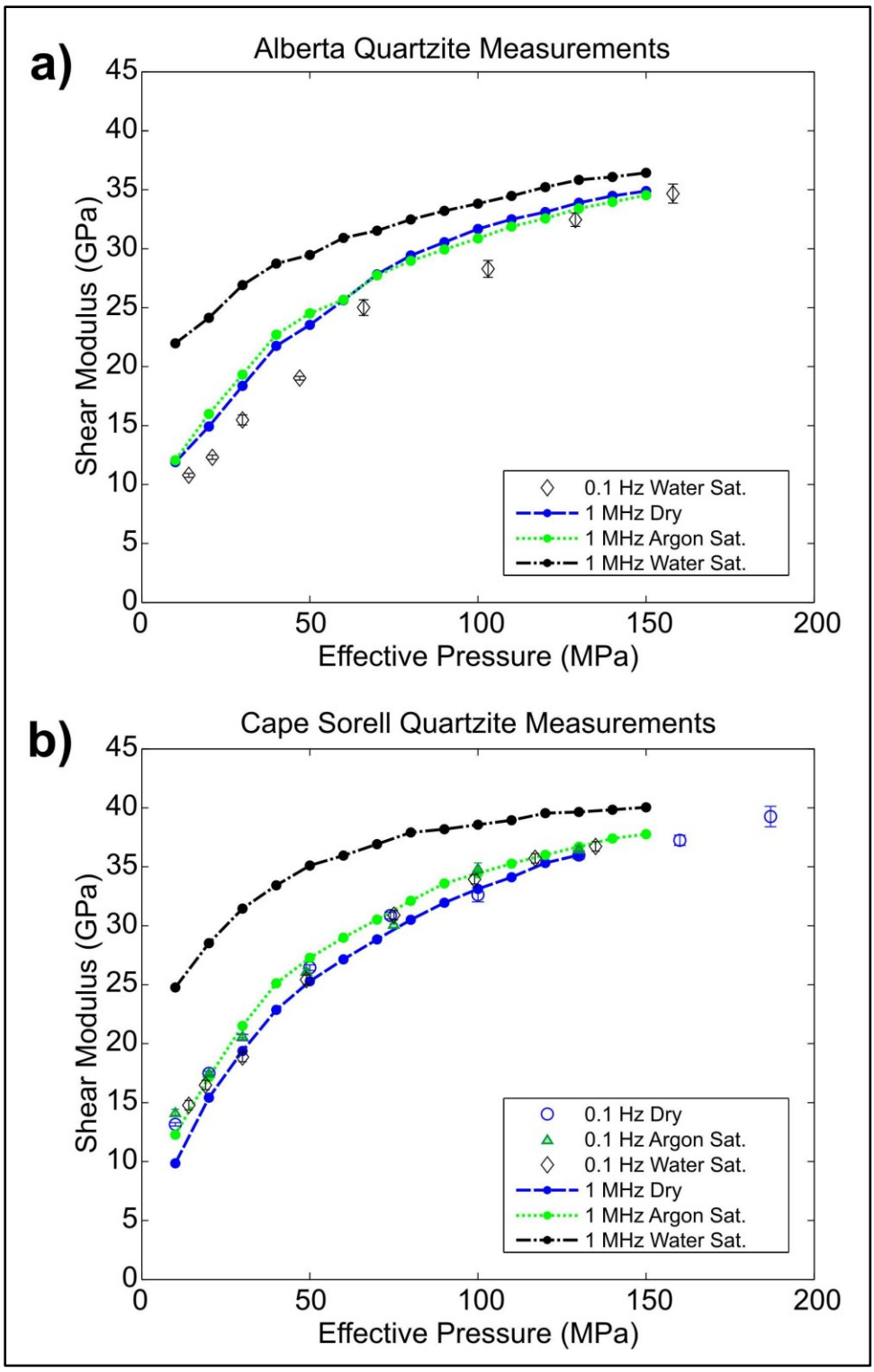

Figure 3.8: The water saturated samples have a significantly stiffer shear modulus at 1 MHz.

dry, argon saturated and water saturated. Due to experimental difficulties, however, the Alberta quartzite was measured in all three states at high frequency, but only in a water saturated state at low frequency. Dry and argon saturated dispersion measurements were therefore limited to the results from the Cape Sorell quartzite. The dry Cape Sorell quartzite, as expected, did not exhibit any shear modulus dispersion, with consistent shear modulus measurements observed from 0.01 Hz to 1 MHz. The argon saturated case was more complicated; no stiffening appeared to occur at low frequency when the dry Cape Sorell quartzite was saturated with argon pore fluid, while a slight stiffening was seen at high frequency. This change in behaviour may be indicative of dispersion, although the differences between the low and high frequency results were close to the errors of the experimental uncertainty. The Cape Sorell quartzite exhibited a slightly stiffer shear modulus at 1 MHz at all effective pressures when argon saturated, while the Alberta quartzite exhibited a stiffer shear modulus at effective pressures 10-50 MPa.

The water saturated measurements showed clear evidence of substantial dispersion for both quartzites. Measurements between 1 mHz and 1 Hz appeared to be frequency independent, but substantial dispersion occurred between 1 Hz and 1 MHz. For the water saturated Cape Sorell quartzite at 20 MPa the 1 Hz shear modulus was 16.4 GPa, while the 1 MHz shear modulus was 28.5 GPa; the Alberta quartzite ranged from 12.2 GPa to 24.1 GPa at the same pressure and frequencies. Dispersion was most significant at lower effective pressure when crack porosity was highest, but was evident at all measured pressures.

3.5 Theoretical modeling

Numerous models, including those derived by Budiansky and O'Connell (1976) and Hudson (1981) use the crack density and pore fluid properties (if any) to calculate the effect of dry and saturated cracks on the rock moduli. Here the shear modulus stiffening was directly experimentally measured, and it was possible to instead use the models to estimate crack density from the amount of shear modulus stiffening. The crack density of the samples, ε, is defined as

$$\varepsilon = Na^3 \tag{3.10}$$

with N the number density and a the radius of the cracks. Hudson (1980, 1981) shows the shear modulus of the cracked rock, μ, can be approximated by a correction term, μ_1, to the shear modulus of the uncracked rock, μ_0:

$$\mu = \mu_0 + \mu_1 \tag{3.11}$$

To first order for a distribution of randomly oriented cracks, Hudson (1981) gives the correction μ_1 as

$$\frac{\mu_1}{\mu_0} = -\frac{16}{45}\varepsilon\left(\lambda_0 + 2\mu_0\right)\left[\frac{6}{\left(3\lambda_0 + 4\mu_0\right)} + \frac{1}{\left(1+J\right)\left(\lambda_0 + \mu_0\right)}\right] \tag{3.12}$$

for the case where the cracks are filled with a highly compressible material with negligible shear modulus. Here λ_0 and μ_0 are the Lamé parameters of the uncracked rock and J is given by

$$J = \frac{a}{c}\frac{K_{fl}}{\mu_0 \pi}\frac{\left(\lambda_0 + 2\mu_0\right)}{\left(\lambda_0 + \mu_0\right)} \tag{3.13}$$

where *c* is the minor axis length of the cracks, and K_{fl} is the bulk modulus of the material in the cracks. Approximating the cracks as perfect ellipsoids allows the crack concentration to be related to the porosity, ϕ:

$$\varepsilon = \frac{3\phi}{4\pi}\frac{a}{c}. \tag{3.14}$$

This assumes that the cracks are all of similar size and aspect ratio, and further, that they are ellipsoidal in shape. Substituting Equation 3.14 into Equation 3.12 and reorganizing yields a quadratic equation that may be solved for the inverse of the crack aspect ratio.

$$\left(\frac{a}{c}\right)^2 \frac{8}{5}\frac{\phi}{\pi}\frac{(\lambda_0+2\mu_0)}{(3\lambda_0+4\mu_0)} + \left(\frac{a}{c}\right)\left[\frac{8}{5}\frac{\mu_0\phi}{K_{fl}}\frac{(\lambda_0+\mu_0)}{(3\lambda_0+4\mu_0)} + \frac{4}{15}\frac{\mu_0\phi}{K_{fl}} + \frac{\mu_1}{\mu_0}\right] + \frac{\mu_1\pi}{K_{fl}}\frac{(\lambda_0+\mu_0)}{(\lambda_0+2\mu_0)} = 0 \tag{3.15}$$

The minor axis of the crack, *c,* was taken to be half of the mercury porosimetry-measured pore throat diameter, although this may not be strictly true as mercury porosimetry provides only a minimum size. The uncracked shear modulus, μ_0 was approximated by the measured high frequency dry shear modulus, μ_H, at the highest measured confining pressures (130 MPa for the Cape Sorell quartzite and 150 MPa for the Alberta quartzite), and the correction term, μ_1, by the difference between the high frequency dry shear modulus at the lowest measured confining pressure (10 MPa) and the high pressure shear modulus. The shear modulus of the uncracked rock was taken to be the high pressure shear modulus of the quartzite as opposed to the shear modulus of pure polycrystalline quartz in order to better incorporate any effects from the small amount of muscovite at the quartz grain boundaries of the sample. Finally, if λ_0 is

calculated from the high frequency, high pressure P-wave velocity (see Chapter 4), then Equation 3.15 can be solved for the crack radius, a. When the samples were dry, K_{fl} was negligible, as it could be approximated as the bulk modulus of nitrogen gas at room temperature and atmospheric pressure, 101 kPa (NIST, 2012). The quartzites were connected to pore pressure tubing filled with air at atmospheric temperature and pressure when they were dry; the comparatively large storage capacity of the tubing meant that changes in pore space volume resulted in negligible changes to the pore pressure of the dry samples at high confining pressures.

The model put forward by Hudson (1981), as shown in Equation 3.15, approximated the crack radius of the Cape Sorell quartzite sample to be 16 μm, and for the Alberta quartzite, 24 μm. The second solution to the quadratic was negative and cannot be real. While the radius of the cracks of the two samples could only be visually estimated from SEM and light microscope images, they appeared to be on the order of the grain sizes; ~500 μm in both cases, or more than an order of magnitude different from the theoretical estimations. This was likely because Hudson (1981) assumes the concentration of cracks is dilute and the cracks therefore do not interact, *e.g.* ε<0.1 (Hudson, 1986). In practice, this was potentially inaccurate for these samples at low effective pressure. For the Cape Sorell quartzite with porosity 2.3% and pore throat size ~0.4 μm, a would need to be <3.6 μm to achieve ε<0.1, which is not supported by either the experimental observations or the theoretical results. The Alberta quartzite had a similarly high crack density at low pressure.

In both the high and low frequency measurements in all saturating condition, the shear modulus entered a more linear regime at ~80 MPa of effective pressure and

above, indicating that the cracks reached maximum effective closure around this pressure. As the shear modulus at higher pressures continued to be lower than the 44.4 GPa calculated for a polycrystalline aggregate (Watt and Peselnick, 1980) from single crystal quartz values (McSkimin *et al.*, 1965), it was likely the quartzite still had non-zero porosity. Walsh (1965a) gives the effective pressure needed to close a randomly oriented distribution of penny-shaped cracks as:

$$P_{eff} = \frac{\pi \alpha \mu_0}{2(1-\nu_0)} \tag{3.16}$$

where ν_0 is the mineral Poisson ratio. Since the pressure required for crack closure was known, this could be rearranged to solve for the crack aspect ratio, α. The shear modulus for quartz at room temperature and pressure, 44.4 GPa (McSkimin *et al.*, 1965, Watt and Peselnick, 1980), and the Poisson ratio, 0.073, calculated from the bulk modulus given by Liu (1993), yielded an aspect ratio of 0.001. This corresponded to a crack radius of 0.4 mm for the Cape Sorell quartzite and 0.7 mm for the Alberta quartzite, which agreed well with the visually observed estimate of ~0.5 mm crack length in both cases.

3.6 Discussion

The Cape Sorell and Alberta quartzite shared relatively similar physical properties; both had a largely monominerallic quartz composition, grain sizes of approximately 0.5 mm, porosity on the order of ~2% and pore throat sizes <1 μm. Interestingly, however, their permeability differed somewhat in behaviour. While the Cape Sorell quartzite

showed a well-behaved exponential decrease in permeability with increasing effective pressure, the Alberta quartzite showed a sharp decline in permeability at effective pressures >50 MPa . This may result from a difference in how the measurements were made, or may be an actual effect in the rock. The Cape Sorell measurements were made over a nearly constant confining pressure (varying from 139-140 MPa) with the majority of the changes in effective pressure being attributable to changes in pore pressure. Difficulties in obtaining the desired final pore pressure for the Alberta quartzite meant that adjustments to the pore pressure in the middle of the pressure equilibration were made more frequently, with the result that virtually all permeability measurements on the Alberta quartzite were obtained over a shorter time frame than the equivalent measurements on the Cape Sorell quartzite. The effective permeability measured on the Alberta quartzite appears to show some dependence on measurement interval (Fig. 3.4b), with higher apparent permeability at early times. The length of measurement may account for some of the higher permeability seen in the Alberta quartzite at low effective pressures during short measurements (Fig. 3.7), however, it likely does not completely explain the significant permeability decrease beyond 50 MPa of pressure. The variability in effective permeability seen in the Alberta quartzite with time indicates the pore throats may have become clogged at higher effective pressure by particulate matter, or that there might have been some slight heterogeneity in the permeability of the sample along its length. Indeed, as the Alberta quartzite, originally cored at a 2.54 cm (1 inch) diameter but reduced post thermal cracking to the required 15 mm diameter through high precision grinding, was pressurized, it was noted that at low effective pressures the sample was cylindrical but at high pressures, when substantial amounts of crack closure had occurred, the sample took on a slight

curvature (<0.25 mm displacement from central axis) along its 150 mm length. This was likely the result of some very slight anisotropy in the crack distribution within the sample. The Cape Sorell quartzite was prepared in a different laboratory for logistical reasons and was thermally fractured after precision grinding. Possibly as a result of the different method of preparation, the Cape Sorell quartzite did not appear to show this curvature at either low or high pressures. The abrupt change in permeability beyond 50 MPa of effective pressure may also have resulted from the mineralogy of the Alberta quartzite. As seen on the thin section and SEM images, the crack and grain boundaries of the Alberta quartzite are quite clean and smooth. At high effective pressures it may be that many of the pore throats closed completely, effectively isolating many of the cracks from each other. The muscovite at the grain boundaries of the Cape Sorell quartzite may have served to keep most of the intercrack pathways open even at high effective pressures.

A second difference in behaviour between the two quartzites was observed during the argon saturated high frequency measurements. The Cape Sorell quartzite had a stiffer argon saturated shear modulus than dry shear modulus at all measured effective pressures, while this was true only for measurements made from 10-50 MPa for the Alberta quartzite. Here, the difference in behaviour likely resulted from some slight additional cracking occurring in the Alberta quartzite under the initial pressurization when dry measurements were made. The difference in composition or in preparation may have made the Alberta quartzite more susceptible to brittle behaviour. Subsequent argon and water saturated high frequency measurements then had a slightly different crack porosity and behaviour.

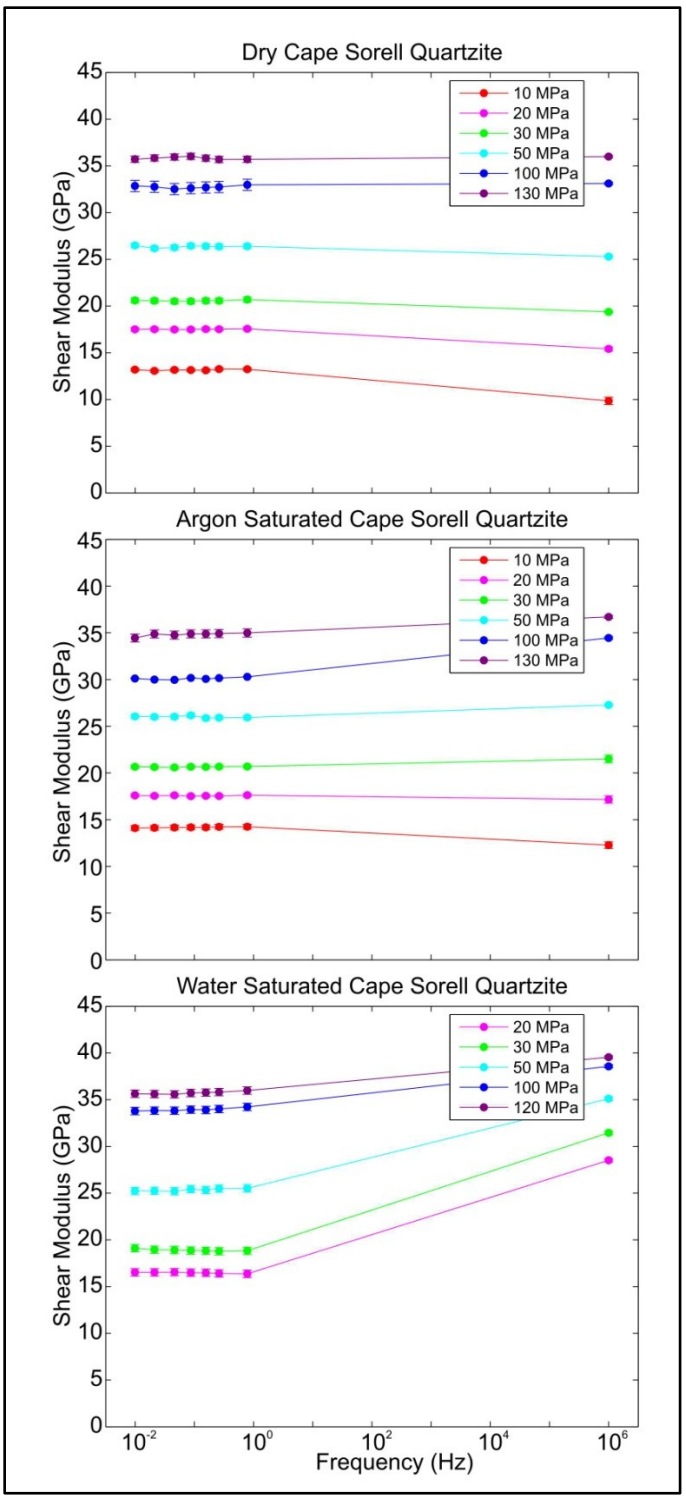

Figure 3.9: Between 0.01 – 1 Hz, the dry, argon and water saturated shear moduli of the Cape Sorell quartzite do not show any velocity dispersion. The quartzite shows significant dispersion between 1 Hz and 1 MHz when it is water saturated, particularly at low effective pressures.

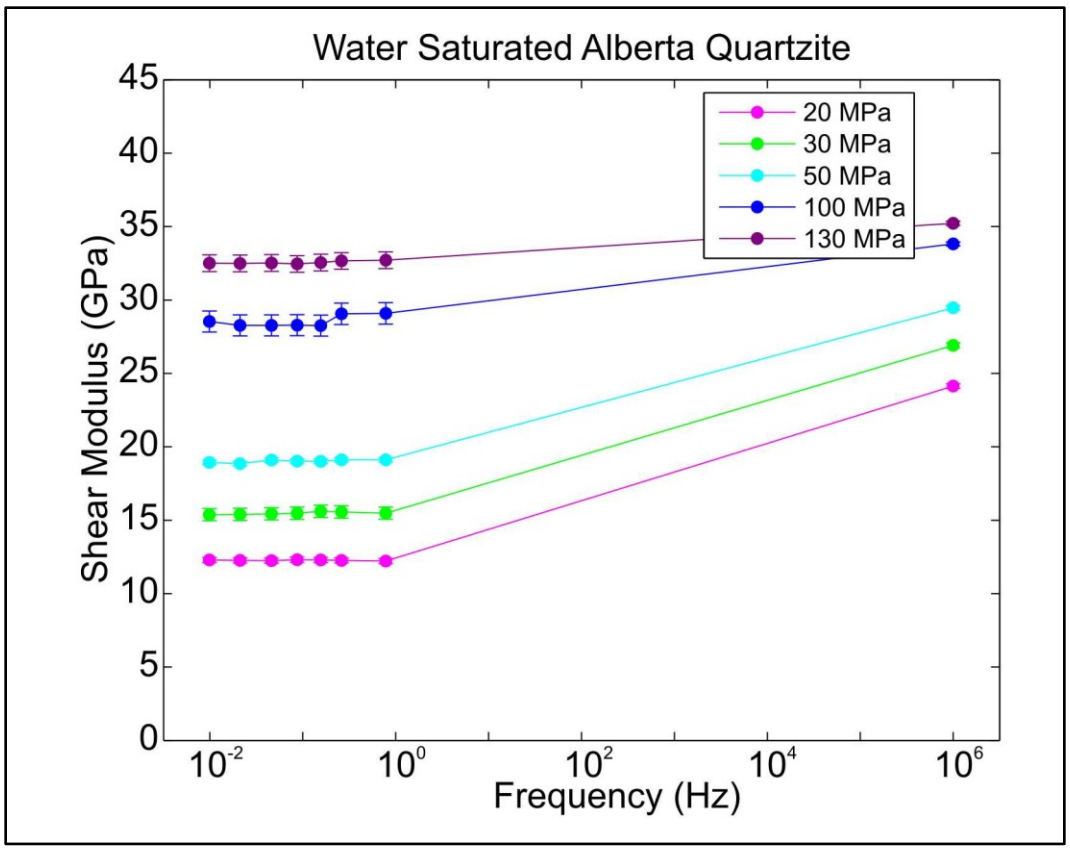

Figure 3.10: The quartzite shows significant dispersion between 1 Hz and 1 MHz when it is water saturated, particularly at low effective pressures. Measurements are made during the 'up' cycle of pressurization, showing shear moduli during loading. Listed effective pressures are those corresponding to the high frequency measurement (low frequency measurements may vary from the listed pressure by up to 3 MPa).

In most ways, however, both quartzites behaved quite similarly. At low frequencies between 0.01 and 1 Hz, neither quartzite showed any saturation-dependent variation in its shear moduli while dry, argon saturated or water saturated (Figs. 3.9, 3.10). Gassmann (1951) predicted that the dry and saturated shear moduli of a rock are equal when the rock is in a saturated isobaric fluid flow regime, and this lack of stiffening at <1 Hz may be evidence that the frequencies measured here were sufficiently low to allow pore pressure equilibration during the course of the measurement. Although the bulk density of the sample increased slightly with saturation, the effect of the dry and saturated shear moduli being equivalent did not result in significant variations in the calculated low frequency shear wave speeds due to the low porosity of the samples (Fig. 3.11).

Dispersion was evident between 1 Hz and 1 MHz in some of the measurements. While high frequency dry measurements agreed with their low frequency counterparts, saturation with argon caused slight stiffening in some high frequency measurements. Comparison between low and high frequency measurements was complicated due to variable argon pore pressures and therefore variable pore fluid properties (Fig. 3.12) as well as small differences in effective pressures measured. Nonetheless, it seems apparent that a small amount of dispersion occurred as a result of argon saturation, indicating a fluid flow regime change between 1 Hz and 1 MHz.

Water saturation resulted in substantial dispersion, evidenced by the stiffening of the shear moduli of both quartzite specimens: up to 251% for the Cape Sorell and up to 185% for the Alberta quartzite, at 1 MHz (Figs. 3.8-3.10) when compared to dry

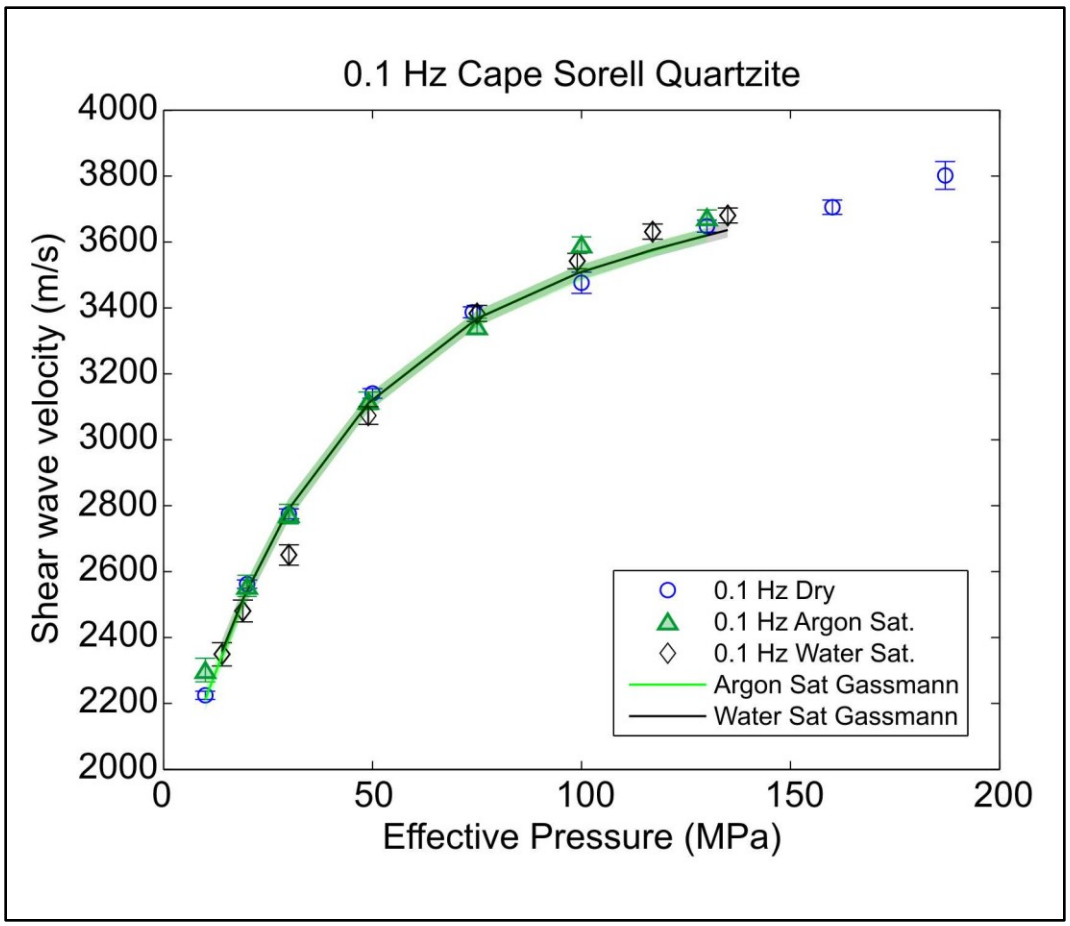

Figure 3.11: Calculated low frequency shear wave velocities compared to Gassmann predictions for the Cape Sorell quartzite. Estimated errors in Gassmann predictions shown as shaded area.

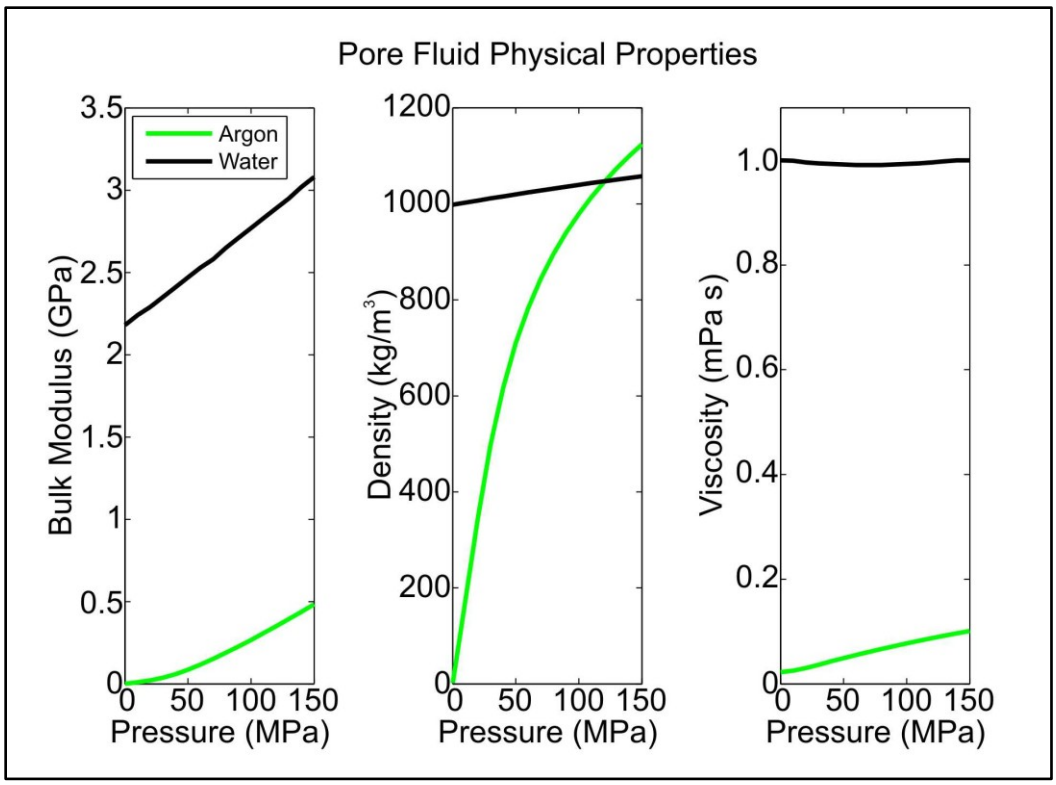

Figure 3.12: Physical properties of the argon and water used to saturate the quartzite samples. Values from NIST (2012).

measurements. The low frequency water saturated measurements agreed with low frequency dry and argon saturated measurements, likely indicating that at frequencies <1 Hz the water saturated quartzites, similar to when argon saturated, behaved as in the saturated isobaric fluid flow regime. The dispersion between 1 Hz and 1 MHz was most pronounced at lower effective pressures, likely resulting from the higher crack porosity present when the cracks were open. At pressures >80 MPa, when the cracks were closed, the differences between the water saturated and dry or argon saturated shear wave velocities were less (Fig. 3.8), but were non-zero. This indicates that, even at the highest effective pressures measured here, some porosity still existed, with the saturated cracks having reduced compliance. The substantial stiffening from 1 Hz to 1 MHz indicates a fluid flow regime change, with the 1 MHz measurements likely in the saturated isolated regime. Although water has a viscosity (1 mPa·s) substantially greater than that of argon (0.03 mPa·s at 10 MPa to 0.12 mPa·s at 150 MPa cP) at these temperatures and pressures (NIST, 2012), the quartzites appeared to transition between the isobaric and isolated fluid flow regimes between 1 Hz and 1 MHz when saturated with either pore fluid.

3.7 Conclusions

The two quartzites studied, from Cape Sorell, Australia, and Alberta, Canada, show a single population of low aspect ratio cracks in a near monominerallic quartz frame. Shear wave velocity dispersion was successfully measured on both samples, providing important experimental results for a field largely dominated by theoretical work. As expected, the dry shear modulus of the quartzites is a function only of

effective pressure, not of frequency. The dry shear modulus of the cracked Cape Sorell quartzite at 10 MPa of effective pressure and 1 MHz is 10.9±0.9 GPa and varies from 13.1±0.1 GPa to 13.2±0.1 GPa rom 0.01-1 Hz during loading. Similarly, the Alberta quartzite has a dry shear modulus of 11.9±0.3 GPa at 1 MHz.

No dispersion was observed in the shear modulus of the argon saturated quartzites, however, stiffening of the argon saturated ultrasonic measurements compared to the dry indicates that dispersion is likely occurring but has an amplitude lower than the experimental error, due in part to pore fluid property variations between frequencies. At 20 MPa, the argon saturated Cape Sorell quartzite has a shear modulus varying from 17.5±0.2 GPa to 17.6±0.2 GPa between 0.01 and 1 Hz during loading. The 1 MHz shear modulus, 17.2±0.4 GPa, agrees with the low frequency measurements within error, but is 11% stiffer than its dry high frequency counterpart (15.4±0.2 GPa).

The water saturated quartzites show substantial frequency-dependent dispersion in their shear moduli. High frequency water saturated shear moduli are substantially stiffer than those measured at low frequencies. Water saturated moduli measured at 1 MHz and 20 MPa of effective pressure are 74% higher than their 1 Hz counterparts for the Cape Sorell quartzite and 98% stiffer for the Alberta quartzite. The amount of dispersion grows less with increasing effective pressure as a result of crack closure, however, even at maximum effective crack closure the water continues to cause additional stiffening at high frequencies. This indicates that the cracks do not completely close over the range of effective pressures measured, but that when measured at high frequency the pore fluid is not able to flow between cracks and the cracks behave as in the saturated isolated regime. The Cape Sorell quartzite shows a 9%

increase between the 1 Hz and 1 MHz measurements at 120 MPa of effective pressure, while the Alberta quartzite shows a 10% increase at 130 MPa. At low frequencies (0.01-1 Hz) no dispersion is seen, with 0.01 Hz measurements in agreement with 1 Hz measurements. This indicates that both water saturated specimens behave as in the saturated isobaric regime where fluid has sufficient time to flow between cracks on the timescale of measurement, allowing pore pressure equilibration at frequencies ≤1 Hz. The low frequency water saturated shear moduli are in agreement with the shear moduli measured when the samples were dry or argon saturated, as predicted by Gassmann.

The samples were pressurized multiple times, but their shear moduli were frequently measured during both loading and unloading in order to determine the repeatability of the measurements. The samples show excellent repeatability overall, indicating crack growth and hysteresis was minimal. The exception to this was a lessening of the argon saturated stiffness of the Alberta quartzite during ultrasonic measurements at pressures >50 MPa, possibly indicating some additional cracking occurred in the dry measurement run immediately preceding the argon saturated measurements.

Both quartzites consistently undergo large changes in their shear moduli up to ~80 MPa of effective pressure. At higher pressures their shear moduli have a more linear relationship with pressure, and this is interpreted to indicate that maximum crack closure occurs around ~80 MPa. This result supports the relationship between pressure necessary to effect crack closure and crack aspect ratio proposed by O'Connell and Budiansky (1977); the theory proposed by Hudson (1981) was unable to model the

quartzite results as it is limited by an assumption of low crack concentration which is inaccurate for these samples. In addition to shear moduli, permeability was measured as a function of pressure. The Cape Sorell quartzite show a logarithmic decrease in permeability as a function of pressure up to the highest effective pressure measured, 100 MPa. The Alberta quartzite, however, show a more complicated relationship between permeability and pressure, with a sudden strong decrease in permeability between 50 and 80 MPa of effective pressure. This is likely largely attributable to the difference in mineralogy between the two samples, as the Alberta quartzite appears to have clean, smooth grain boundaries in thin section images which may be capable of more complete closure of the intergranular space than the muscovite edged grains of the Cape Sorell quartzite, preventing fluid flow between cracks, but may be the result in anisotropic crack distribution or particulate matter clogging pore throats during the permeability measurements.

As the shear modulus affects both P- and S-wave seismic velocities, the experimental results measured on the two quartzite specimens show that dispersion can have an extremely large effect on velocity measurements of both body waves and has important implications for seismic acquisition and modeling of cracked crystalline rocks. It is generally thought that the majority of the Earth's crystalline crust has fluid-filled cracks and these can be expected to cause significant velocity dispersion between seismic measurements acquired across a broad range of frequencies. This data set provides necessary experimental data with which to constrain theoretical models.

Table 3.1: Cape Sorell quartzite dry shear modulus measurements

Frequency

Pressure (GPa)	1 mHz (up)	2.1 mHz (up)	4.7 mHz (up)	9.9 mHz (up)	9.9 mHz (down)	0.021 Hz (up)	0.021 Hz (down)	0.046 Hz (up)	0.046 Hz (down)	0.087 Hz (up)	0.087 Hz (down)	0.16 Hz (up)	0.16 Hz (down)	0.26 Hz (up)	0.26 Hz (down)	0.78 Hz (up)	0.78 Hz (down)	1 MHz (up)	1 MHz (down)
10/12/10	*	*	*	13.202	19.469	13.064	19.469	13.165	19.469	13.147	19.469	13.124	19.469	13.249	19.469	13.235	19.469	9.85	*
20	*	*	*	17.503	21.285	17.513	21.334	17.49	21.239	17.484	21.315	17.537	21.327	17.523	21.299	17.564	21.285	15.41	*
30	*	*	*	20.599	26.842	20.569	26.814	20.513	26.793	20.514	26.812	20.569	26.848	20.567	26.723	20.687	26.733	19.38	*
40	*	*	*	*	*	*	*	*	*	*	*	*	*	*	*	*	*	22.87	*
50/51/50	*	*	*	26.483	30.775	26.181	30.707	26.27	30.722	26.443	30.937	26.394	30.788	26.37	30.809	26.393	30.659	25.29	*
60	*	*	*	*	*	*	*	*	*	*	*	*	*	*	*	*	*	27.15	*
70	*	*	*	*	*	*	*	*	*	*	*	*	*	*	*	*	*	28.84	*
74/75/*	*	*	*	30.713	34.071	30.548	34.277	30.603	34.225	30.868	34.231	30.716	34.123	30.751	34.154	30.787	34.03	*	*
80	*	*	*	*	*	*	*	*	*	*	*	*	*	*	*	*	*	30.50	*
90	*	*	*	*	*	*	*	*	*	*	*	*	*	*	*	*	*	31.95	*
100	*	*	*	32.849	36.137	32.768	36.15	32.52	36.07	32.622	36.213	32.701	36.242	32.738	36.321	32.971	36.729	33.12	*
110	*	*	*	*	*	*	*	*	*	*	*	*	*	*	*	*	*	34.11	*
120	*	*	*	*	*	*	*	*	*	*	*	*	*	*	*	*	*	35.33	*
130/131/130	*	*	*	35.712	37.829	35.842	37.911	35.945	37.854	36.021	37.892	35.823	37.762	35.683	37.521	35.705	37.571	35.99	*
140	*	*	*	*	*	*	*	*	*	*	*	*	*	*	*	*	*	*	*
150	*	*	*	*	*	*	*	*	*	*	*	*	*	*	*	*	*	*	*
160/161/*	*	*	*	37.208	37.046	37.189	37.251	37.269	37.127	37.247	37.084	37.068	36.906	36.766	36.542	36.843	36.622	*	*
187	*	*	*	38.58	*	38.864	*	39.069	*	39.264	*	39.3	*	39.356	*	39.355	*	*	*

* Where multiple pressures are shown, the first indicates the low frequency pressure during loading (up), the second the low frequency pressure during unloading (down) and the third the high frequency pressure during both loading and unloading measurements, where applicable.

Table 3.2: Cape Sorell quartzite argon saturated shear modulus measurements

Frequency

Pressure (GPa)	1 mHz (up)	2.1 mHz (up)	4.7 mHz (up)	9.9 mHz (up)	9.9 mHz (down)	0.021 Hz (up)	0.021 Hz (down)	0.046 Hz (up)	0.046 Hz (down)	0.087 Hz (up)	0.087 Hz (down)	0.16 Hz (up)	0.16 Hz (down)	0.26 Hz (up)	0.26 Hz (down)	0.78 Hz (up)	0.78 Hz (down)	1 MHz (up)	1 MHz (down)
10	*	*	*	*	14.103	*	14.128	*	14.16	*	14.18	*	14.179	*	14.236	*	14.244	12.28	*
20	*	*	*	17.592	18.446	17.552	18.387	17.605	18.445	17.526	18.436	17.551	18.47	17.538	18.519	17.616	18.566	17.16	*
30	*	*	*	20.656	21.703	20.628	21.731	20.588	21.721	20.662	21.724	20.648	21.749	20.678	21.814	20.693	21.832	21.51	*
40	*	*	*	*	*	*	*	*	*	*	*	*	*	*	*	*	*	25.11	*
49/48/50	*	*	*	26.049	27.107	26.009	27.128	26.017	27.172	26.163	27.272	25.877	27.204	25.916	27.228	25.927	27.086	27.28	*
60	*	*	*	*	*	*	*	*	*	*	*	*	*	*	*	*	*	28.98	*
70	*	*	*	*	*	*	*	*	*	*	*	*	*	*	*	*	*	30.52	*
75/74/75	*	*	*	30.116	32.786	30	32.721	29.963	32.644	30.169	32.838	30.071	32.778	30.155	32.742	30.284	32.604	*	*
80	*	*	*	*	*	*	*	*	*	*	*	*	*	*	*	*	*	32.11	*
90	*	*	*	*	*	*	*	*	*	*	*	*	*	*	*	*	*	33.59	*
100/98/100	*	*	*	34.443	35.312	34.865	35.359	34.751	35.308	34.879	35.526	34.884	35.479	34.91	35.542	34.981	35.749	34.45	*
110	*	*	*	*	*	*	*	*	*	*	*	*	*	*	*	*	*	35.26	*
120	*	*	*	*	*	*	*	*	*	*	*	*	*	*	*	*	*	36.01	*
129/130/130	*	*	*	36.43	36.071	36.521	36.208	36.585	36.235	36.566	36.283	36.466	36.184	36.185	35.916	36.183	35.984	36.69	*
140	*	*	*	*	*	*	*	*	*	*	*	*	*	*	*	*	*	37.4	*
150	*	*	*	*	*	*	*	*	*	*	*	*	*	*	*	*	*	37.76	*

Table 3.3: Cape Sorell quartzite water saturated shear modulus measurements

Pressure (GPa) \ Frequency	1 mHz (up)	2.1 mHz (up)	4.7 mHz (up)	9.9 mHz (up)	9.9 mHz (down)	0.021 Hz (up)	0.021 Hz (down)	0.046 Hz (up)	0.046 Hz (down)	0.087 Hz (up)	0.087 Hz (down)	0.16 Hz (up)	0.16 Hz (down)	0.26 Hz (up)	0.26 Hz (down)	0.78 Hz (up)	0.78 Hz (down)	1 MHz (up)	1 MHz (down)
10	*	*	*	*	*	*	*	*	*	*	*	*	*	*	*	*	*	24.73	26.32
14	*	*	*	14.669	*	14.703	*	14.76	*	14.776	*	14.814	*	14.822	*	14.886	*	*	*
19/*/20	*	*	*	16.524	*	16.52	*	16.541	*	16.488	*	16.474	*	16.409	*	16.362	*	28.46	30.08
30	*	*	*	19.099	*	18.951	*	18.909	*	18.858	*	18.835	*	18.783	*	18.828	*	31.36	32.73
40	*	*	*	*	*	*	*	*	*	*	*	*	*	*	*	*	*	33.31	34.41
49/*/50	*	*	*	25.229	*	25.238	*	25.203	*	25.424	*	25.334	*	25.491	*	25.512	*	34.95	35.79
60	*	*	*	*	*	*	*	*	*	*	*	*	*	*	*	*	*	35.77	36.72
70	*	*	*	*	*	*	*	*	*	*	*	*	*	*	*	*	*	36.70	37.42
75	*	*	*	30.851	*	30.723	*	30.662	*	30.896	*	30.74	*	30.686	*	30.754	*	*	*
80	*	*	*	*	*	*	*	*	*	*	*	*	*	*	*	*	*	37.68	38.14
90	*	*	*	*	*	*	*	*	*	*	*	*	*	*	*	*	*	37.94	38.60
99/*/100	*	34.407	34.12	33.784	*	33.83	*	33.822	*	33.935		33.903		34.003		34.226		38.29	39.06
110	*	*	*	*	*	*	*	*	*	*	*	*	*	*	*	*	*	38.66	39.34
117/*/120	*	*	*	35.636	*	35.606	*	35.571	*	35.713		35.762		35.808		35.979		39.23	39.52
130	*	*	*	*	*	*	*	*	*	*	*	*	*	*	*	*	*	39.31	39.71
135	*	*	*	36.68	*	36.805	*	36.76	*	36.729		36.582		36.343		36.43		*	*
140	*	*	*	*	*	*	*	*	*	*	*	*	*	*	*	*	*	39.49	39.79
150	*	*	*	*	*	*	*	*	*	*	*	*	*	*	*	*	*	39.68	*

Table 3.4: Alberta quartzite dry shear modulus measurements

Pressure (GPa) \ Frequency	1 mHz (up)	2.1 mHz (up)	4.7 mHz (up)	9.9 mHz (up)	9.9 mHz (down)	0.021 Hz (up)	0.021 Hz (down)	0.046 Hz (up)	0.046 Hz (down)	0.087 Hz (up)	0.087 Hz (down)	0.16 Hz (up)	0.16 Hz (down)	0.26 Hz (up)	0.26 Hz (down)	0.78 Hz (up)	0.78 Hz (down)	1 MHz (up)	1 MHz (down)
10	*	*	*	*	*	*	*	*	*	*	*	*	*	*	*	*	*	11.89	*
20	*	*	*	*	*	*	*	*	*	*	*	*	*	*	*	*	*	14.92	20.33
30	*	*	*	*	*	*	*	*	*	*	*	*	*	*	*	*	*	18.37	22.92
40	*	*	*	*	*	*	*	*	*	*	*	*	*	*	*	*	*	21.75	24.80
50	*	*	*	*	*	*	*	*	*	*	*	*	*	*	*	*	*	23.54	26.36
60	*	*	*	*	*	*	*	*	*	*	*	*	*	*	*	*	*	25.62	29.48
70	*	*	*	*	*	*	*	*	*	*	*	*	*	*	*	*	*	27.81	30.67
80	*	*	*	*	*	*	*	*	*	*	*	*	*	*	*	*	*	29.42	31.65
90	*	*	*	*	*	*	*	*	*	*	*	*	*	*	*	*	*	30.55	32.37
100	*	*	*	*	*	*	*	*	*	*	*	*	*	*	*	*	*	31.67	33.03
110	*	*	*	*	*	*	*	*	*	*	*	*	*	*	*	*	*	32.49	33.58
120	*	*	*	*	*	*	*	*	*	*	*	*	*	*	*	*	*	33.10	33.90
130	*	*	*	*	*	*	*	*	*	*	*	*	*	*	*	*	*	33.89	34.31
140	*	*	*	*	*	*	*	*	*	*	*	*	*	*	*	*	*	34.47	34.63
150	*	*	*	*	*	*	*	*	*	*	*	*	*	*	*	*	*	34.88	*

Table 3.5: Alberta quartzite argon saturated shear modulus measurements

Pressure (GPa) \ Frequency	1 mHz (up)	2.1 mHz (up)	4.7 mHz (up)	9.9 mHz (up)	9.9 mHz (down)	0.021 Hz (up)	0.021 Hz (down)	0.046 Hz (up)	0.046 Hz (down)	0.087 Hz (up)	0.087 Hz (down)	0.16 Hz (up)	0.16 Hz (down)	0.26 Hz (up)	0.26 Hz (down)	0.78 Hz (up)	0.78 Hz (down)	1 MHz (up)	1 MHz (down)
10	*	*	*	*	*	*	*	*	*	*	*	*	*	*	*	*	*	12.06	18.45
20	*	*	*	*	*	*	*	*	*	*	*	*	*	*	*	*	*	15.99	20.95
30	*	*	*	*	*	*	*	*	*	*	*	*	*	*	*	*	*	19.31	23.24
40	*	*	*	*	*	*	*	*	*	*	*	*	*	*	*	*	*	22.70	24.70
50	*	*	*	*	*	*	*	*	*	*	*	*	*	*	*	*	*	24.51	25.70
60	*	*	*	*	*	*	*	*	*	*	*	*	*	*	*	*	*	25.67	26.33
70	*	*	*	*	*	*	*	*	*	*	*	*	*	*	*	*	*	27.75	29.71
80	*	*	*	*	*	*	*	*	*	*	*	*	*	*	*	*	*	28.97	30.71
90	*	*	*	*	*	*	*	*	*	*	*	*	*	*	*	*	*	29.93	31.40
100	*	*	*	*	*	*	*	*	*	*	*	*	*	*	*	*	*	30.87	32.11
110	*	*	*	*	*	*	*	*	*	*	*	*	*	*	*	*	*	31.88	32.87
120	*	*	*	*	*	*	*	*	*	*	*	*	*	*	*	*	*	32.56	33.26
130	*	*	*	*	*	*	*	*	*	*	*	*	*	*	*	*	*	33.41	33.89
140	*	*	*	*	*	*	*	*	*	*	*	*	*	*	*	*	*	33.97	34.22
150	*	*	*	*	*	*	*	*	*	*	*	*	*	*	*	*	*	34.54	*

Table 3.6: Alberta quartzite water saturated shear modulus measurements

Frequency

Pressure (GPa)	1 mHz (up)	2.1 mHz (up)	4.7 mHz (up)	9.9 mHz (up)	9.9 mHz (down)	0.021 Hz (up)	0.021 Hz (down)	0.046 Hz (up)	0.046 Hz (down)	0.087 Hz (up)	0.087 Hz (down)	0.16 Hz (up)	0.16 Hz (down)	0.26 Hz (up)	0.26 Hz (down)	0.78 Hz (up)	0.78 Hz (down)	1 MHz (up)	1 MHz (down)
14/*/10	*	*	*	10.851	*	10.793	*	10.803	*	10.784	*	10.768	*	10.802	*	10.778	*	21.97	24.47
21/*/20	12.716	12.618	12.474	12.293	*	12.263	*	12.249	*	12.312	*	12.291	*	12.265	*	12.216	*	24.13	29.75
30	*	*	*	15.378	*	15.394	*	15.437	*	15.473	*	15.602	*	15.565	*	15.48	*	26.91	30.22
40	*	*	*	*	*	*	*	*	*	*	*	*	*	*	*	*	*	28.73	30.93
47/*/50	*	*	*	18.932	*	18.854	*	19.093	*	19.02	*	19.01	*	19.116	*	19.105	*	29.46	32.34
60	*	*	*	*	*	*	*	*	*	*	*	*	*	*	*	*	*	30.92	32.38
66/*/70	*	*	*	25.015	*	24.894	*	25.042	*	25.005	*	25.014	*	25.111	*	25.106	*	31.53	33.75
80	*	*	*	*	*	*	*	*	*	*	*	*	*	*	*	*	*	32.47	34.45
90	*	*	*	*	*	*	*	*	*	*	*	*	*	*	*	*	*	33.21	34.67
103/*/100	29.354	28.975	28.67	28.533	*	28.272	*	28.27	*	28.281	*	28.253	*	29.054	*	29.09	*	33.82	35.07
110	*	*	*	*	*	*	*	*	*	*	*	*	*	*	*	*	*	34.47	35.58
120	*	*	*	*	*	*	*	*	*	*	*	*	*	*	*	*	*	35.22	35.75
129/*/130	*	*	*	32.506	*	32.492	*	32.524	*	32.456	*	32.55	*	32.659	*	32.71	*	35.83	36.27
140	*	*	*	*	*	*	*	*	*	*	*	*	*	*	*	*	*	36.09	36.45
150	*	*	*	*	*	*	*	*	*	*	*	*	*	*	*	*	*	36.44	*
158	*	*	*	34.659	*	34.531	*	34.533	*	34.668	*	34.616	*	34.627	*	34.644	*	*	*

4.0 Young's Modulus Dispersion

4.1 Introduction

Seismic velocities in rocks with fluid-filled cracks are expected to show a strong dependence on the frequencies at which the velocities are measured. The behaviour of the fluid in the cracks can be described by one of three regimes, depending on the timescale of measurement: "saturated isolated," where the fluid does not have time to flow between cracks, "saturated isobaric," where sufficient time exists for pore fluid pressure to flow and equilibrate between cracks and "drained," where the fluid is exchanged with an external reservoir (O'Connell and Budiansky, 1977, Jackson, 1991).

Numerous theoretical models exist, with some of the more commonly used including the self-consistent model (Budiansky and O'Connell, 1976, O'Connell and Budiansky, 1977), Hudson theory (Hudson, 1981), the Gassmann model (Gassmann, 1951), Biot theory (Biot, 1956a, 1956b) and squirt flow theory (Mavko and Jizba, 1991). The theories differ in their formulations: Gassmann theory predicts changes in bulk modulus properties related to changes in saturating pore fluid, but does not assume a particular crack or pore shape and is not limited to lower porosities. It is the theory that is believed to be the most applicable to low frequency measurements as it assumes a saturated isobaric regime. The self consistent method calculates a solution for inclusions of known shape within a background material of as-yet-unknown effective elastic stiffness, while Hudson theory deals with dilute penny-shaped cracks in a material with known elastic properties. All of these theories assume that the wavelength of the passing wave is much larger than the dimensions of the cracks or pores, and all but Gassmann theory assume that the fluid in the cracks is isolated from

neighbouring cracks. Biot and squirt flow theory predict elastic properties for materials with fluid filled inclusions at higher frequencies, although Biot theory reduces to the Gassmann equation at its low frequency limit. Biot theory predicts the result of the inertial interaction between pore fluid and the rock matrix on the effective elastic properties, while squirt flow theory estimates local fluid flow effects at the grain scale.

Theoretical models of dispersion have long been hindered by the difficulty of testing the models experimentally. Comparison between in-situ and laboratory results is complicated by issues of heterogeneity and scale, while low frequency measurements are difficult to make in the laboratory setting as a result of the sensitivity of the elastic moduli to the amplitude of strain applied (Batzle *et al.*, 2006). Experimental work on cracked rock has increased in recent years (e.g. Adam *et al.*, 2006, Batzle *et al.*, 2006, Adelinet *et al.*, 2010), however, these measurements remain few and far between, and there are few apparatuses capable of making low frequency laboratory measurements in the seismic strain regime. Recently, ANU (Australian National University) developed the capability of measuring low frequency Young's moduli (Jackson *et al.*, 2011). The ANU apparatus had previously been regularly used for low frequency shear moduli measurements (Jackson and Paterson, 1993), and recent modification now allows both the shear and Young's moduli to be measured at frequencies of 1 mHz – 1 Hz over a range of pressures and under a variety of saturation regimes.

In this study, low (0.01-1 Hz) and high (1 MHz) frequency Young's modulus experimental measurements were made on two quartzites; one from Cape Sorell, Australia and one from Alberta, Canada. Both quartzites had thermally induced low aspect ratio cracks. The Young's modulus was measured while the quartzites were dry,

argon saturated and water saturated across a range of effective pressures (10-150 MPa). Low frequency measurements were made using the forced flexural oscillation apparatus newly developed at Australian National University (ANU), while high frequency measurements were made using the relatively standard ultrasonic pulse technique at the University of Alberta. Here, the low frequency Young's modulus measurement method is described, and the low frequency measurements are compared to their 1 MHz counterparts. The Young's modulus of the quartzites showed significant stiffening with water saturation at high frequency, and significant dispersion was observed. The dispersion measurements were compared to the predictions of Gassmann theory and to predictions incorporating the high frequency limit of Biot and squirt flow theory.

4.2 Low frequency measurements

4.2.1 ANU apparatus flexural measurement theory

Low frequency Young's modulus measurements were undertaken using the ANU apparatus (Jackson *et al.*, 2011). The apparatus is an approximately 1 m long beam cantilevered at the top and propped at the lower boundary. A ~150 mm long specimen is located near the top of the beam and is sandwiched between two hollow polycrystalline (Duramic™) alumina rods; the specimen assembly is jacketed. Below the specimen assembly is an elastic element, comprised of a hollow steel tube. Flexure is measured by parallel plate capacitors between the specimen assembly and elastic element and below the elastic element, at distances l_1 and l_2, respectively, below the upper cantilevered end of the assembly. The beam is sinusoidally driven by

electromagnetic drivers moving in opposition at the bottom of the beam, at l_3 (Figure 4.1). The parallel plate capacitors measure a displacement $d_i(t)$ with time t at a distance D from the axis of the beam:

$$d_i(t) = Dv'(l_i, t) \qquad \text{i=1,2} \qquad (4.1)$$

Here v' is the angle of flexure, dv/dx.

These displacements are used to calculate a normalized flexural modulus, S_{NF}, which is the ratio of change in angle of flexure across the specimen assembly to that for the elastic element:

$$S_{NF} = \left| \frac{d_1}{d_2 - d_1} \right| = \left| \frac{v'(l_1)}{v'(l_2) - v'(l_1)} \right| \qquad (4.2)$$

The flexure of the beam at any given point is controlled mainly by longitudinal extension and contraction, and is related to the Young's modulus, E, the diametral moment of inertia, I, and the local bending moment, M, through the equation:

$$E(x)I(x)\frac{\partial^2 v}{\partial x^2} = -M(x) \qquad (4.3)$$

The local bending moment is related to the bending moment applied at $x = l_3$, M_a, and the lateral reaction force at the propped end of the beam, R_L:

$$M(x) = R_L(L - x) - M_a \qquad 0 \le x < l_3 \qquad (4.4)$$

$$M(x) = R_L(L - x)) \qquad l_3 < x \le L \qquad (4.5)$$

where L is the lower, propped end of the beam.

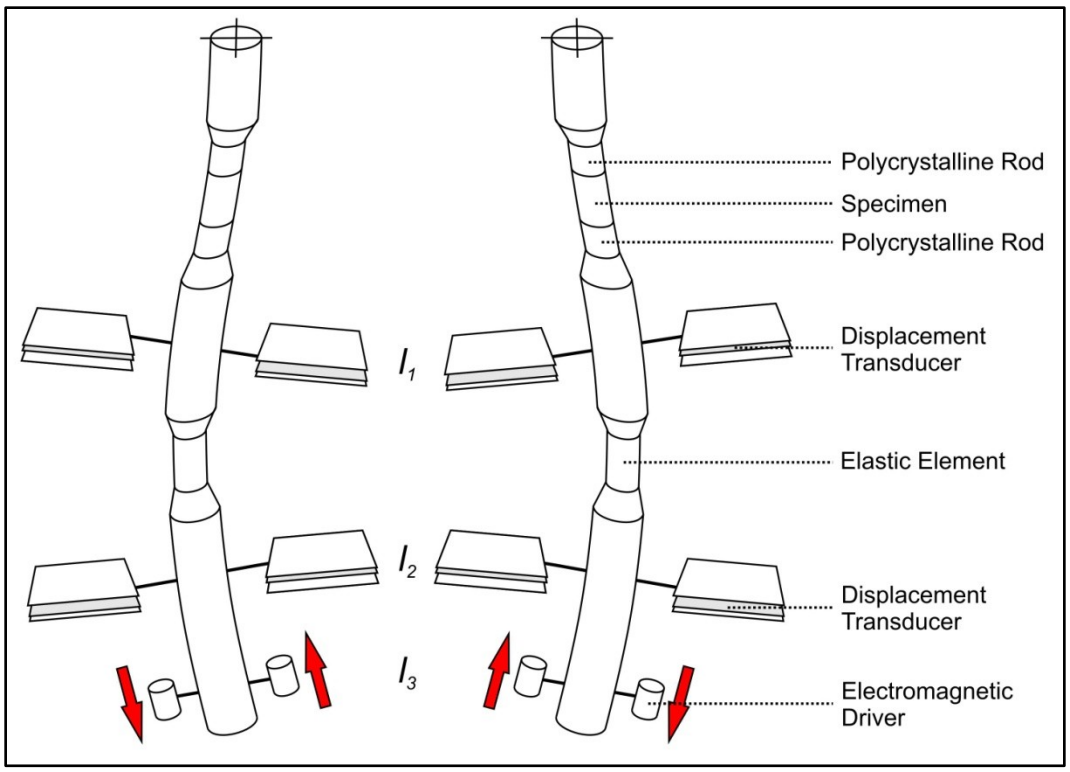

Figure 4.1: Schematic of the low frequency apparatus in flexural mode showing exaggerated flexure. The top of the apparatus is held vertical while the bottom is held in place but allowed to vary in angle.

Substituting Equation 4.4 into Equation 4.3 and integrating allows for *v'* at $x < l_3$ to be solved for:

$$v'(x) = M_a \int_0^x \frac{1}{E(x)I(x)}dx - R_L \int_0^x \frac{(L-x)}{E(x)I(x)}dx \tag{4.6}$$

The normalized flexural modulus is therefore related to the Young's modulus of the beam by substituting Equation 4.6 into Equation 4.2:

$$S_{\text{mod}} = \left| \frac{M_a \int_0^{l_1} \frac{1}{E(x)I(x)}dx - R_L \int_0^{l_1} \frac{(L-x)}{E(x)I(x)}dx}{M_a \int_{l_1}^{l_2} \frac{1}{E(x)I(x)}dx - R_L \int_{l_1}^{l_2} \frac{(L-x)}{E(x)I(x)}dx} \right| \tag{4.7}$$

Here S_{mod} is the theoretical value of the normalized modulus, as opposed to S_{NF} which is the measured value. Where the shear stress at the interfaces between adjacent filaments is negligible, as demonstrated by Jackson *et al.* (2011), S_{mod} and S_{NF} should be equivalent. In order to solve for S_{mod} using finite difference code in MATLAB™, the beam is discretized into *N* intervals of length $h = L/N$. The second derivative of displacement, *v"*, can then be calculated:

$$v''(x_i) = \frac{\frac{v_{i+1} - v_i}{h} - \frac{v_i - v_{i-1}}{h}}{h} = \frac{v_{i-1} - 2v_i + v_{i+1}}{h^2} \tag{4.8}$$

This can be substituted into Equation 4.3:

$$v_{i-1} - 2v_i + v_{i+1} = \frac{h^2 M_i}{E_i I_i} \tag{4.9}$$

The boundary conditions of a cantilevered, propped beam require that $v(x_0) = v(x_N) = 0$ and that $v'(x_0) = 0$, which requires $v(x_{-1}) = v(x_1)$. These conditions are applied, and the N simultaneous linear equations are solved (Jackson *et al.*, 2011):

$$\frac{h^2 L}{E_0 I_0} R_L + 2v_1 = \frac{h^2 M_a}{E_0 I_0} \qquad i = 0 \qquad (4.10)$$

$$\frac{h^2 (L - x_i)}{E_i I_i} R_L + v_{i-1} - 2v_i + v_{i+1} = \frac{h^2 M_a}{E_i I_i} \qquad i \geq 1,\ 0 \leq x_i < l_3 \qquad (4.11)$$

$$\frac{h^2 (L - x_i)}{E_i I_i} R_L + v_{i-1} - 2v_i + v_{i+1} = 0 \qquad i < N,\ l_3 < x_i \leq L \qquad (4.12)$$

S_{mod} is calculated from the local x-derivative of v_i at $x = l_1$ and $x = l_2$. The Young's moduli and diametral moments of inertia of the components of the steel beam and the copper jacket of the specimen assembly are accurately known at standard pressure, however, as effective pressures of up to 200 MPa are applied it is necessary to account for changes in these parameters. These changes are estimated based on published values for the changes in shear and Young's moduli with pressure (Simmons and Wang, 1971).

4.2.2 Calibration of the ANU apparatus

During this experimental study it was desired to deliver pore fluids to the sample. The sample, which was precision ground to a 15 mm diameter, was therefore sandwiched within the specimen assembly between two hollow polycrystalline alumina rods which allowed fluid to flow from the pore fluid reservoirs into the sample. While the dimensions of the polycrystalline alumina rods were well-measured, their Young's modulus was not accurately known. In order to determine their effective elastic

stiffness, measurements were made while they sandwiched a fused quartz sample of known elastic stiffness in order that their Young's modulus was the only unknown in the system. Fused quartz is a commonly used standard; the Young's modulus of the fused quartz sample used here was measured using ultrasonic interferometry and found to be 72.6 GPa, similar to values found in other published literature (e.g. Gerlich and Kennedy, 1978, Meister *et al.*, 1980). The pressure dependence of its dimensions and Young's modulus was estimated from values measured by Ohno *et al.* (2000), G'=-3.5 and K'=-6.0.

Experimental measurements of the fused quartz assembly were made in two separate runs, #1206 and #1208[1], over a range of effective pressures. During run #1206, the fused quartz was enclosed bare within the copper jacket, and argon pore pressure was introduced during measurements at 28 MPa and 103 MPa of effective pressure. During run #1208, only confining pressure was used, but the fused quartz was wrapped in Teflon tape before being inserted in the copper jacket in an effort to further minimize the possibility of fluid flow along the boundary of the sample in future measurements where pore fluid could potentially be used. Measurements from run #1208 did not appear to agree well with the measurements of run #1206, likely due to issues with the Teflon, such as not accounting for the additional diameter added to the assembly by the tape. Run #1206 was therefore used to determine the normalized modulus of the fused quartz assembly, and permeability measurements later showed that longitudinal fluid flow along the jacket-sample boundary was negligible. Comparison of the #1206

[1] Each pressurization cycle of the ANU apparatus since conception has a unique, sequential run number. Pressurization is required for specimen jacket collapse (e.g. run #1207), and a pressurization cycle does not necessarily include data measurement.

measurements made with confining pressure only versus those made with pore pressure showed good agreement, indicating that lateral fluid flow between the side of the sample instantaneously in compression and the side in extension was also minimal along the sample boundary. Teflon tape was therefore not used in any of the experimental measurements.

The normalized modulus of the assembly was found to be pressure dependent, well in excess of the pressure dependence that could be accounted for by the variation in Young's moduli or the dimensions of components of the beam (Fig. 4.2). This was not fully understood, however, it was hypothesized that the change in compliance was caused by interfacial effects between the fused quartz, the alumina rods and the rest of the assembly, as these components were coupled solely by friction and could potentially undergo a slight amount of creeping during measurement. A combination of the Young's modulus of the alumina rods and the interfacial coupling effects was captured by allowing the effective Young's modulus of the polycrystalline alumina to vary with pressure over and above the E' = 4.7 measured by Gieske and Barsch (1968). A 3rd order polynomial was fitted to the normalized modulus measurements of the fused silica assembly (Fig. 4.2). The Young's modulus of the alumina rods sandwiching the fused quartz specimen was varied within the finite difference model until the calculated normalized modulus, S_{mod}, matched the value calculated from the curve fit to the experimental fused quartz normalized moduli, S_{NF}. Thus the flexural oscillation data for the fused quartz assembly were effectively used to solve for the least well constrained parameter, namely a mildly pressure dependent effective Young's modulus for the hollow alumina rods.

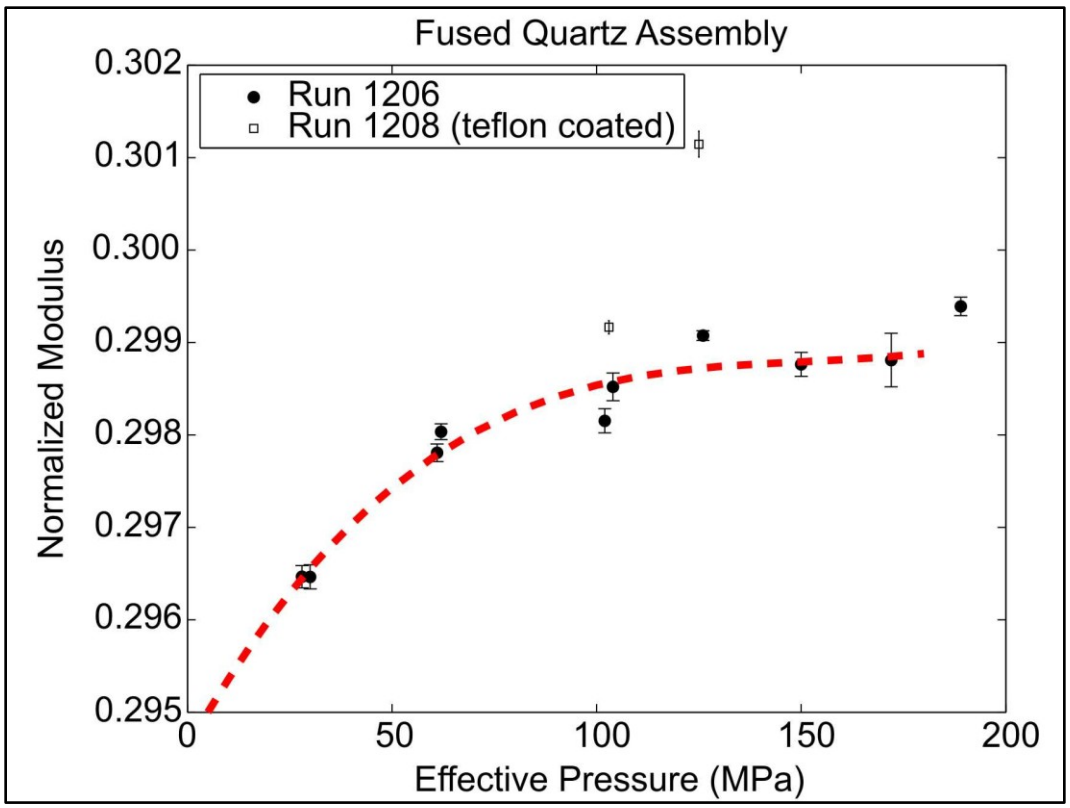

Figure 4.2: Normalized modulus of fused quartz assembly measured over a range of effective pressures, showing the dependence of the normalized modulus of the assembly on effective pressure – approximated by the third order polynomial function represented by the dashed curve.

The normalized flexural modulus calculated by the finite difference model was somewhat dependent on the number of elements, *N*, used in the calculation. The model solution typically converged when the beam was discretized into >2500 parts, however, due to discretization effects as well as machine precision, some scatter remained (Fig. 4.3). In order to have consistent quality in the results of the model, the normalized modulus was calculated multiple times using different discretization regimes, and averaged. The normalized modulus for a beam of 4100 to 5000 elements, in increments of 100, was calculated for a total of 10 normalized flexural modulus calculations. The mean of these 10 moduli was taken to be the converged normalized modulus. In practice, the maximum observed standard deviation in the set of ten normalized moduli was 8×10^{-5}; and the average standard deviation was 5×10^{-5}. In order to save processing time, when the standard deviation of the normalized moduli is $<5 \times 10^{-5}$ after a minimum of four normalized modulus calculations, the compliance was deemed to have converged and in these cases the mean of these compliances was used as the converged compliance even though the mean was based on a fewer number of calculations. A standard deviation of 5×10^{-5} translated to an error of <0.02% for the unitless normalized moduli measured experimentally, however, this refers only to the error caused by discretization and machine precision. The overall experimental error was typically larger, as discussed later in the text.

The rods required an effective Young's modulus varying mildly with pressure from 235 GPa at 5 MPa of pressure to 272 GPa at 190 MPa of pressure to return theoretical normalized moduli equal to those measured experimentally for the fused quartz specimen assembly (Fig. 4.4). Unfortunately, no published results for Duramic

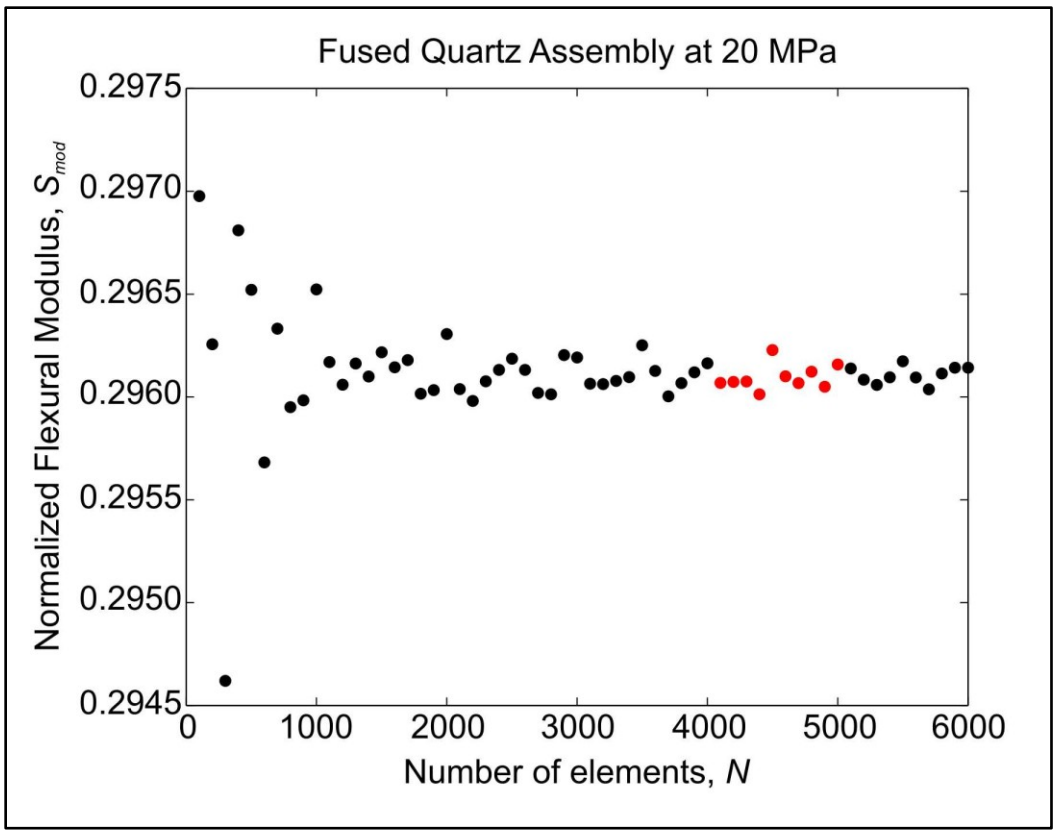

Figure 4.3: Normalized modulus calculated using the finite difference model as a function of the number of elements, *N*, used in the calculation for the fused quartz assembly at a confining pressure of 20 MPa, showing the convergence of the modulus for $N > 2500$. The 10 results from N=4100-5000 that are averaged to produce the accepted value of the modulus are shown in red.

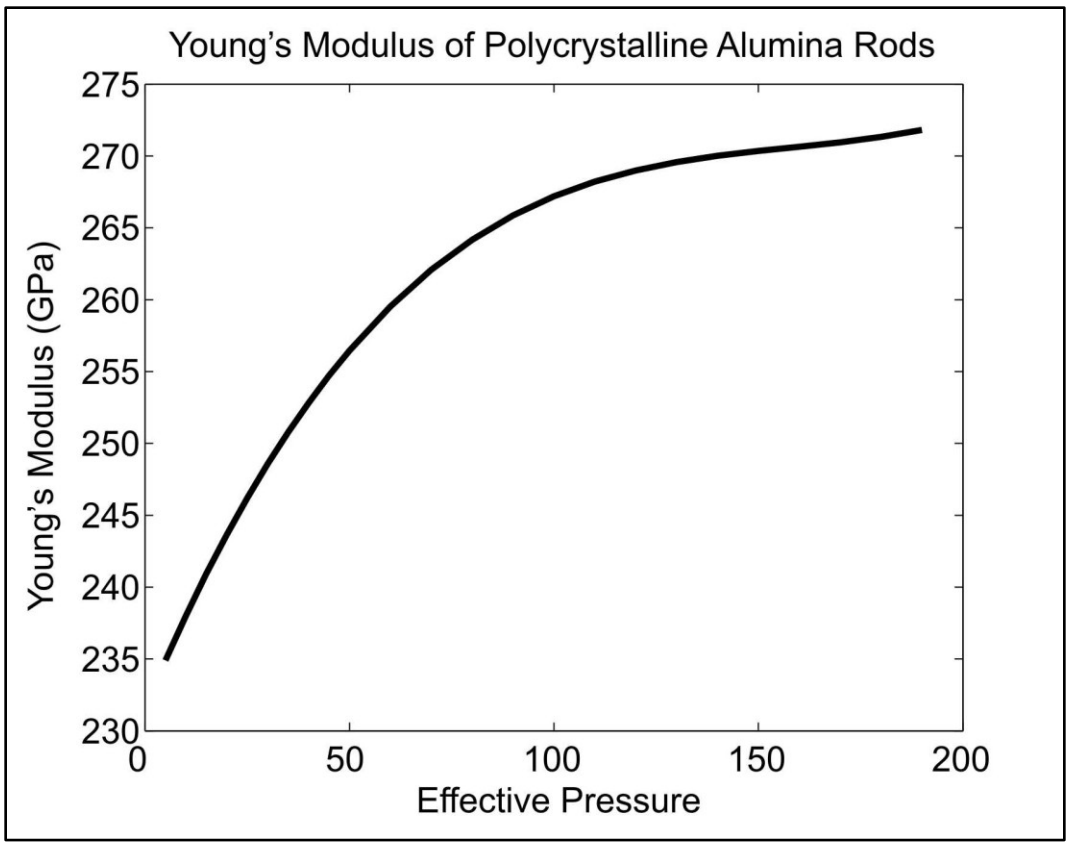

Figure 4.4: The effective Young's modulus of the polycrystalline alumina rods required for the finite difference code to return an S_{mod} value equal to the normalized moduli, S_{NF}, measured experimentally by run 1206 with a fused quartz assembly.

polycrystalline alumina were found, however, these values do not appear unreasonable when compared to published results for Lucalox polycrystalline alumina which measure a Young's modulus on the order of 400 GPa (Schreiber and Anderson, 1965). Lucalox is a purer, less porous ceramic; the increased material porosity of the Duramic alumina, both intrinsic porosity and crack porosity induced by repeated pressure and high temperature cycling during repeated experimental use of the Duramic rods, would be expected to result in a much reduced Young's modulus. Further, the compliance at the interfaces between the rods and the fused quartz specimen was likely not negligible. The ends of the rods were ground but not lapped, while the ends of the fused quartz sample were lapped.

Substitution of these Young's modulus values for the alumina rods into the finite difference model meant that, when the fused quartz was replaced by another sample specimen, the Young's modulus of the sample specimen was the only unknown. This allowed the unknown Young's modulus of a sample to be measured using the apparatus, through the change in the experimental response relative to that for the standard fused quartz.

4.2.3 Low frequency Young's modulus measurements on experimental samples

Two quartzite samples, one from Cape Sorell, Australia, and one from Alberta, Canada, were chosen for measurement. The shear moduli of the two samples had previously been measured under similar saturation and pressure conditions across a similar range of frequencies to those measured here; in addition, the porosity, permeability and composition of the quartzites has been well characterized (see Chapter 3). The quartzites had been thermally cracked by heating to 1100°C and

quenching in liquid nitrogen (for the Cape Sorell quartzite) and water (for the Alberta quartzite). After cracking, the quartzites both had low aspect ratio (i.e. aperture to diameter ratio of ~0.001) cracks. At ambient pressure, the porosity of the Cape Sorell quartzite was 2.3% and that of the Alberta quartzite was 2.4%. Their permeabilities were 5×10^{-20} m^2 and 3×10^{-19} m^2, respectively, at low effective pressure but had been measured to decrease with pressure as crack closure was effected.

Flexural measurements were made on the Cape Sorell quartzite under dry, argon saturated and water saturated conditions, as well as on the dry Alberta quartzite. It was not possible to measure the saturated Alberta quartzite in flexural mode due to bending of the sample under pressure. Although the magnitude of the bending was extremely small, it nonetheless rendered the measurements impossible as the bending caused the sample to rub on the sides of the pressure vessel and introduced additional stiffness into the system which could not be properly quantified. Saturated measurements of the Cape Sorell quartzite were made following pore pressure equilibration throughout the specimen by fluid flow from the lower to the upper reservoir. The Young's moduli at frequencies 0.01 - 1 Hz were numerically modelled using the experimentally determined values for the Young's modulus of the polycrystalline alumina rods. Errors in the Young's moduli of the quartzites were estimated from the Young's moduli measurements of the fused quartz. As the Young's modulus of the fused quartz itself can be expected to be independent of frequency as a result of the extremely low attenuation of the non porous material, any frequency-dependent variation must be as a result of measurement error. Each fused quartz measurement was undertaken at 7 frequencies at equal logarithmic spacing between 0.01 - 1 Hz. At each pressure, the

small error observed in the fused quartz measurement at different frequencies was likely a result of minor noise in the movement of the electromagnetic flexural drivers due to higher order harmonics (Fig. 4.5) as well as the interaction of the parallel plate capacitors measuring the flexure of the beam with the argon pressurizing fluid. The parallel plate capacitors of the apparatus are exposed to the argon induced confining pressure, with the central plate of the triple plate capacitor moving through the argon fluid. At high confining pressures the viscosity of the argon is increased and may have caused a small amount of drag on the moving capacitor plate, particularly at higher frequencies. In the fused quartz measurements, the average standard deviation in the measurement of the normalized modulus at each pressure was 0.04%; the standard deviation in the experimental measurements did not appear to have any pressure dependence. The error in the normalized modulus measurement was assumed to be two standard deviations, 0.1%, in order to reasonably encompass the majority of the data. The errors in the Young's moduli of the quartzites were propagated by modeling the moduli resulting from this error estimate in normalized modulus: the Young's modulus corresponding to a normalized modulus 0.1% larger and one 0.1% smaller than measured was calculated, and half of this range was used as the error in the Young's modulus. There may be other errors in the low frequency Young's modulus measurements, such as those relating to the calibration of the moduli for the alumina rods. Further, as discussed previously, the normalized modulus could only be solved for within a <0.02% error and this error estimate should be taken as a minimum error.

The error of 0.1% in the normalized modulus may appear quite small; however, the fairly low sensitivity of the apparatus to the Young's modulus means that even quite

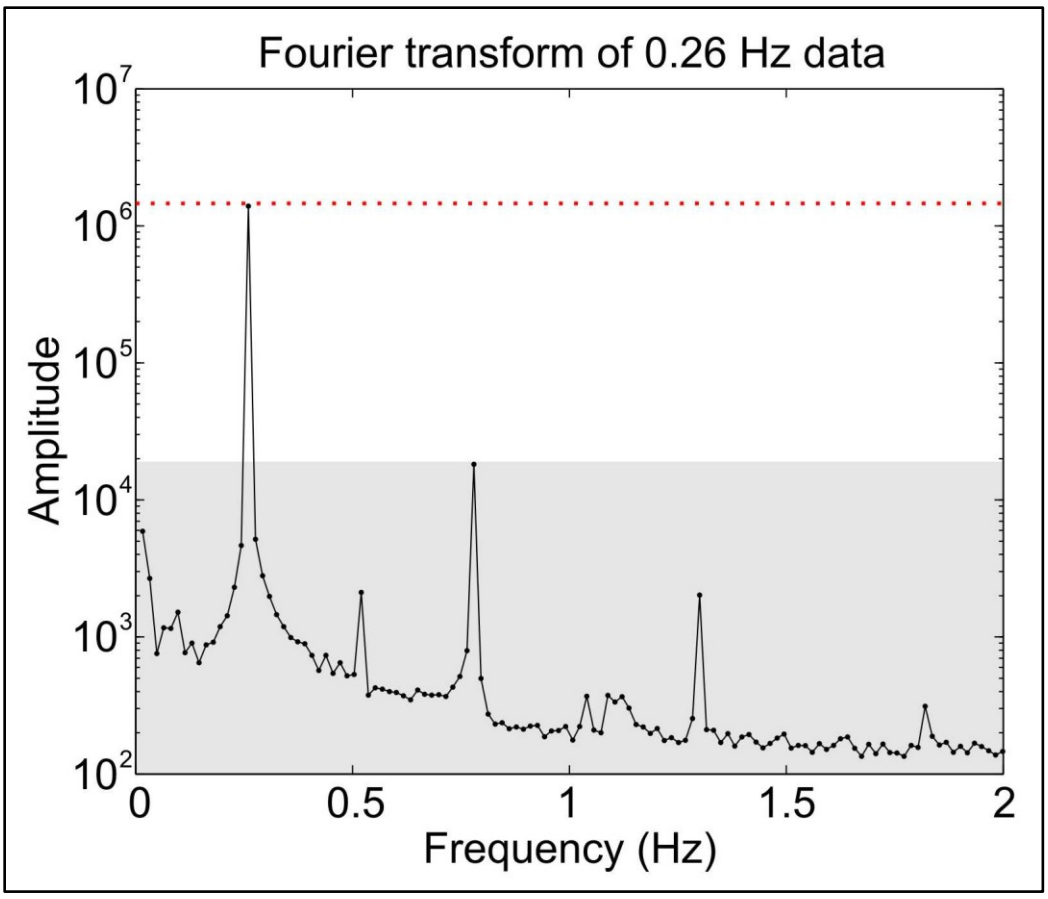

Figure 4.5: Fourier transform of raw flexural data at 0.26 Hz (black), showing the signal level of the 0.26 Hz driving frequency (red dotted line) is approximately two orders of magnitude greater than harmonic and other noise (shaded area).

small variations in the normalized modulus can indicate larger magnitude errors in the Young's modulus. Measurements of Young's moduli at high effective pressure, in particular, have significantly higher errors due to the lower sensitivity of the apparatus with increasing sample stiffness. This is a result of the location of the sample within the apparatus: maximum flexure occurs between the two measuring locations, l_1 and l_2, and near the top of the cantilevered beam, with relatively little occurring in the specimen itself (Fig. 4.6). As evidenced in Equation 4.3, the curvature of the assembly is greatest where the assembly has both a low Young's modulus and low moment of inertia. The normalized compliance reflects the relative gradients at l_1 and l_2, which are influenced by the geometry and material properties of the assembly. For a given effective pressure and associated Young's modulus of the Duramic rods sandwiching the specimen, there is in fact a maximum modulus that can be returned by numerical modeling. This occurs when the Young's modulus of the specimen is high enough that no flexure is induced in the specimen during measurement. The maximum theoretical normalized modulus is then controlled exclusively by the flexure occurring within the other components of the apparatus; the contribution of the polycrystalline alumina rods is the only component which has not been independently measured. Experimentally, however, the theoretical maximum of the normalized modulus has been exceeded in some cases, with experimental measurements of the modulus at times larger than the maximum modulus achievable with the current numerical modeling program.

A discrepancy between measurements and modeling arose for the water saturated quartzite samples, which consistently had experimental normalized moduli

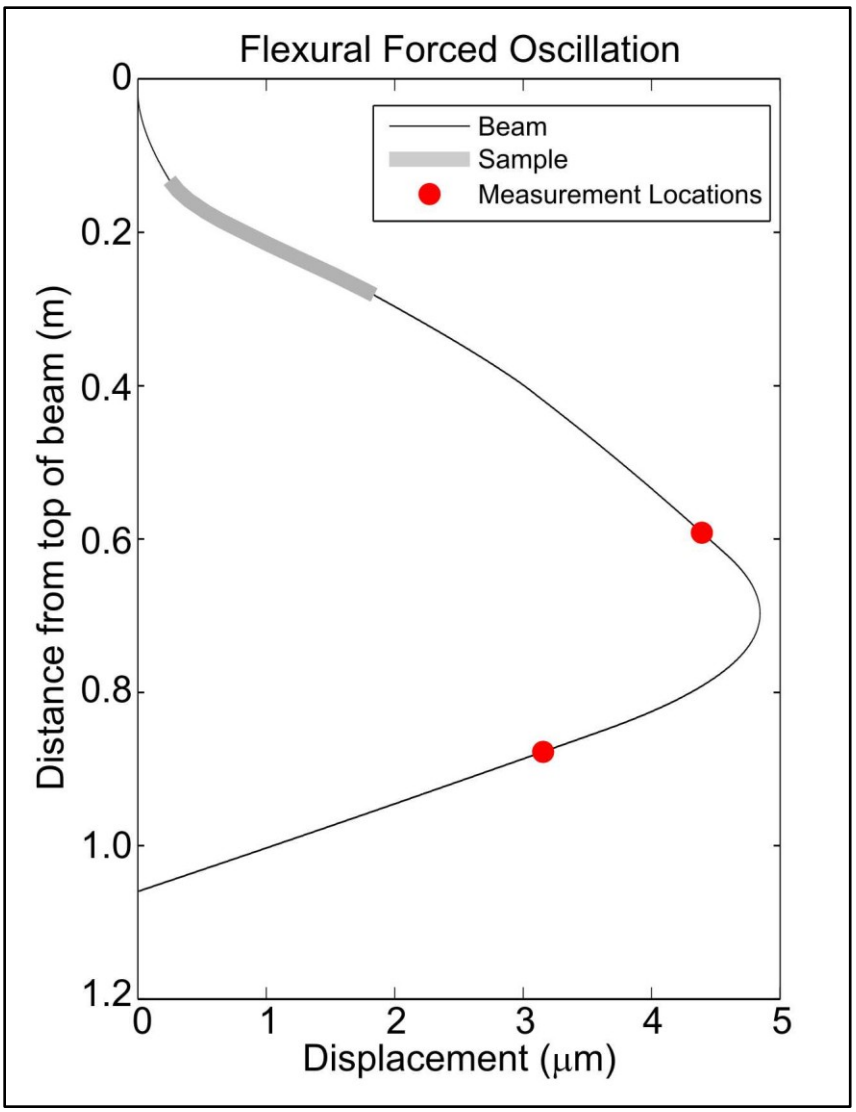

Figure 4.6: Typical displacement along the beam of the apparatus while in flexural mode, with red points showing locations l_1 and l_2 where the parallel plate capacitors measure flexure. Note that the diagram is horizontally exaggerated.

measurements that were higher than those theoretically possible with the Young's modulus values of the polycrystalline alumina rods calibrated from run #1206. At this early stage of technique development the origin of this additional stiffness in the apparatus is incompletely understood, although it may be related to the influence of water within alumina rods cracked from prior thermal cycling or to the interfacial coupling between the components of the assembly. Time constraints meant that the Young's modulus of the polycrystalline rods had been measured through the use of the fused quartz standard only while dry and argon saturated, and not while saturated with water pore fluid. It was therefore not possible to estimate the effect of water saturation on the Young's modulus of the rods. The additional stiffening observed was assumed to be a consistent system response and, along with the interfacial coupling effects, was captured within the Young's modulus value of the polycrystalline alumina rods through modeling of the water saturated quartzites: it was assumed that at high effective pressures the cracks in the quartzites would be effectively closed and the Young's modulus of the rocks would have a linear relationship with pressure. Such a linear variation of the Young's moduli measured on the Cape Sorell quartzite, both dry and argon saturated, at effective pressures >75 MPa and at a frequency of 0.09 Hz (during both loading and unloading) was used to estimate a value for the low frequency Young's modulus at 140 MPa effective pressure. The water saturated Cape Sorell quartzite had been measured at 140 MPa and 142 MPa of effective pressure at low frequency, and the stiffness of the polycrystalline alumina rods was adjusted so that the average of the normalized moduli of these two water saturated measurements at 0.09 Hz returned the same Young's modulus as the normalized modulus for the dry and argon saturated measurements at 140 MPa. This required an 89.5 GPa increase in the

effective Young's modulus of the alumina rods. As a first approximation to the system response, this 89.5 GPa correction was assumed to be independent of pressure. All other water saturated measurements were then modeled with a Young's modulus for polycrystalline alumina subject to the same upward adjustment, based on the assumption of identical Young's moduli of the Cape Sorell quartzite measured at 140 MPa whether dry, argon or water saturated.

4.3 High frequency measurements

High frequency measurements were made on both of the quartzites at 1 MHz using piezoelectric transducers. The samples were placed between two aluminum buffers affixed with P- and S-wave piezoelectric transducers. Argon and water were introduced through a small opening in one of the buffers. For safety reasons, argon pore fluid pressure was maintained at 10 MPa for argon saturated measurements, and effective pressures were achieved by varying the confining pressure only. In the case of water saturation however, the confining pressure was kept fixed and the water pore fluid pressure was varied to obtain the desired effective pressure. Traveltime measurements were made for both P- and S-waves under dry, argon saturated and water saturated conditions from 10-150 MPa of effective pressure. P- and S-wave velocities through the quartzites were determined by accounting for travel-times through the aluminum buffers and dimensional changes of the quartzites based on pure quartz mineralogy, as the quartzites have been shown to have only minimal contamination by other minerals. S-wave and shear modulus measurements are described in the previous chapter. Seismic velocities were then used in conjunction with

the bulk density of the quartzites to calculate the Young's moduli under the various pressure and saturation conditions. As in Equation 2.18 the P-wave velocity can be described by the bulk density, shear and Young's moduli; combining Equation 2.18 with Equation 2.19, which describes the S-wave velocity in terms of the bulk density and shear modulus allows the isolation of the Young's modulus:

$$E = \frac{\rho v_S^{\,2}\left(3v_P^{\,2} - 4v_S^{\,2}\right)}{v_P^{\,2} - v_S^{\,2}} \tag{4.13}$$

where ρ is the bulk density, v_P the P-wave velocity and v_S the S-wave velocity.

4.4 Results

The low frequency Cape Sorell quartzite measurements were made by frictionally coupling three 5 cm long pieces in series to achieve the 15 cm sample length necessary for the apparatus, while the Alberta quartzite sample was composed of a single 15 cm long core. The Alberta quartzite had been precision ground to the necessary 1.5 cm diameter after thermal cracking was used to induce low aspect ratio cracks. The Cape Sorell quartzite, however, was precision ground prior to thermal cracking. While the thermal cracking technique was quite successful at inducing a relatively isotropic, randomly oriented distribution of cracks, it was not perfect and, during crack closure under pressurization, the cylindrical Alberta quartzite sample acquired a very slight curvature. Lateral clearance in the low frequency apparatus is quite small, and it was difficult to orient the quartzite in such a manner that the pressure-induced curvature did not cause the quartzite to contact the sides of the pressure vessel when the sample

was undergoing forced oscillation. While the Cape Sorell quartzite was measured at low frequency under dry, argon and water saturated conditions, the Young's modulus of the Alberta quartzite was only successfully measured while dry, and for confining pressures <100 MPa. High frequency measurements were possible under all saturation and pressure conditions for both quartzites due to the different mechanism of measurement (Figs. 4.7, 4.8, 4.9).

The Young's moduli of the quartzites behaved similarly to the shear moduli (see chapter 2), showing a significant increase in stiffness from 0-80 MPa of effective pressure, apparently reflecting crack closure, before entering a regime with milder, linear pressure dependence at pressures >80 MPa.

As expected, no frequency dispersion occurred in the dry quartzites. The low and high frequency measurements showed good agreement across the measured frequency bands from 0.01 Hz – 1 MHz. The Young's modulus of the Alberta quartzite agreed particularly well, while the Cape Sorell quartzite exhibited a minor but somewhat systematic difference between its low and high frequency results at 10 and 20 MPa of pressure where low frequency measurements had slightly lower Young's moduli.

When the Cape Sorell quartzite was saturated with argon pore fluid, its behaviour was similar to when it was dry. If dispersion was occurring, it was of low amplitude, as the low and high frequency Young's modulus measurements broadly agreed. The Alberta quartzite was not measured at low frequency while argon or water saturated; it was therefore only possible to compare its high frequency argon saturated

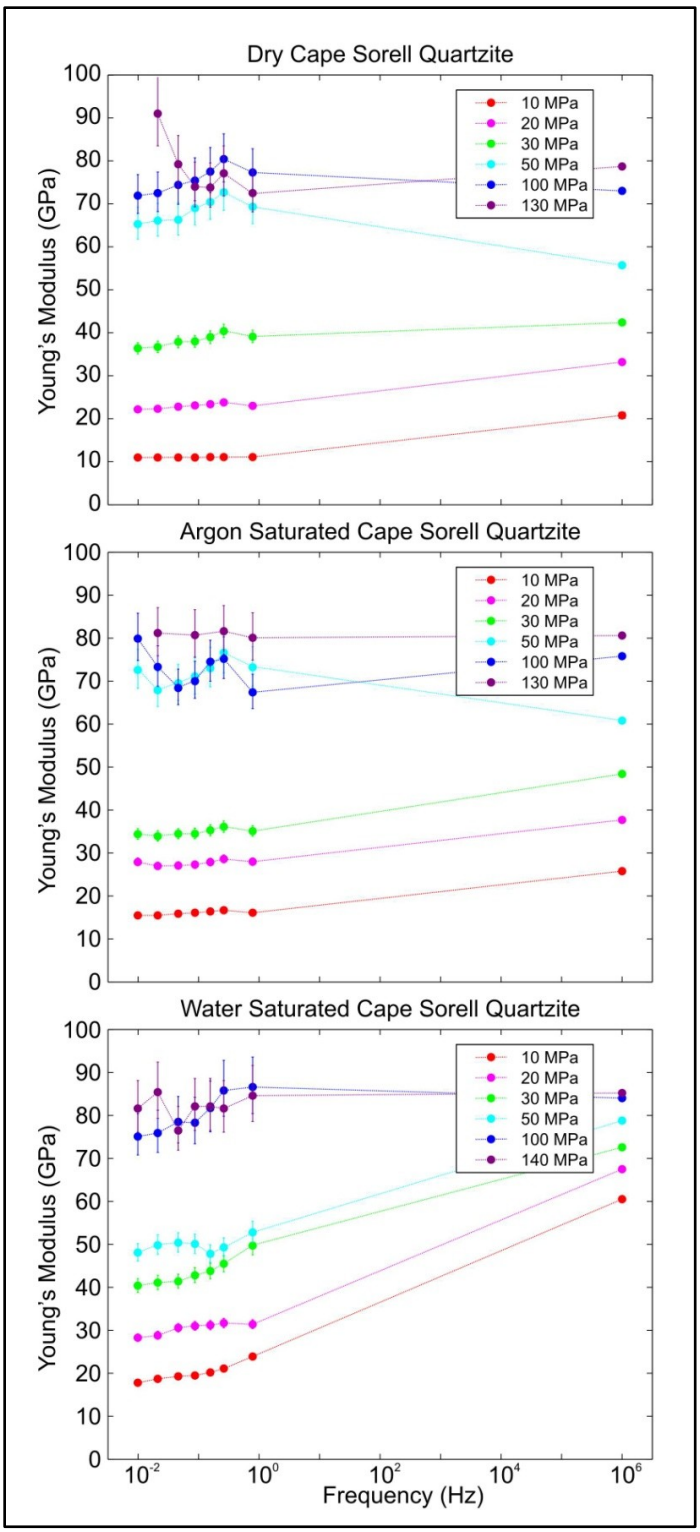

Figure 4.7: Dispersion measurements of Cape Sorell quartzite, showing low (0.01-1 Hz) and high (1 MHz) measurements with the sample dry (top), argon saturated (middle) and water saturated (bottom) at various effective pressures.

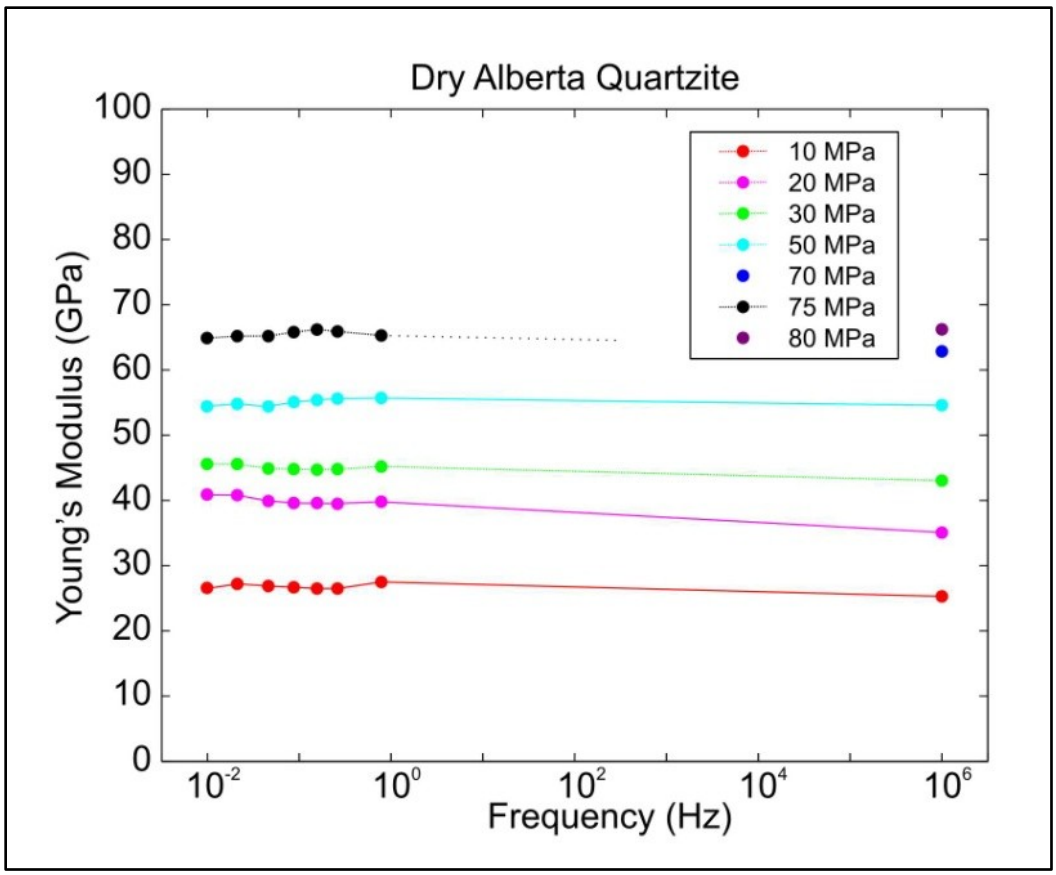

Figure 4.8: Dispersion measurements of the Young's modulus of the Alberta quartzite, showing low (0.01-1 Hz) and high (1 MHz) measurements on the dry sample over a range of confining pressures.

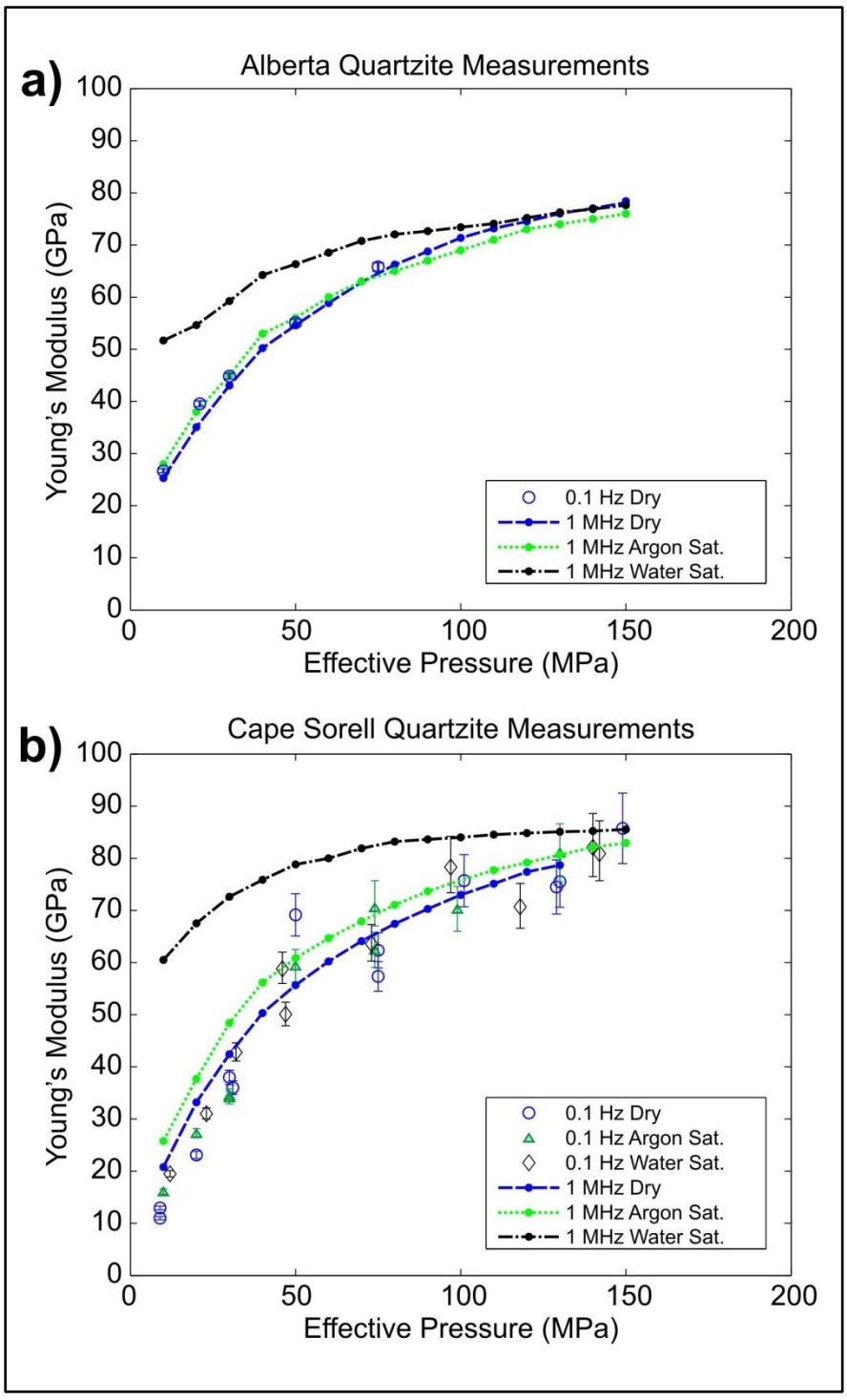

Figure 4.9: Measurements on the dry Alberta quartzite (a) at 0.1 Hz, and dry, argon saturated and water saturated Alberta quartzite at 1 MHz, as well as measurements on the dry, argon saturated and water saturated Cape Sorell quartzite quartzite (b) at 0.1 Hz and 1 MHz, showing the significant stiffening of the Young's modulus with water saturation.

measurements to its dry measurements. At low effective pressures, both the Alberta and the Cape Sorell quartzite showed some slight additional stiffening in their Young's moduli at high frequency when saturated with argon compared to when dry. The 1 MHz argon saturated Cape Sorell quartzite Young's modulus was 24.1% higher than when measured dry at 10 MPa of effective pressure (25.8±0.4 GPa versus 20.8±0.7 GPa). Meanwhile, the Alberta quartzite had an argon saturated Young's modulus that was 12.5% higher than its dry counterpart at the same effective pressure (28.0±0.2 GPa compared to 25.3±0.3 GPa). At higher effective pressures (>70 MPa), however, the 1 MHz argon saturated Young's modulus of the Alberta quartzite was lower than the dry Young's modulus. Similarly, when the Alberta sample was saturated with water at high pressure, the Young's modulus was again lower than the dry Young's modulus.

Substantial dispersion was observed when the Cape Sorell quartzite was saturated with water; the Young's modulus was seen to increase slightly from 0.01 Hz to 1 Hz and a significant increase in stiffness is measured between 1 Hz and 1 MHz. This difference in behaviour between the argon and water saturated specimens was not unexpected as the properties of the liquid water and supercritical argon fluids differ greatly. At the experimental temperatures and pressures the viscosity of water is 0.001 Pa·s (NIST, 2012), 40 times greater than that of argon. The incompressibility of water is also much higher, ranging from 2.2 – 3.0 GPa over the range of pressures measured, more than 200 times higher than that of argon. At 10 MPa effective pressure, the water saturated Cape Sorell quartzite had a Young's modulus of 60.5±0.1 GPa when measured at 1 MHz: almost three times larger than the modulus of 23.9±0.8 GPa measured at 1 Hz and 12 MPa of pressure. At 0.01 Hz, the water saturated measurement was lower

still, approaching the low frequency dry and argon saturated values measured at similar effective pressures, with a Young's modulus of only 17.8±0.6 GPa. Although the Alberta quartzite was not measured at low frequency while water saturated, it could be expected to show similar dispersion results as at high frequency the Young's modulus increased from 25.3±0.3 GPa when dry to 51.7±0.1 GPa when water saturated.

This strong dispersion in the Young's modulus can be expected to impact comparisons between seismic surveys and ultrasonic measurements as it translates to a significant dispersion of the P-wave velocity as well. Using an interpolated value for the water saturated Young's modulus at 0.1 Hz, it was possible to calculate the low frequency P-wave velocity of the Cape Sorell quartzite (with shear modulus measurements reported in Chapter 3), 2882±6 m/s at 14 MPa of effective pressure. At 1 MHz the velocity was substantially higher, 5120±20 m/s at 10 MPa of effective pressure, indicating a minimum of 56% dispersion at these pressures when the sample was water saturated (Fig. 4.10).

4.5 Modeling

In order to assess the accuracy of various theoretical models for a cracked specimen it is necessary to compare experimental results with those calculated from commonly used theories. The Biot (1956a, 1956b) model is frequently used to predict moduli at high frequencies. However, in cracked materials, dispersion as a result of "squirt" flow is considered to be at least as important as Biot dispersion (Mavko and Jizba, 1991), and the two theories can be combined to provide an estimate of the

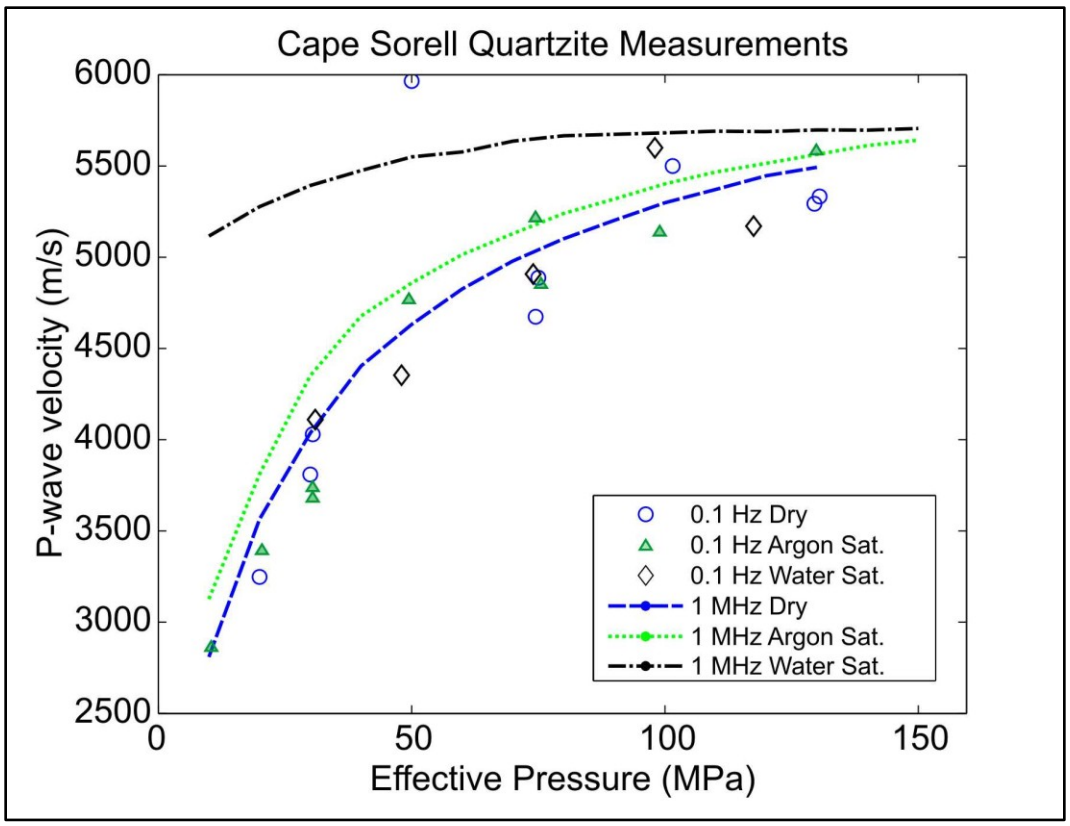

Figure 4.10: Measured high frequency P-wave velocities compared to calculated low frequency velocities for the Cape Sorell quartzite.

Young's and shear moduli at the high frequency limit when the pore fluid is expected to behave as in the saturated isolated regime. Gassmann's (1951) model is the low-frequency limit of the Biot model and is commonly applied to low frequency measurements made under different saturation conditions when sufficient time exists for the pore fluid to equilibrate between cracks as in the saturated isobaric regime.

O'Connell and Budiansky (1977), for highly cracked rocks, estimate the characteristic frequency for the squirt flow between elliptically shaped cracks that separates the saturated-isolated and saturated-isobaric regimes for the self-consistent theory as:

$$f_{OB} = \frac{K_0 \alpha^3}{2\pi\eta} \qquad \text{(2.43 revisited)}$$

where α is the aspect ratio of the cracks, η is the pore fluid viscosity and K_0 is the dry bulk modulus of the rock. When frequencies are $>>f_{OB}$, they fall into the saturated-isolated regime, while frequencies $<< f_{OB}$ fall into the low frequency regime. For both of these quartzites, the characteristic frequency was calculated assuming the aspect ratio is related to the pore throat size measured by mercury porosimetry (0.4 μm and 0.7 μm for the Cape Sorell and Alberta quartzites, respectively) with a pore diameter similar to the grain size visually estimated from thin sections (~0.5 mm for both quartzites). For the Alberta quartzite the calculated characteristic frequency ranged from ~16 kHz for the more viscous water saturation to 170-660 kHz for the argon saturated experimental conditions applied in this study. The characteristic frequency had a broader range for the argon saturated measurements due to argon's strongly pressure dependent viscosity. While low frequency measurements used a varying argon pore pressure, the

high frequency measurements used a constant 10 MPa argon pore pressure due to safety considerations resulting from the different setup for these measurements. The argon saturated high frequency measurements therefore had a more consistent characteristic frequency; 640-660 kHz for the 1 MHz measurements. It was calculated that the Cape Sorell quartzite has cracks with a slightly lower aspect ratio, and the characteristic frequency was estimated to range from 3-140 kHz, depending on the pore fluid properties. For both quartzites the characteristic frequency calculated by the formulation of O'Connell and Budiansky (1977) (as in Equation 2.43) separated the low (0.01-0.78 Hz) frequency measurements into the saturated isobaric fluid flow regime and the high (1 MHz) frequency measurements into the saturated isolated regime. The 1 MHz measurement frequency, however, closely approaches the 660 kHz characteristic frequency estimated for the argon saturated Alberta quartzite, indicating that the argon saturated high frequency measurements may have sampled part of the transition zone between fluid flow regimes.

Biot's (1956a, 1956b) formulations do not assume a particular pore shape, and instead have a reference frequency given by:

$$f_B = \frac{\phi\eta}{2\pi\rho_{fl}\kappa} \qquad \text{(2.41 revisited)}$$

The Biot reference frequency distinguishes at what frequency the effect of inertial coupling between the fluid and matrix becomes more important than viscous coupling. In the case of these measurements the permeabilities of the quartzites are so low that even at the lowest measured effective pressures f_B>>1 GHz. Biot theory reduces to the Gassmann equation at its low frequency limit. Gassmann theory is therefore applicable

at measurement frequencies below the Biot reference frequency, $f<<f_B$, and it is worthwhile to compare both the experimental measurements made between 0.01 – 1 Hz and those made at 1 MHz with the Gassmann prediction.

Meanwhile, the self-consistent theory predicts that, in fact, the 1 MHz measurements fall within the high frequency saturated isolated fluid flow regime, 1 MHz>f_{OB}. As significant dispersion was observed in the water saturated quartzites this seems a likely possibility and implies the 1 MHz measurements can be usefully compared to theoretical models estimating the high frequency limit of the Young's modulus. Here, the measurements were compared to estimations accounting for both Biot and squirt-flow dispersion. Modeling was conducted on the Cape Sorell quartzite as a more comprehensive data set was acquired for the Cape Sorell sample than the Alberta quartzite.

4.5.1 Gassmann

Gassmann's model (1951) predicts the bulk modulus of a fluid saturated rock based on the porosity, bulk modulus of the dry rock, K_{dry}, the mineral, K_0, and the saturating fluid, K_{fl}. A constant shear modulus, μ, is assumed:

$$K_{sat} = K_{dry} + \frac{\left(1 - \frac{K_{dry}}{K_0}\right)^2}{\frac{\phi}{K_{fl}} + \frac{(1-\phi)}{K_0} - \frac{K_{dry}}{K_0^2}}, \qquad \mu_{sat} = \mu_{dry} \qquad \text{(2.27 revisted)}$$

The bulk modulus is related to the Young's modulus through the relation:

$$K_{sat} = \frac{E_{sat}\mu_{sat}}{3(3\mu_{sat} - E_{sat})} \qquad (4.14)$$

The dry bulk moduli of the Cape Sorell quartzite at 1 MHz were calculated using the Young's and shear (see Chapter 2) moduli and substituted into Equation 2.27; porosity was assumed to decrease exponentially with increasing pressure. As measurements at 1 MHz were made on the dry quartzite only up to a confining pressure of 130 MPa due to concerns about leaks it was necessary to estimate dry moduli values at 140 and 150 MPa of pressure. The elastic moduli were in a fairly linear regime after crack closure at ~100 MPa; therefore a line of best fit was applied to the measured shear and Young's modulus from 110-130 MPa to calculate the moduli at 140 and 150 MPa of pressure.

Gassmann theory fails to adequately describe the stiffening effect of either the argon or the water saturated crack porosity on the quartzite at 1 MHz (Fig. 4.11). The Young's modulus result from Gassmann, 26.7±3.5 GPa for water saturation at 10 MPa of effective pressure is 56% smaller than the 1 MHz measured results of 60.5±1.8 GPa, and, at 21.0±9.5 GPa for argon saturation, is 19% smaller than the measured value at 10 MPa, 25.8±4.0 GPa. The Gassmann prediction begins to converge with the measured Young's modulus at pressures ≥130 MPa for the argon saturated quartzite and presumably at pressures >150 MPa for the water saturated quartzite.

The saturated Young's modulus values estimated from Gassmann (1951) were also compared to the quartzite measurements made at frequencies <1 Hz to determine if Gassmann theory was more applicable to these low frequency measurements. Due to the higher variability in the pressure increments at which measurements were taken, a curve was fit to the 0.1 Hz dry shear and Young's moduli measurements of the Cape Sorell quartzite and the fitted values were used to calculate values of K_{dry} for the appropriate effective pressures representative of the 0.1 Hz timescale. These values of

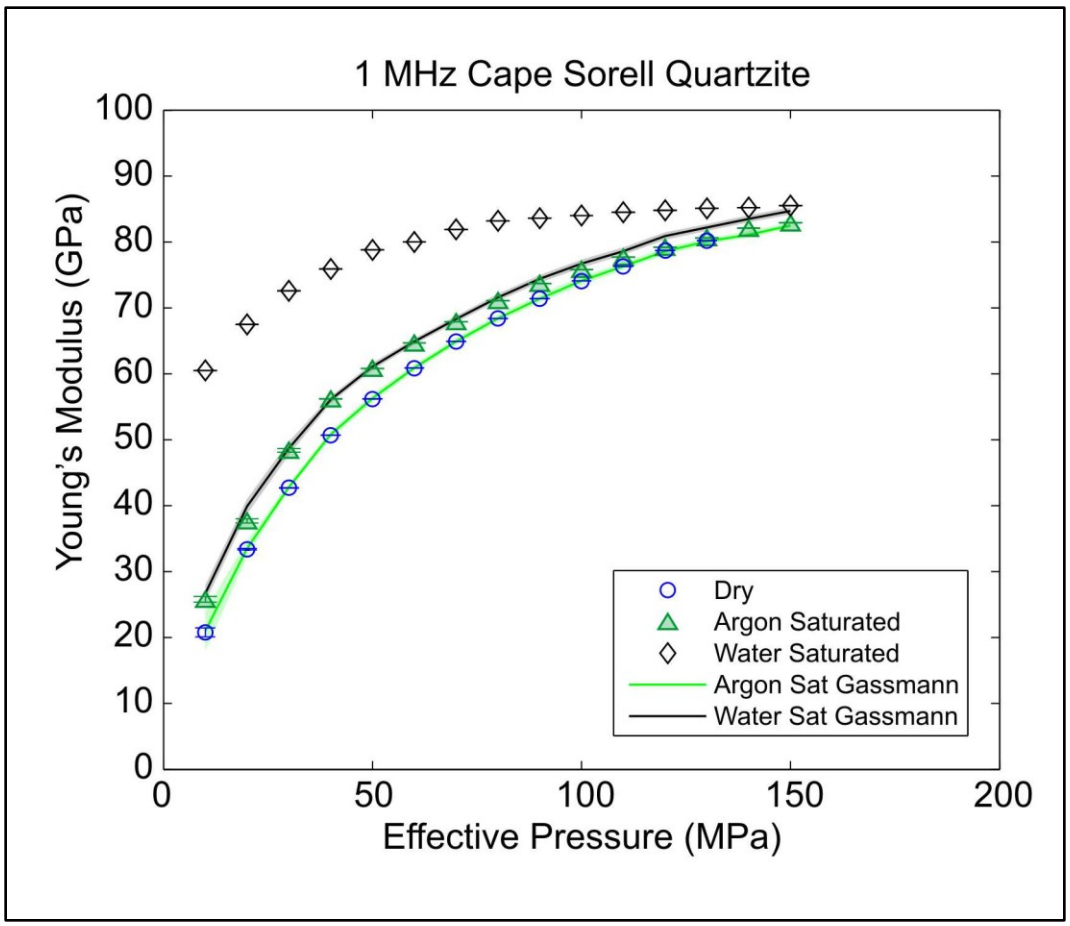

Figure 4.11: Comparison of the Young's modulus of the Cape Sorell quartzite measured at 1 MHz while dry, argon and water saturated with the predictions from Gassmann's (1951) equation. Error bars of measurements in some instances smaller than the marker size; error in theoretical estimate shown as shaded region.

K_{dry} were used as input into Equation 2.27. The Young's moduli estimated from Gassmann's equation were compared to the Young's moduli of the argon and water saturated Cape Sorell quartzite measured at 0.1 Hz (Fig. 4.12). At 0.1 Hz, Gassmann's equation predicts significantly stiffer Young's moduli values than are observed at low effective pressures. The Gassmann prediction for water saturation is 87% higher than the Young's modulus measured at 0.1 Hz and 12 MPa (36.5±1.8 GPa and 19.5±0.6 GPa, respectively) as well as 87% higher than the argon saturated modulus at 10 MPa (predicted to be 30.1±2.1 GPa and measured as 16.1±0.5 GPa). Gassmann equation does not account for the significant additional compliance of the bulk modulus caused by cracks, even at very low porosities. At the low porosity limit, the saturated bulk modulus predicted by Gassmann equation (Eq. 2.27) reduces to the mineral bulk modulus, as opposed to the dry bulk modulus of the rock:

$$\lim_{\phi \to 0}(K_{sat}) = K_{dry} + \frac{\left(1 - \frac{K_{dry}}{K_0}\right)^2}{\frac{1}{K_0} - \frac{K_{dry}}{K_0^2}} = K_0 \qquad (4.15)$$

The treatment of the saturated bulk modulus differs from the treatment of the saturated shear modulus, which is approximated by the dry shear modulus. At the low porosities of the quartzites, the Gassmann prediction is therefore closer to the bulk modulus of quartz, 37.3 GPa at 10 MPa of effective pressure (Liu, 1993) than the calculated bulk modulus of the dry Cape Sorrel quartzite, 2.0±0.7 GPa.

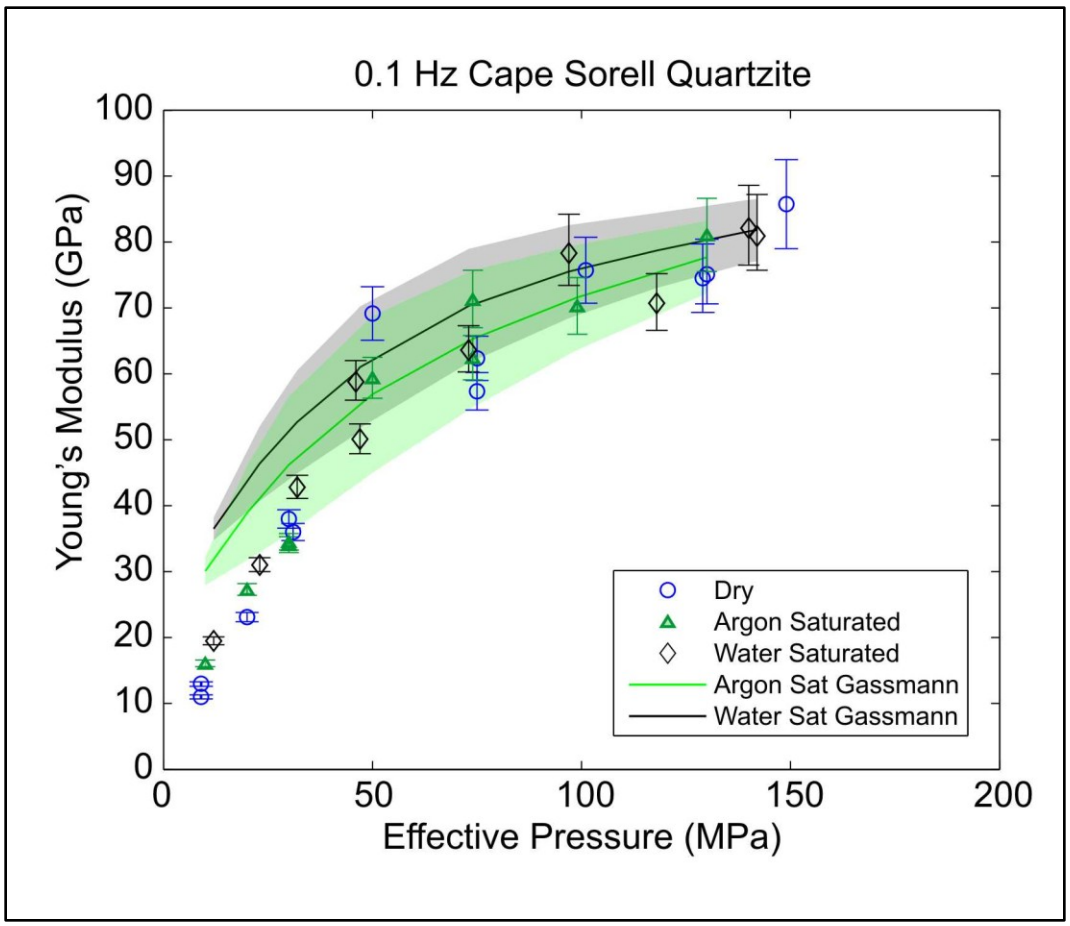

Figure 4.12: Comparison of the Young's modulus of the Cape Sorell quartzite measured at 0. 1 Hz while dry, argon and water saturated with the predictions from Gassmann's (1951) equation. Error in Gassmann estimate shown as shaded region.

Above pressures of 50 MPa the theoretical values predicted by Gassmann and the experimentally measured values begin to converge for both the argon and water saturated measurements as the compliance caused by crack porosity is reduced.

4.5.2 Biot-Squirt Flow

As the Gassmann model (1951) does not adequately predict the stiffening caused by water saturation in the quartzite measurements made at 1 MHz, Biot (1956a, 1956b) theory was combined with squirt-flow theory (Mavko and Jizba, 1991) to investigate whether it is better able to predict the saturated Young's moduli of the quartzites measured at 1 MHz. Effective high frequency, unrelaxed, wet frame bulk and shear moduli, K_{uf} and μ_{uf}, were estimated using squirt flow theory and then substituted into Biot's relations (Eqs. 2.29 – 2.38). The squirt flow moduli were calculated using the formulation of Mavko and Jizba (1991):

$$\frac{1}{K_{uf}} \approx \frac{1}{K_{dry-hiP}} + \phi_{soft}\left(\frac{1}{K_{fl}} - \frac{1}{K_0}\right) \qquad \text{(2.39 revisited)}$$

$$\left(\frac{1}{\mu_{uf}} - \frac{1}{\mu_{dry}}\right) = \frac{4}{15}\left(\frac{1}{K_{uf}} - \frac{1}{K_{dry}}\right) \qquad \text{(2.40 revisited)}$$

where K_{dry} and μ_{dry} are the dry bulk and shear moduli of the rock, $K_{dry\text{-}hiP}$ is the bulk modulus of the dry rock at very high pressure and ϕ_{soft} is the soft porosity which closes at high pressure. The Cape Sorell quartzite had an initial porosity of 0.3% (Lu and Jackson, 1998) which was increased to 2.3% after thermal cracking. Here, ϕ_{soft} at atmospheric pressure was assumed to be the 2.0% of the porosity which had been induced by thermal cracking.

In addition to K_{uf}, μ_{uf} and the physical properties of the saturating fluid, Biot's relations depend on the total porosity, ϕ, and tortuosity, τ, of the rock. Tortuosity was not measured directly during the experiment and it was necessary to calculate it. Flow through the low aspect ratio cracks was approximated as flow between two parallel walls and, using Darcy's law (1856), tortuosity can be related to permeability, κ, crack aperture, c, and porosity (e.g. Mavko *et al.*, 2009):

$$\tau = c\sqrt{\frac{\phi}{12\kappa}} \tag{4.16}$$

As tortuosity is dependent on porosity and permeability in Equation 4.16, both of which are dependent on pressure, the calculated tortuosity was also dependent on pressure. Crack aperture and porosity were measured using mercury porosimetry; porosity was assumed to decrease in an exponential fashion with increasing pressure. This resulted in a tortuosity that varied from τ=69 at 10 MPa up to τ=152 at 150 MPa of effective pressure for the Cape Sorell quartzite. In practice, the tortuosity had little effect on the theoretical predictions in this case. The porosity of the sample (2.3%) is low enough that, as the tortuosity appears in Biot's relation only in multiplication with the porosity, it has negligible effect on the results.

Biot-squirt flow theory provides an excellent estimation of the stiffening effect of argon on the shear modulus of the Cape Sorell quartzite at 1 MHz. At 10 MPa of effective pressure, Biot-squirt flow predicts an argon saturated shear modulus of 13±3 GPa, while the argon saturated shear modulus, within error of the prediction, was measured to be 12.3±0.4 GPa. The Young's modulus prediction, of 35±1 GPa at 10 MPa

of effective pressure is30% different from the measured argon saturated modulus of 25.8±0.4 GPa.

Biot-squirt flow theory, however, fails by a substantial margin to predict the increase in elastic stiffness that was measured when the quartzite was water saturated (Figs. 4.13, 4.14). The theoretical predictions do not agree with the experimentally observed values until pressures above 130 MPa. The velocity dispersion predictions of the theory are largely dominated by squirt-flow effects. As the total porosity and assumed soft porosity of the sample are small, effects of fluid compressibility are negligible to the squirt-flow predictions in this case (Eq. 2.39), leading to similar predictions for both argon and water saturated conditions. At 10 MPa of effective pressure, Biot-squirt flow predicts a water saturated shear modulus of 13±3 GPa, similar to the prediction for argon saturation. The experimentally measured results differ substantially under the different saturation conditions, however, and the water saturated shear modulus was measured to be 24.7±0.1 GPa, well outside the range of error in the Biot-squirt flow estimate. Biot-squirt flow also underpredicts the water saturated Young's modulus. Biot-squirt flow predicts a Young's modulus of 35±1 GPa at 10 MPa of effective pressure for the water saturated quartzite, while measured results were substantially higher, at 60.5±0.1 GPa.

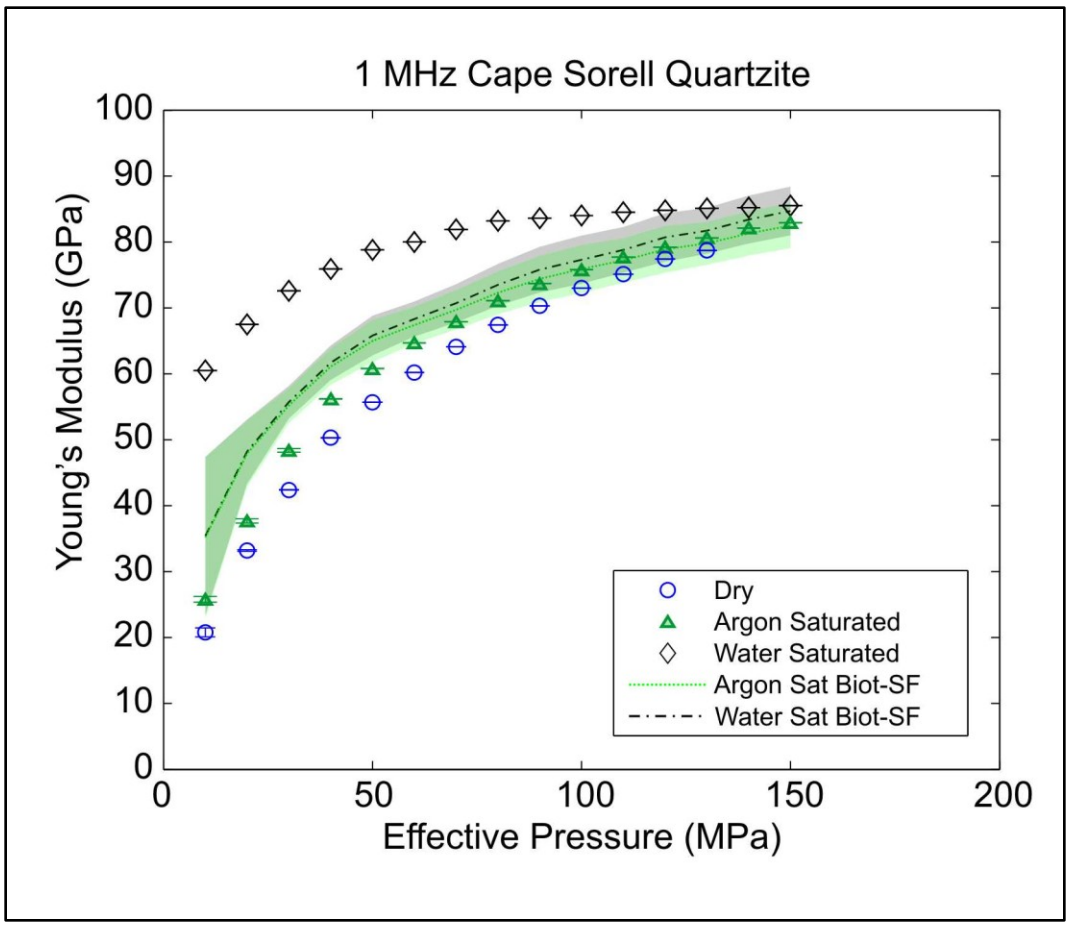

Figure 4.13: Comparison of the Young's modulus of the Cape Sorell quartzite measured at 1 MHz while dry, argon and water saturated with the predictions from Biot-Squirt Flow theory. Error bars of measurements in some instances smaller than the marker size; error in theoretical estimate shown as shaded region.

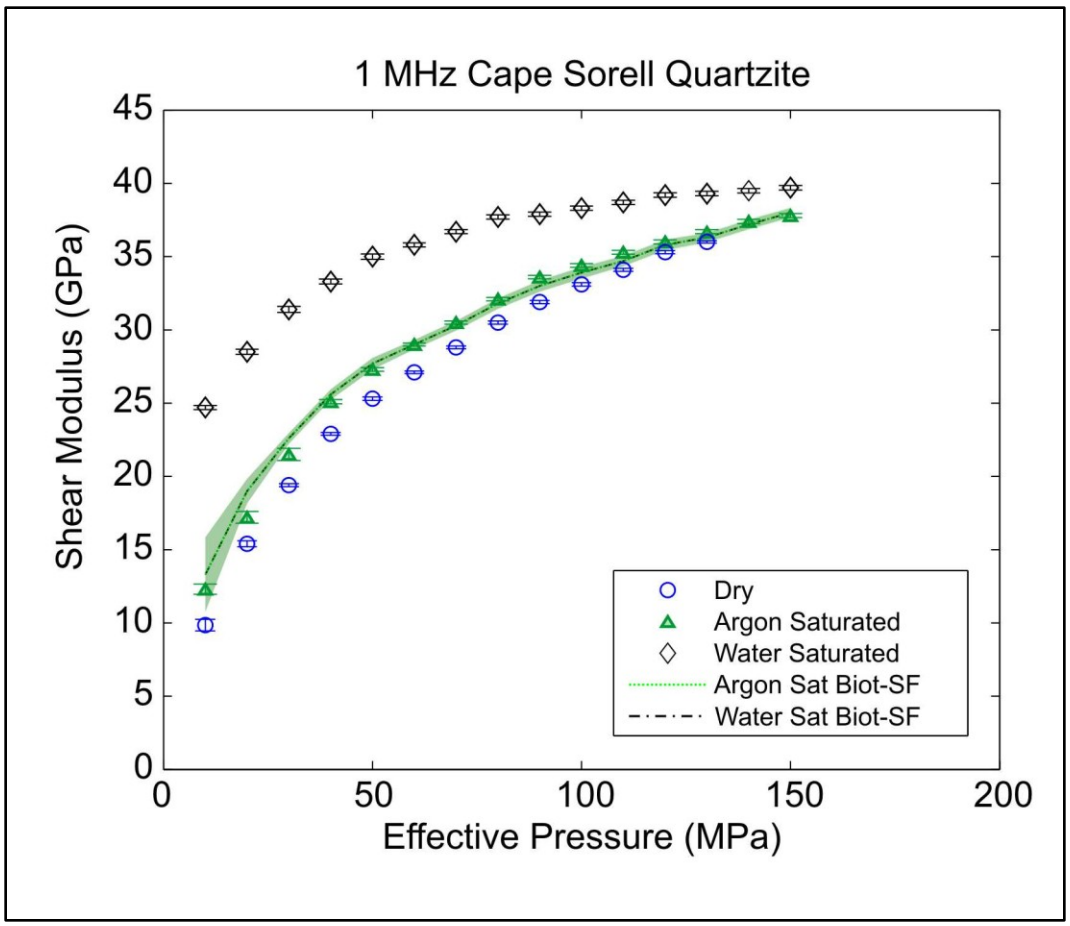

Figure 4.14: Comparison of the shear modulus of the Cape Sorell quartzite measured at 1 MHz while dry, argon and water saturated with the predictions from Biot-Squirt Flow theory. Error bars of measurements in some instances smaller than the marker size; error in theoretical estimate shown as shaded region.

4.6 Discussion

Strong Young's modulus dispersion is definitively observed in the water saturated Cape Sorell quartzite, with a similar magnitude of dispersion expected in the Alberta quartzite from its measured high frequency water saturated modulus and low frequency dry modulus. The substantial stiffening of the Young's modulus at high frequencies indicates that the quartzite must have been in a higher frequency fluid flow regime at 1 MHz than at measurements <1 Hz. Likely, the quartzites are in the saturated isolated regime at 1 MHz. The Cape Sorell quartzite measurements between 0.01 and 1 Hz show some slight ongoing stiffening of the Young's modulus, as might be expected during a fluid flow regime transition. The dispersion is highest at lower effective pressures when cracks are open. The cause of this is not completely clear; it may be that the characteristic frequency separating the isolated saturated and isolated isobaric is lower than anticipated and the stiffening is resulting from nearing a saturated isolated fluid flow regime. Alternatively, this may result from boundary effects at the surface of the cylinder (Dunn, 1986, Dunn, 1987).

The theoretical models tested fail to adequately estimate the stiffening effect of water saturation at high frequency for both quartzites. While Gassmann, Biot and squirt-flow theory do not explicitly depend on pore shape, they appear to perform poorly for low aspect ratio crack porosity. This highlights the need to determine a suitable theoretical model capable of accurately estimating dispersion in the cracked crystalline crust.

At low frequencies, Gassmann overestimates the stiffening caused by water saturation, predicting a Young's modulus of 37±2 GPa at 12 MPa of effective pressure

for the Cape Sorell quartzite, while a modulus of only 19.5±0.6 GPa was measured at 0.1 Hz. The low frequency estimation has a stiffer Young's modulus than the high frequency estimation at low effective pressures here (27±1 GPa at 10 MPa of pressure), as a result of differences in the moduli measured at low and high frequency. The 1 MHz dry shear modulus was previously measured to be significantly lower than the 0.1 Hz shear modulus, 9.9 GPa and 13.1 GPa respectively (Chapter 3), impacting the Gassmann prediction. The difference in shear modulus measurements may result from error in picking the high frequency shear-wave arrival time at the lower signal to noise ratios present at low effective pressures during ultrasonic pulse transmission (Fig. 3.6). An erroneously low shear modulus would result in an increase in the Young's modulus calculated from the 1 MHz P- and S-wave velocities. Indeed, the high frequency dry Young's modulus was measured to be higher than the 0.1 Hz Young's modulus, 20.8±0.7 GPa and 12±3 GPa, respectively. Nonetheless, both Gassmann estimations overestimate the stiffening effect of water at low frequencies. There are several possible reasons for this. Global fluid flow (e.g. Dunn, 1986, Dunn, 1987) between the side of the specimen in extension and the side simultaneously in compression during the low frequency flexural oscillation may provide some of the answer. Alternatively, the transition between fluid flow regimes indicated by the increasing Young's modulus measurements between 0.01 and 1 Hz may be indicative of a transition between the drained regime and the saturated isobaric regime, as opposed to between the saturated isobaric and saturated isolated, as indicated by the self-consistent theory. Permeability measurements indicate it is unlikely that the water could flow completely out of the sample on the timescale of measurement, however, and this is considered unlikely. Finally, it is possible that Gassmann, while a robust model at higher porosities with more

equant pores, performs poorly for low porosity cracked crystalline rock. While the compliance introduced by spherical pores is proportional to the porosity, crack induced compliance is instead proportional to the rate of change of porosity (Walsh, 1965a). As a result, the Gassmann prediction that at low porosity the saturated bulk modulus tends towards the bulk modulus of the mineral as opposed to towards the measured dry bulk modulus of the rock may not be correct for low porosity rocks with low aspect ratio cracks.

It is evident in the 1 MHz measurements that both the argon saturated Cape Sorell and Alberta quartzites have stiffer Young's moduli than when dry. For the Alberta quartzite this is true only at effective pressures <80 MPa. As the dry measurements were undertaken first, it appears this may be the result of some additional cracking induced during the initial pressurization run. Porosity measurement of the Alberta sample was made exclusively using mercury porosimetry, a destructive technique, and it was therefore only possible to measure the porosity after the completion of all measurements. The amplitude of the stiffening seen at high frequency is low, and with the higher error in the low frequency measurements it is not clear if the low frequency measurements see a similar stiffening with argon pore fluid or not. Potential observations of dispersion are further complicated by the different mechanisms of measurement at low and high frequencies. At low effective pressures high frequency measurements were made with argon at a low pore pressure (10 MPa) for safety reasons while low frequency measurements were made with argon at a high pore pressure (137, 127 and 117 MPa for effective pressures 10, 20 30 MPa, respectively) as these were logistically simpler for the low frequency apparatus. At high frequencies, the

pore fluid therefore had a bulk modulus of 0.01 GPa, while at low frequencies, the bulk modulus of the pore fluid was as high as 0.04 GPa (NIST, 2012). The amount of stiffening caused by argon at <1 Hz is similar to at 1 MHz; at 20 MPa the Young's modulus stiffens by 4.2±1.6 GPa and 4.5±0.6 GPa, respectively. It is possible that the higher bulk modulus of the saturating argon at low frequencies is helping to mask any subtle dispersion response, if it exists.

No dispersion is observed in the dry quartzites, with excellent agreement evident across the measured frequencies of the Alberta quartzite in particular. A small discrepancy is observed between the <1 Hz and 1 MHz measurements of the Cape Sorell quartzite at effective pressures <75 MPa. This could have several possible explanations. Potentially, this could indicate that the interfacial effects and compliance of the polycrystalline alumina rods have been slightly underestimated in the low frequency measurements by the fit of the fused quartz normalized modulus data. The fused quartz data (Fig. 4.2) appears to imply these aspects of the rod have a strong pressure dependence at effective pressures <75 MPa, but few fused quartz data have been acquired to constrain them at these lower pressures. As noted above, however, the Alberta quartzite shows excellent agreement between the low and high frequency measurements from 10-30 MPa, rendering this an unlikely culprit. A comparison of the measured high frequency P-wave velocities with calculated low frequency P-wave velocities for the Cape Sorell quartzite shows good agreement, even at low effective pressures (Fig. 4.10). This implies that the discrepancy in the low effective pressure Young's modulus measurements likely results from low signal-to-noise levels in the high

frequency shear wave travel time picks required to calculate the high frequency Young's modulus.

4.7 Conclusions

The ANU apparatus successfully measures the dry and argon saturated Young's moduli of the dry Alberta and Cape Sorell quartzites and argon saturated Cape Sorell quartzite at frequencies 0.01 – 1 Hz using forced flexural oscillation. The apparatus successfully measures the Young's modulus of the water saturated Cape Sorell quartzite as well, but requires an empirical correction in the numerical modelling. The empirical correction required is potentially related to the behaviour of the polycrystalline alumina rods which form part of the apparatus and sandwiched the quartzite specimens during measurement. The rods have undergone repeated pressure and temperature cycling during their history. Cracks may have been induced in the rods as a result, which caused the change in observed behaviour of the apparatus during water saturation. Alternatively, the effect may be caused by water-induced changes in the frictional coefficients of the interfacially coupled components of the apparatus. Confirmation of the cause of the differing behaviour of the apparatus during water saturation requires further work in order to allow it to be analytically incorporated into the modelling. In all cases, the apparatus is less sensitive to Young's moduli of stiffer specimen and therefore loses sensitivity here at higher effective pressures as the samples undergo progressive crack closure. Future work may explore an alternative mode of flexural oscillation excited by an oscillating bending force rather than a bending moment with the lower end of the cantilevered beam only weakly propped. Instead of flexure being induced by

two electromagnetic drivers working in opposition parallel to the beam, bending could be achieved by the electromagnetic drivers working together to exert force in a direction perpendicular to the beam. This change in experimental setup would reduce the setup time required for each experiment. Significant changes to the amplitude of the experimentally measured normalized modulus could be achieved by changing the lower boundary condition of the experimental assembly which could potentially result in higher signal to noise in the flexural measurements.

High (1 MHz) and low (0.01-1 Hz) frequency Young's modulus measurements were compared for both the Alberta and Cape Sorell quartzites. As expected, no dispersion was observed while the quartzites are dry. Some disagreement between the low and high frequency results is observed, but this is likely caused by difficulty in picking ultrasonic shear wave traveltimes. No dispersion in the Young's modulus can be confidently identified during argon saturation of the Cape Sorell quartzite, although both quartzites show a stiffening of up to ~20% of their Young's moduli at high frequency when saturated. The water saturated Cape Sorell quartzite shows substantial dispersion, with the high frequency Young's modulus at 10 MPa of effective pressure more than three times larger than the low frequency modulus at 12 MPa of effective pressure (103% different). Although the Alberta quartzite was not measured at low frequencies while water saturated, similar dispersion is expected. The high frequency modulus of the Alberta quartzite increases significantly under water saturation conditions, from 25.3 GPa when measured dry to 55.2 GPa when saturated.

Due to the extremely low permeability of the samples the measurements undertaken at 1 MHz fall below the Biot reference frequency which theoretically

differentiates between the low and high frequency measurement regimes, however, both Gassmann and Biot-squirt flow fail to account for the full magnitude of the dispersion observed in the water saturated Cape Sorell quartzite. Gassmann theory underestimates the 1 MHz saturated measurements, with Gassmann predictions for the water saturated quartzite as much as 56% lower than the measured Young's modulus, and as much as 19% lower than the measured Young's modulus of the argon saturated quartzite. Despite the 1 MHz measurements falling below the Biot reference frequency, Biot-squirt flow theory performs better. The theory successfully predicts the 1 MHz argon saturated shear modulus. The 1 MHz argon saturated Young's modulus, however, is overestimated by the theory, with Biot-squirt flow predicting a Young's modulus that is 36% higher than the measured argon saturated Young's modulus. The theory fails to predict the effects of water saturation, significantly underestimating the 1 MHz moduli. The Biot-squirt flow Young's and shear moduli are, respectively, as much as 42% and 47% lower than the measured water saturated moduli. Both Gassmann and Biot-squirt flow give poor predictions of the dispersion of this sample, likely as a result of its very low porosity in conjunction with its very low aspect ratio cracks.

Although the mineralogy and crack distribution of the quartzites is relatively simple in terms of experimental samples, the physical properties of the quartzites are quite complex when compared to theoretical expectations with complicated crack shapes and the associated complications of fluid flow between cracks.

Table 4.1: Fused quartz normalized flexural modulus

Effective Pressure (MPa)	Argon Pore Pressure (MPa)	Run No.	.087 Hz	0.010 Hz	0.021 Hz	0.046 Hz	0.156 Hz	0.260 Hz	0.781 Hz
28	72	1206	0.29649	0.29654	0.29642	0.29633	0.29647	0.29655	0.2967
30	*	1206	0.29637	0.29668	0.29658	0.29649	0.29638	0.29629	0.29645
61	40	1206	0.29782	0.29775	0.29777	0.29768	0.2979	0.29792	0.29793
62	*	1206	0.29796	0.29812	0.29794	0.29807	0.2981	0.29802	0.29817
102	*	1206	0.29801	0.29828	0.29824	0.29816	0.29799	0.29824	0.29834
103	*	1208	0.29907	0.29909	0.29924	0.29915	0.29924	0.2992	0.29922
104	*	1206	0.29853	0.29841	0.29844	0.2985	0.29856	0.29868	0.29883
125	*	1208	0.30125	0.30094	0.30105	0.30133	0.30116	0.30114	0.30132
126	*	1206	0.29902	0.2991	0.299	0.29908	0.29912	0.29913	0.29912
150	*	1206	0.29866	0.29887	0.29879	0.29872	0.29879	0.29875	0.29906
172	*	1206	0.29879	0.29894	0.29886	0.29875	0.29876	0.29876	0.29956
189	*	1206	0.29939	0.29943	0.29954	0.2993	0.29946	0.29922	0.2994

Table 4.1: Normalized modulus measurements of fused quartz at varying effective pressures. During run 1206 the fused quartz was inserted directly into the copper jacket; during run 1208 the quartz was wrapped in Teflon tape prior to insertion into the copper jacket.

Table 4.2: Dry Cape Sorell quartzite Young's modulus

Frequency

Pressure (GPa)	9.9 mHz (up)	9.9 mHz (down)	0.021 Hz (up)	0.021 Hz (down)	0.046 Hz (up)	0.046 Hz (down)	0.087 Hz (up)	0.087 Hz (down)	0.16 Hz (up)	0.16 Hz (down)	0.26 Hz (up)	0.26 Hz (down)	0.78 Hz (up)	0.78 Hz (down)	1 MHz (up)	1 MHz (down)
9/9/10	11	11.2	11	11.7	11	12.2	11	13	11.1	13.7	11.1	14.6	11.1	15.5	20.76	*
20	22.2	*	22.3	*	22.8	*	23.1	*	23.4	*	23.8	*	23	*	33.23	*
30/31/30	36.4	*	36.7	35.1	37.9	*	38	35.9	39	*	40.4	37.2	39.1	37.7	42.39	*
40	*	*	*	*	*	*	*	*	*	*	*	*	*	*	50.31	*
50	65.3	*	66.1	*	66.3	*	69	*	70.4	*	72.7	*	69.3	*	55.68	*
60	25.229	*	25.238	*	25.203	*	25.424	*	25.334	*	25.491	*	25.512	*	60.21	*
70	*	*	*	*	*	*	*	*	*	*	*	*	*	*	64.07	*
75	58.8	59.9	59.5	61.9	60.8	62	57.2	62.2	59.8	65.1	61.7	67.1	58.1	66.5	*	*
80	*	*	*	*	*	*	*	*	*	*	*	*	*	*	67.44	*
90	*	*	*	*	*	*	*	*	*	*	*	*	*	*	70.34	*
101/*/100	71.9	*	72.5	*	74.4	*	75.4	*	77.5	*	80.4	*	77.3	*	72.97	*
110	*	*	*	*	*	*	*	*	*	*	*	*	*	*	75.05	*
120	*	*	*	*	*	*	*	*	*	*	*	*	*	*	77.35	*
129/130/130	109.1	*	91	76.5	79.2	*	74	75.2	73.8	*	77.1	75.4	72.5	72.7	78.75	*
140	*	*	*	*	*	*	*	*	*	*	*	*	*	*	*	*
149/*/150	182.3	*	101.2	*	90	*	85.1	*	85.4	*	85.6	*	85.6	*	*	*

* Where multiple pressures are shown, the first indicates the low frequency pressure during loading (up), the second the low frequency pressure during unloading (down) and the third the high frequency pressure during both loading and unloading measurements, where applicable.

Table 4.3: Argon saturated Cape Sorell quartzite Young's modulus

Effective Pressure (GPa)	Frequency															
	9.9 mHz (up)	9.9 mHz (down)	0.021 Hz (up)	0.021 Hz (down)	0.046 Hz (up)	0.046 Hz (down)	0.087 Hz (up)	0.087 Hz (down)	0.16 Hz (up)	0.16 Hz (down)	0.26 Hz (up)	0.26 Hz (down)	0.78 Hz (up)	0.78 Hz (down)	1 MHz (up)	1 MHz (down)
10	*	15.5	*	15.5	*	15.9	*	16.1	*	16.4	*	16.7	*	16.1	25.76	*
20	*	27.9	*	27	*	27.1	*	27.3	*	27.9	*	28.6	*	28	37.68	*
30	33	34.4	33	33.9	33.5	34.5	34.1	34.5	34.7	35.3	35.3	36.1	34.5	35.1	48.40	*
40	*	*	*	*	*	*	*	*	*	*	*	*	*	*	56.19	*
50	*	58.7	*	57.5	*	58.4	*	59.3	*	60.1	*	63.8	*	61.5	60.81	*
60	*	*	*	*	*	*	*	*	*	*	*	*	*	*	64.73	*
70	*	*	*	*	*	*	*	*	*	*	*	*	*	*	67.90	*
74	*	72.6	61.8	67.9	*	69.5	62.3	71.1	*	73	63.2	76.6	61.4	73.2	71.10	*
80	*	*	*	*	*	*	*	*	*	*	*	*	*	*	73.68	*
90	*	*	*	*	*	*	*	*	*	*	*	*	*	*	75.85	*
*/99/100	*	79.9	*	73.3	*	68.4	*	70	*	74.5	*	75.2	*	67.4	77.68	*
110	*	*	*	*	*	*	*	*	*	*	*	*	*	*	79.15	*
120	*	*	*	*	*	*	*	*	*	*	*	*	*	*	80.60	*
130	*	325.2	81.2	180	*	144	80.7	147.8	*	124.5	81.6	127.8	80.1	113.8	82.08	*
140	*	*	*	*	*	*	*	*	*	*	*	*	*	*	82.93	*
150	*	*	*	*	*	*	*	*	*	*	*	*	*	*	25.76	*

Table 4.4: Water saturated Cape Sorell quartzite Young's modulus

Effective Pressure (GPa)	Frequency																		
	1 mHz (up)	2.1 mHz (up)	4.7 mHz (up)	9.9 mHz (up)	9.9 mHz (down)	0.021 Hz (up)	0.021 Hz (down)	0.046 Hz (up)	0.046 Hz (down)	0.087 Hz (up)	0.087 Hz (down)	0.16 Hz (up)	0.16 Hz (down)	0.26 Hz (up)	0.26 Hz (down)	0.78 Hz (up)	0.78 Hz (down)	1 MHz (up)	1 MHz (down)
*/12/10	*	*	*	*	17.8	*	18.7	*	19.3	*	19.5	*	20.2	*	21.1	*	23.9	60.47	63.76
23/*/20	26.6	28.1	28.7	28.3	*	28.8	*	30.6	*	31	*	31.2	*	31.7	*	31.4	*	67.51	70.59
*/32/30	*	*	*	*	4.04	*	41.1	*	41.4	*	42.8	*	43.8	*	45.5	*	49.7	72.59	74.92
40	*	*	*	*	*	*	*	*	*	*	*	*	*	*	*	*	*	75.93	77.80
47/46/50	*	*	*	48.1	*	49.8	57.3	50.4	*	50.1	58.8	47.8	*	49.3	57.9	52.8	57.4	78.77	80.23
60	*	*	*	*	*	*	*	*	*	*	*	*	*	*	*	*	*	80.00	81.55
73/*/70	*	*	*	60.4	*	61.2	*	60.1	*	63.6	*	66.9	*	66.9	*	72.3	*	81.87	82.85
80	*	*	*	*	*	*	*	*	*	*	*	*	*	*	*	*	*	83.22	83.98
90	*	*	*	*	*	*	*	*	*	*	*	*	*	*	*	*	*	83.59	84.71
97/*/100	*	*	*	75.1	*	75.9	*	78.5	*	78.3	*	81.7	*	85.8	*	86.6	*	84.04	85.23
110	*	*	*	*	*	*	*	*	*	*	*	*	*	*	*	*	*	84.49	85.61
118/*/120	*	*	*	67.1	*	68.8	*	71.1	*	70.7	*	70.8	*	71	*	69.9	*	84.85	85.48
130	*	*	*	*	*	*	*	*	*	*	*	*	*	*	*	*	*	85.10	85.80
142/140/140	*	*	*	78.6	81.6	79.6	85.4	81.1	76.5	80.9	82.1	84.3	82.1	81.8	81.6	88.2	84.6	85.19	85.60
150	*	*	*	*	*	*	*	*	*	*	*	*	*	*	*	*	*	85.52	*

Table 4.5: Dry Alberta Quartzite Young's modulus

Frequency

Pressure (GPa)	9.9 mHz (up)	9.9 mHz (down)	0.021 Hz (up)	0.021 Hz (down)	0.046 Hz (up)	0.046 Hz (down)	0.087 Hz (up)	0.087 Hz (down)	0.16 Hz (up)	0.16 Hz (down)	0.26 Hz (up)	0.26 Hz (down)	0.78 Hz (up)	0.78 Hz (down)	1 MHz (up)	1 MHz (down)
10/*/10	26.6	*	27.2	*	26.9	*	26.7	*	26.5	*	26.5	*	27.5	*	25.30	*
21/*/20	40.9	*	40.8	*	39.9	*	39.6	*	39.6	*	39.5	*	39.8	*	35.07	44.57
30	45.6	*	45.6	*	44.9	*	44.8	*	44.7	*	44.8	*	45.2	*	43.07	51.77
40	*	*	*	*	*	*	*	*	*	*	*	*	*	*	50.24	56.29
50/*/50	54.4	*	54.8	*	54.4	*	55.1	*	55.4	*	55.6	*	55.7	*	54.60	60.93
60	*	*	*	*	*	*	*	*	*	*	*	*	*	*	58.86	65.69
70	*	*	*	*	*	*	*	*	*	*	*	*	*	*	62.84	68.22
75	64.9	*	65.2	*	65.2	*	65.8	*	66.2	*	65.9	*	65.3	*	*	*
80	*	*	*	*	*	*	*	*	*	*	*	*	*	*	66.23	70.81
90	*	*	*	*	*	*	*	*	*	*	*	*	*	*	68.75	72.33
100	*	*	*	*	*	*	*	*	*	*	*	*	*	*	71.35	73.83
110	*	*	*	*	*	*	*	*	*	*	*	*	*	*	73.16	74.96
120	*	*	*	*	*	*	*	*	*	*	*	*	*	*	74.51	75.89
130	*	*	*	*	*	*	*	*	*	*	*	*	*	*	76.04	76.92
140	*	*	*	*	*	*	*	*	*	*	*	*	*	*	77.05	77.37
150	*	*	*	*	*	*	*	*	*	*	*	*	*	*	78.11	*

Table 4.6: Argon saturated Alberta Quartzite Young's modulus

Frequency

Effective Presssure (GPa)	9.9 mHz (up)	9.9 mHz (down)	0.021 Hz (up)	0.021 Hz (down)	0.046 Hz (up)	0.046 Hz (down)	0.087 Hz (up)	0.087 Hz (down)	0.16 Hz (up)	0.16 Hz (down)	0.26 Hz (up)	0.26 Hz (down)	0.78 Hz (up)	0.78 Hz (down)	1 MHz (up)	1 MHz (down)
10/*/10	*	*	*	*	*	*	*	*	*	*	*	*	*	*	28.46	32.50
21/*/20	*	*	*	*	*	*	*	*	*	*	*	*	*	*	37.64	45.25
30	*	*	*	*	*	*	*	*	*	*	*	*	*	*	45.36	52.16
40	*	*	*	*	*	*	*	*	*	*	*	*	*	*	52.51	56.76
50/*/50	*	*	*	*	*	*	*	*	*	*	*	*	*	*	56.42	59.67
60	*	*	*	*	*	*	*	*	*	*	*	*	*	*	59.51	61.26
70	*	*	*	*	*	*	*	*	*	*	*	*	*	*	62.54	65.70
75	*	*	*	*	*	*	*	*	*	*	*	*	*	*	*	*
80	*	*	*	*	*	*	*	*	*	*	*	*	*	*	65.02	67.92
90	*	*	*	*	*	*	*	*	*	*	*	*	*	*	67.35	69.65
100	*	*	*	*	*	*	*	*	*	*	*	*	*	*	69.16	71.13
110	*	*	*	*	*	*	*	*	*	*	*	*	*	*	70.93	72.71
120	*	*	*	*	*	*	*	*	*	*	*	*	*	*	72.60	74.01
130	*	*	*	*	*	*	*	*	*	*	*	*	*	*	74.13	75.20
140	*	*	*	*	*	*	*	*	*	*	*	*	*	*	75.26	75.84
150	*	*	*	*	*	*	*	*	*	*	*	*	*	*	76.41	*

Table 4.7: Water saturated Alberta Quartzite Young's modulus

Frequency

Effective Presssure (GPa)	9.9 mHz (up)	9.9 mHz (down)	0.021 Hz (up)	0.021 Hz (down)	0.046 Hz (up)	0.046 Hz (down)	0.087 Hz (up)	0.087 Hz (down)	0.16 Hz (up)	0.16 Hz (down)	0.26 Hz (up)	0.26 Hz (down)	0.78 Hz (up)	0.78 Hz (down)	1 MHz (up)	1 MHz (down)
10	*	*	*	*	*	*	*	*	*	*	*	*	*	*	55.23	60.26
20	*	*	*	*	*	*	*	*	*	*	*	*	*	*	59.75	70.47
30	*	*	*	*	*	*	*	*	*	*	*	*	*	*	65.11	41.35
40	*	*	*	*	*	*	*	*	*	*	*	*	*	*	68.43	72.44
50	*	*	*	*	*	*	*	*	*	*	*	*	*	*	69.91	75.01
60	*	*	*	*	*	*	*	*	*	*	*	*	*	*	72.34	75.01
70	*	*	*	*	*	*	*	*	*	*	*	*	*	*	73.56	77.37
80	*	*	*	*	*	*	*	*	*	*	*	*	*	*	75.18	78.71
90	*	*	*	*	*	*	*	*	*	*	*	*	*	*	76.42	78.74
100	*	*	*	*	*	*	*	*	*	*	*	*	*	*	77.35	79.26
110	*	*	*	*	*	*	*	*	*	*	*	*	*	*	78.33	79.91
120	*	*	*	*	*	*	*	*	*	*	*	*	*	*	79.39	80.41
130	*	*	*	*	*	*	*	*	*	*	*	*	*	*	80.30	80.87
140	*	*	*	*	*	*	*	*	*	*	*	*	*	*	80.52	81.01
150	*	*	*	*	*	*	*	*	*	*	*	*	*	*	81.00	*

5.0 Conclusions

Seismic velocity is used to process seismic refraction and seismic reflection data. The quality of the velocity information is often directly linked to the quality of the processed survey images (e.g. Heinonen *et al.*, 2013, Schijns *et al.*, 2009b). There are numerous ways to measure seismic velocity including in-situ methods such as velocities from refracted waves, semblance methods and vertical seismic profiles. In-situ data can, however, be costly and logistically difficult to acquire. It is often necessary, or preferred, to model the seismic response of a survey area prior to collecting any in-situ data in order to optimize survey design. For these reasons, it is beneficial and certainly more cost effective to acquire laboratory measurements of seismic velocities. Laboratory measurements, however, are typically made in the megahertz frequency range, while active source seismic is typically measured on the order of 10-300 Hz and passive seismic at even lower frequencies, typically in the millihertz range. Fluid in pores and cracks in rocks affect the bulk elastic properties of the rock. The fluid takes a finite amount of time to flow between pore spaces, with the result that pore pressure is dependent on the period of the seismic wave inducing the stress. As seismic velocities are directly correlated with elastic stiffness, these fluid-filled inclusions result in frequency dependent seismic velocities, or velocity dispersion. Fluid filled low aspect ratio cracks can have a particularly strong dispersion effect on velocities due to the high compliance of the cracks when they are relaxed. It is necessary to determine how well current theoretical models predict the dispersion caused by fluid in cracks in order to increase our ability to accurately compare in-situ and laboratory results.

5.1 Summary

This thesis presents elastic moduli results acquired over a range of frequencies on two quartzite specimens. The majority of the Earth's crust is anticipated to be composed of crystalline rock with fluid-filled cracks (Crampin and Lovell, 1991), and these cracked natural crystalline rock specimens are considered representative of potential crustal lithology. Shear and Young's modulus measurements were made from 0.01-1 Hz and at 1 MHz under dry, argon saturated and water saturated conditions.

The two quartzites were thermally shocked in order to induce low aspect ratio cracks. The quartzites were well characterized, with density, permeability and porosity measured. Mercury porosimetry was used to give information on the distribution of the crack population in terms of size. Further, the mineralogy and cracks of the quartzites were well imaged with light microscope and SEM.

Low frequency measurements are difficult to make in the laboratory; here, low frequency shear modulus measurements were made using the well established forced torsional oscillation method using the ANU (Australia National University) apparatus (Jackson *et al.*, 1984, Jackson and Paterson, 1993), while Young's modulus measurements were made by innovatively adapting the ANU apparatus to make forced flexural measurements (Jackson *et al.*, 2011). This thesis presents the calibration process and analysis method and the first experimental results from the forced flexural measurement technique, as well as the first water saturated results from the apparatus. Previously, low frequency flexural measurements had been made on experimental specimens composed of fused quartz and copper with known moduli by Jackson *et al.* (2011). Here, a finite difference model was used to determine the elastic stiffness of

polycrystalline alumina (Duramic) rods which formed an important component of the overall specimen assembly, as they were hollow and allowed pore fluid to be delivered to the sample. The finite difference model was then used in conjunction with the experimentally determined stiffness of the alumina rods to calculate the Young's moduli of the two quartzite specimens under varying effective pressures. A further calibration of the rods was required for the water saturated quartzites.

High frequency measurements of P- and S-wave velocities were made using ultrasonic pulse transmission. Shear and Young's moduli were calculated from the high frequency velocities and densities of the samples and used in conjunction with the low frequency measurements to characterize the velocity dispersion in the samples. The experimental measurements were compared to several theoretical formulations, with aspects compared to Gassmann (1951), Biot-Squirt flow (Biot, 1956, Mavko and Jizba, 1991), Hudson theory (Hudson, 1981) and the self-consistent theory (O'Connell and Budiansky, 1977).

5.2 Discussion

This research took advantage of the innovative adaptation to the ANU apparatus which allowed flexural forced oscillation low frequency measurements to study dispersion of the elastic stiffness. The flexural method successfully measured the Young's moduli of the two quartzites at frequencies ≤1 Hz. A slight pressure dependence of the experimental results on fused quartz using the apparatus was expected to result from interfacial effects between frictionally coupled components of

the apparatus. These effects were accounted for by allowing slight variation in the Young's modulus of the apparatus' polycrystalline alumina rods within the finite difference model used to calculate the Young's modulus of the specimen. Water saturation similarly affected the experimental measurements. The mechanism of this is not completely clear, but it is hypothesized that the stiffer moduli observed result from small cracks induced in the polycrystalline alumina rods during historic repeated pressure and temperature cycling. Allowing further variation in the elastic stiffness of the rods during the modeling accounts for this variation and allowed low frequency water saturated Young's modulus measurements.

During both low and high frequency measurements, the shear and Young's moduli of the quartzites were observed to be strongly pressure dependent. The moduli stiffened substantially as a result of crack closure as effective pressure was increased. The pressure at which the majority of the cracks close has been theoretically linked to the aspect ratio of the cracks and the elastic properties of the rock; the self-consistent theory (Walsh, 1965a) results agree with experimental observations of the quartzite accurately estimating the aspect ratio of the cracks. The Hudson model (1981) was investigated as well but was not a good fit in this case, likely due to the high crack density of the thermally shocked rocks. Alternatively, the models are predicated on rather simple geometrical assumptions with regards to crack shapes. Real cracks, as seen in the microscopic images presented, are substantially more complex; the existing theories may not be adequate to describe such real cracks.

Moduli measurements were undertaken under both loading and unloading. Moduli measured during unloading appear to be stiffer than those measured during

loading. This appears to be simple hysteresis in the response of the cracks to pressure, as, for the most part, loading cycles are repeatable.

Although the elastic moduli of the dry quartzites showed the pressure dependence seen in all the measurements, a comparison of the low and high frequency results at any given pressure shows no dispersion occured when the samples are dry. This is an expected result and confirms dispersion is caused by pore fluid in these rocks. Low frequency shear modulus measurements of both the argon and water saturated quartzites agreed with their dry counterparts, as did the low frequency saturated Young's modulus measurements.

High frequency shear and Young's moduli stiffened when saturated with argon or water pore fluid. The only limitation to this result was the behaviour of the argon saturated Alberta quartzite at effective pressures >50 MPa. It is not clear why these higher pressure argon saturated measurements had anomalous shear and Young's moduli values, but it is expected that this relates to additional cracking which may have occurred in previous pressurization runs, or that the sudden decrease in permeability of the Alberta sample at pressures >50 MPa resulted in insufficient equilibration time for the argon pore fluid. If the argon did not have sufficient time to flow out of the cracks as pressures were increased then these higher pore pressures could mean effective pressures were actually lower than recorded. This second possibility seems unlikely however as, at 10 MPa of pressure, the argon has a viscosity one hundred times less than that of water and an expected required equilibration time in the quartzite on the order of minutes. The otherwise stiffer high frequency moduli indicate that dispersion is occurring. As a result of the higher bulk modulus and viscosity of water, dispersion is

most significant in the water saturated samples. Water saturation of the quartzites causes the high frequency shear modulus to be as much as 189% stiffer than the low frequency modulus. This is significant dispersion, by any measure, but it pales in comparison to the magnitude of dispersion seen in the Young's modulus. The Cape Sorell quartzite records a 1 MHz Young's modulus that is 253% stiffer than its 1 Hz modulus, and 339% stiffer than its 0.01 Hz modulus. The actual dispersion may be even stronger than observed: the high frequency measurements were made during loading, while the low frequency measurements were made during unloading for logistical reasons. Due to the aforementioned crack hysteresis, it is likely low frequency measurements made during loading would have been still more compliant.

The water saturated Young's modulus appears to show dispersion even between 0.01 and 1 Hz, possibly indicating that these measurements lie near a fluid flow regime transition zone. The invariance of the water saturated shear modulus at low frequency, however, indicates that the 0.01-1 Hz measurements do lie in the saturated isobaric, or relaxed, fluid flow regime. This agrees with Gassmann's (1951) prediction of a shear modulus independent of pore fluid saturation. Gassmann's relation fails, however, to predict the low frequency behaviour of the Young's modulus. A combination of Biot (1956) and squirt flow (Mavko and Jizba, 1991) theory accounts for the stiffening of the shear modulus with argon saturation, indicating that all the high frequency saturated measurements are in the saturated isolated, or unrelaxed, fluid flow regime at 1 MHz. The characteristic frequency of Biot, however, falsely indicates that the rocks remain in a relaxed state. In the case of these quartzites, the characteristic frequency predicted by the self-consistent model (O'Connell and Budiansky, 1977) performs much better for

the cracked rocks, accurately predicting a regime transition between 1 Hz and 1 MHz. Although the self-consistent model accurately predicts the characteristic frequency in this case, its theoretical predictions of the moduli themselves were not examined here, and it is therefore not clear if it would accurately predict the elastic moduli. The combined Biot and squirt flow theory substantially underestimates the stiffening effect of the water on the elastic moduli.

This work presents the first experimental low frequency Young's modulus measurements made using the Australian National University apparatus. It demonstrates the flexural mode adaptation is a viable technique for allowing the acquisition of a second independent modulus using the apparatus, in addition to the historically acquired shear modulus measurements. Further, following adaptation of the pore fluid system, this work presents the first experimental measurements made using liquid (water) pore fluid in the apparatus. Very few laboratories worldwide have low frequency measurement capability and fewer still the ability to measure two independent moduli. These adaptations of the Australian National University apparatus are critically important to the advancement of the study of dispersion.

The dispersion results presented in this thesis indicate that some of the most commonly used theories significantly underestimate observed dispersion. It is extremely important to experimentally constrain dispersion theory in order to allow joint interpretation of complementary data sets acquired in different frequency bands. These results are, to the author's knowledge, the first dispersion measurements made on quartzites, and amongst only a very few dispersion measurements made on cracked rock. As the results include two independent moduli and a characterization of the

physical properties of the rocks, they are well placed to advance theoretical understanding of dispersion. In addition, few, if any, measurements of dispersion with supercritical argon pore fluid have been made to date. Most models to date have focused on liquids, gases or weak solids in the pore space; experimental measurement of the dispersive effects of supercritical fluid may serve to further advance theory.

5.3 Conclusions

Most crystalline rocks have porosity dominated by low aspect ratio cracks. The flexural mode adaptation of the ANU apparatus successfully measured Young's moduli of two cracked quartzite specimens at frequencies 0.01-1 Hz. In conjunction with the proven forced torsional oscillation mode of the apparatus and 1 MHz pulse transmission measurements, the elastic properties of the quartzites are fully described across a range of frequencies spanning nine decades. Despite their significant crack porosity, the quartzites are observed to have low permeability, and both permeability and elastic moduli are highly pressure dependent due to crack closure with increasing pressure.

Argon saturation and water saturation are observed to affect the behaviour of the shear and Young's moduli at high frequency, with dramatic stiffening of the moduli occurring when the quartzites are water saturated. Continued frequency dependence of the Young's modulus appears evident in the water saturated results even at frequencies <1 Hz, indicating that dispersion effects may need to be accounted for even within passive seismic measurements of the crystalline crust.

Gassmann, Biot and squirt flow models in general perform quite poorly and are inadequate in estimating both the effects of fluid saturation on the elastic moduli of the quartzites as well as the characteristic frequency of the quartzites. The self-consistent model seems to do somewhat better, accurately predicting the characteristic frequency between fluid flow regimes and the aspect ratio of the rocks, but the estimations of the moduli are not compared here.

Dispersion is observed to have strong effects on the elastic moduli, and therefore the seismic velocities, of crystalline rocks with low aspect ratio cracks. Joint interpretation of data sets involving saturated crystalline rocks need to account for the dispersive effects of fluid flow in order to accurately compare measurements made in different fluid flow regimes. This likely requires significant further experimental work to characterize dispersion in a variety of crystalline rocks, as well as work towards improved theoretical models.

5.4 Future work

Future work on this data set may include comparisons to alternate theoretical models, including a comparison of the moduli predictions of the self-consistent theory. Models with differing crack geometry and interaction assumptions may provide better fits to the experimental results obtained here.

Both the low and high frequency measurements could be analyzed to obtain attenuation information as well. Phase lags of the sample response compared to that of the elastic standard contain shear attenuation information and, although not presented

here, were acquired as part of the low frequency torsional measurements. Similarly, phase lag measurements were collected in the low frequency flexural mode, but additional theoretical work is required to correlate them to an attenuation parameter. The flexural attenuation data would then require modeling and calibration against fused quartz data prior to interpretation of attenuation results for the quartzites. Spectral analysis of the high frequency P- and S-wave data could provide attenuation measurements at 1 MHz, however, it is difficult to determine if the signal to noise levels would be sufficient for this method without further work. Attenuation measurements would provide a second data set for comparison to theoretical models, and increase understanding of the effects of these fluid-filled cracks on seismic data.

Additional experimental work on the two quartzite samples using a low frequency apparatus capable of making measurements in the rather large gap between 1 Hz and 1 MHz would allow further understanding of when and how the water saturated moduli begin to stiffen. Determining the characteristic frequency which separates the fluid flow regimes would allow greater understanding of when velocity dispersion must be accounted for in seismological measurements.

In terms of the experimental method, the learnings from this study have been examined and the flexural mode of the ANU apparatus will undergo further work to attempt to provide greater sensitivity to the Young's moduli of the specimens. The work will include investigations to determine whether different modes of motion (e.g. the electromagnetic drivers working cooperatively in the horizontal plane, rather than in opposition in the vertical plane), boundary conditions on the beam (e.g. with the bottom of the beam weakly propped as opposed to fully propped) or specimen

placement (with the specimen moved higher or lower within the experimental assembly) can improve the sensitivity.

Appendix A: High Frequency Measurement

Seismic properties of a rock can often inform of its porosity, saturation or lithology, while well defined seismic velocities can aid in improving the quality of seismic reflection imaging. There are many reasons to require accurate knowledge of the seismic properties, but it is often logistically difficult or costly to acquire in-situ measurements, and results may be more difficult to interpret due to heterogeneity within a survey area. Laboratory measurements on core samples provide a relatively inexpensive method of obtaining this information, and ultrasonic pulse transmission is commonly used for this purpose (Adam *et al.*, 2006, Adelinet *et al.*, 2010, Batzle *et al.*, 2006, Cholach *et al.*, 2005, Kern *et al.*, 2008, Martinez and Schmitt, 2013). This appendix describes the technique and the University of Alberta equipment.

A.1 Preparation of Transducers and Experimental Set Up

Ultrasonic pulse transmission is typically undertaken using piezoelectric transducers excited by a pulsed voltage. The voltage stimulates a piezoelectric at one end of the sample and produces an acoustic wave. The acoustic wave travels through the sample and is received by a piezoelectric at the other end where it is converted back into a voltage. The resulting voltage is recorded by an oscilloscope. Here, the setup includes a pressure vessel which allows confining and pore pressure (either liquid or gas) to be applied independently of each other to the sample (Fig. A.1).

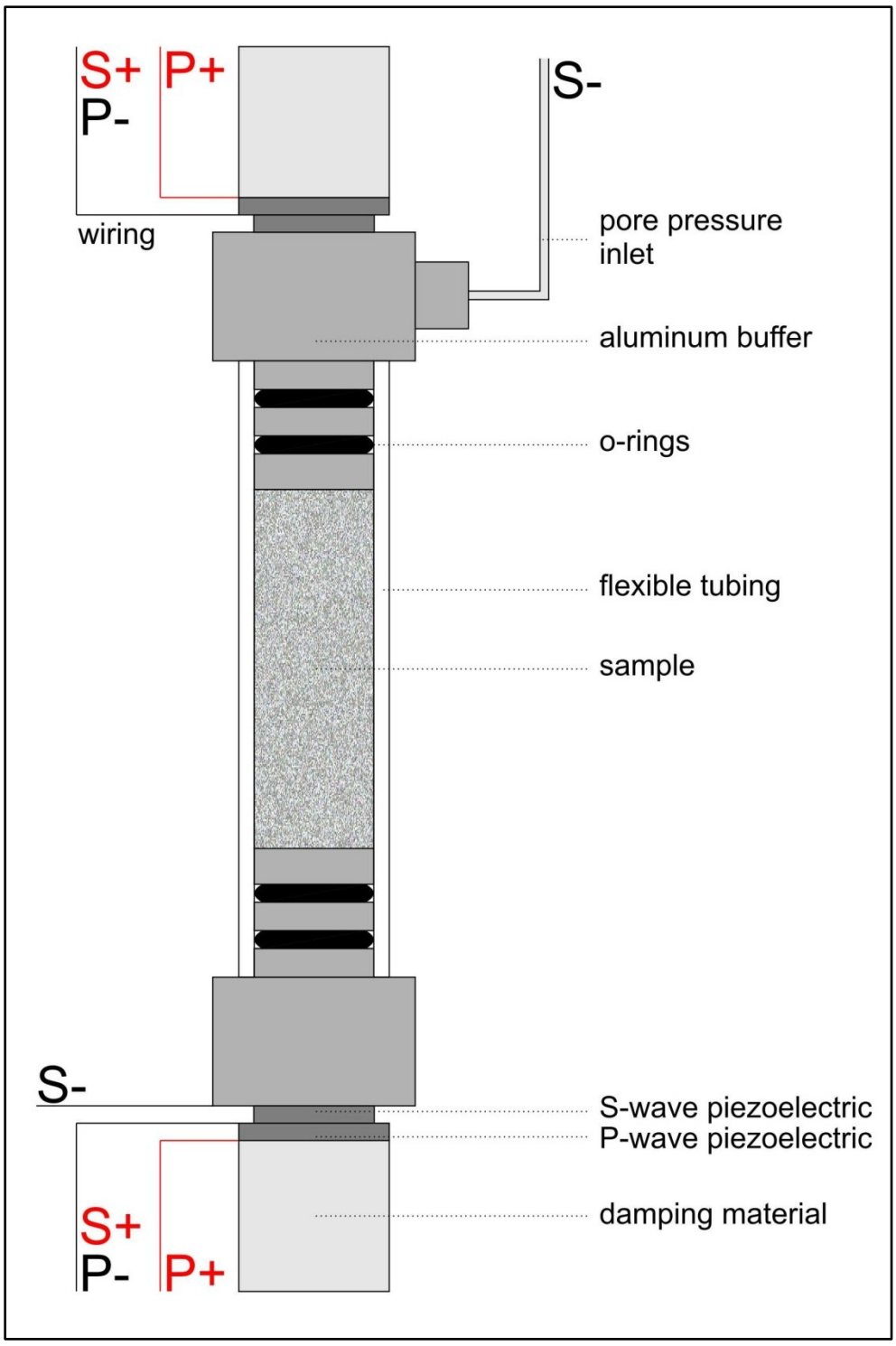

Figure A.1: Set up for ultrasonic measurement of core samples in the University of Alberta pressure vessel.

The building of the piezoelectric transducers is somewhat involved. Two piezoelectric ceramics, one polarized to produce P-waves and one polarized for S-wave transmission, are affixed to aluminum buffers which are coupled with the sample. There are multiple reasons for not affixing the piezoelectrics to the sample directly. First and foremost, the aluminum buffers, in conjunction with a jacket made of plastic tubing, allow the sample to be isolated from the confining fluid. This allows the introduction and independent control of pore fluid into the sample via a small pore fluid inlet in one of the aluminum buffers. Although time of flight calculations, determining the travel time through the sample, are complicated by the necessity of subtracting the travel time through the aluminum buffers, building the transducers as separate entities from the core samples allows the transducers to be used on multiple samples. This increases consistency in the signal and decreases labour overall. Finally, the piezoelectric material has a 'rise' time which means that the onset of the voltage stimulation does not correspond exactly with the onset of the deformation of the piezoelectric ceramic. The PR35 pulser (JSR Ultrasonics, New York) transmits a fast (5 ns) rise square wave, with voltage of ~30-100 V peak-to-peak across the piezoelectric ceramic, depending on experimental parameters. The transmitted signal, recorded by an oscilloscope (LabView, National Instruments, Texas) at a sampling rate of 10 ns, shows a slight delay. Experiments done with the piezoelectrics mounted directly onto fused quartz specimens of varying length indicate that the lead zirconate titanate (PZT) SP5-A piezoelectrics (Sparkler Ceramics Pvt. Ltd., India) used here do not produce a peak pressure (or acceleration) until ~0.4 μs after they are stimulated with a voltage (Fig. A.2).

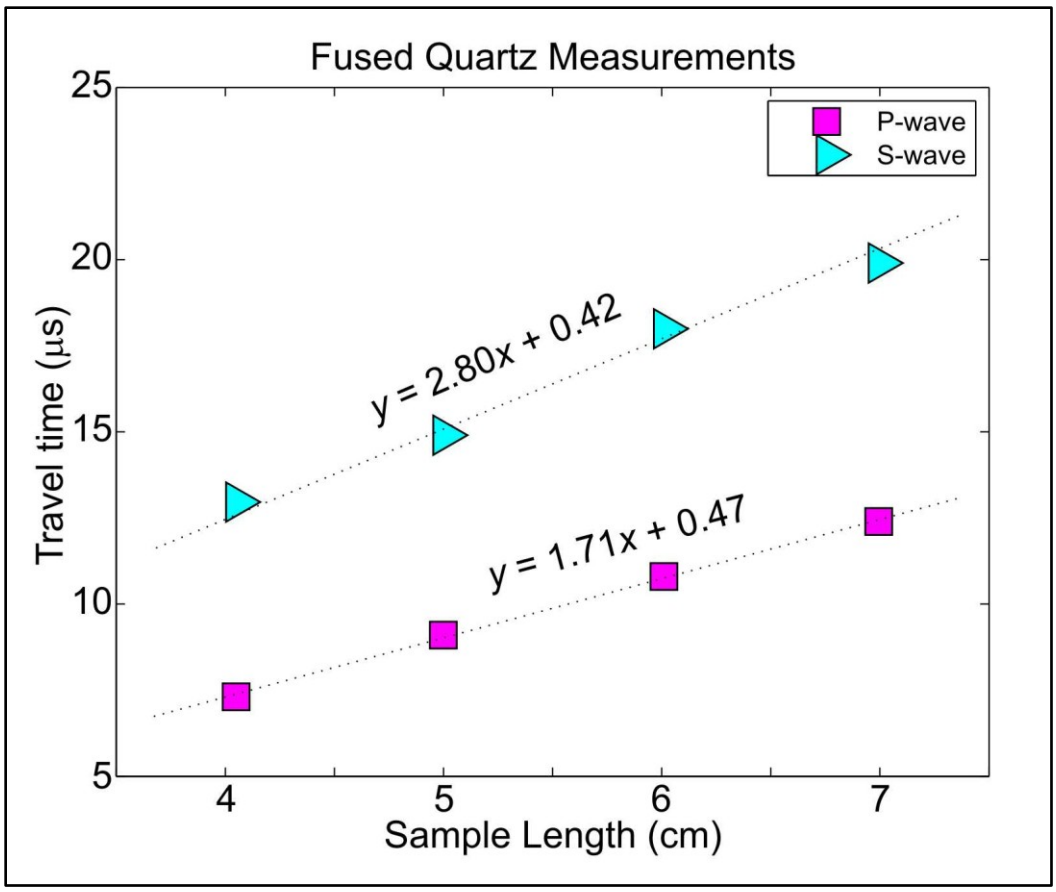

Figure A.2: Experimental measurements done with the piezoelectrics mounted directly onto fused quartz specimens of varying length indicate that both the P- and S-wave ceramics require a finite amount of time to produce an acoustic pulse (0.47 μs and 0.42 μs, respectively).

The aluminum buffers have the S-wave ceramic mounted flush against their surface using a silver epoxy. The silver epoxy electrically couples the piezoelectric ceramic to the buffer, and a grounding wire is connected to the buffer to provide for the negative lead from the ceramic. A flat copper sheet is cut slightly larger than the S-wave ceramic and epoxied on top of it. The positive lead for the shear-wave is soldered to the edge of the copper, and also serves as the negative lead for the P-wave ceramic which is stacked on top of both the S-wave ceramic and copper sheet. A final copper sheet and wire is attached on top of the P-wave ceramic to allow the provision of voltage across the P-wave piezoelectric. As the aluminum buffer and the ceramics themselves are fairly linearly elastic, a damping material is affixed to the top of the P-wave ceramic to provide damping to both the P- and S-wave signals. The damping material is composed of Flexane® 80 (Devcon, Massachussets), a viscous urethane compound, and lead powder. Finally, the piezoelectrics and damping material are sealed in a coating of Flexane® 80 in order to protect them from the pressurizing fluid (oil) of the University of Alberta pressure vessel. The Flexane® 80, even with the aid of primers, does not bond strongly with the aluminum surface of the buffers, and the transducers typically have a limited life before the highly pressurized oil delaminates the piezoelectrics from the surface of the buffer and the tranducer must be rebuilt.

After preparation of the transducers, the sample is placed in a Tygon® (Saint-Gobain, France) tubing jacket. One buffer is placed on top and one below the sample, with the bottom half of each aluminum buffer being inserted into the tubing jacket as well. The bottom of each aluminum buffer is of the same diameter as the sample (1.5 cm), and has two o-rings to seal against the Tygon®. The buffers are rotated so as to

align the S-wave piezoelectrics and the samples and buffers are placed in a drill press. The drill press is used to obtain contact between the sample and the adjoining surfaces of the buffers. While they are being held together by the drill press, a steel hose-clamp is tightened around the tubing, one on top of each o-ring. This ensures that jacket is able to seal the sample from the pressurizing fluid at confining pressures up to 200 MPa.

The pore pressure tubing is connected to the sample, and the prepared sample is inserted into the pressure vessel. The transducer wires are connected through feed-throughs in the pressure vessel to the pulser and oscilloscope. Confining and/or pore pressure are applied, and, after sufficient time has been allowed for the pressurized fluid to return to room temperature, and the sample to be evenly saturated (if pore pressure is being applied), measurement on the sample can commence.

It is necessary to measure the travel time through the buffers alone as well, and in this case the preparation is as above except the sample is not placed in between the buffers and, instead, the buffers are in direct contact with each other. The travel time through the buffers is measured for the same effective pressures as the sample is subjected to, in order to capture the effects of pressure on the buffers (Fig. A.3). Two sets of buffers were used in this experiment, buffers #100711 and buffers #101204. In order to account for any potential differences in travel time due to varying thicknesses of epoxy or copper sheeting in the building of the transducers, as well as the signal itself as a result of differences in the damping or manufacturing of the ceramics, it is necessary to measure the travel times through both sets in order to properly remove this time from the overall transit time and determine the travel time through the sample alone (Fig. A.4). The final travel time through the sample is calculated by subtracting the

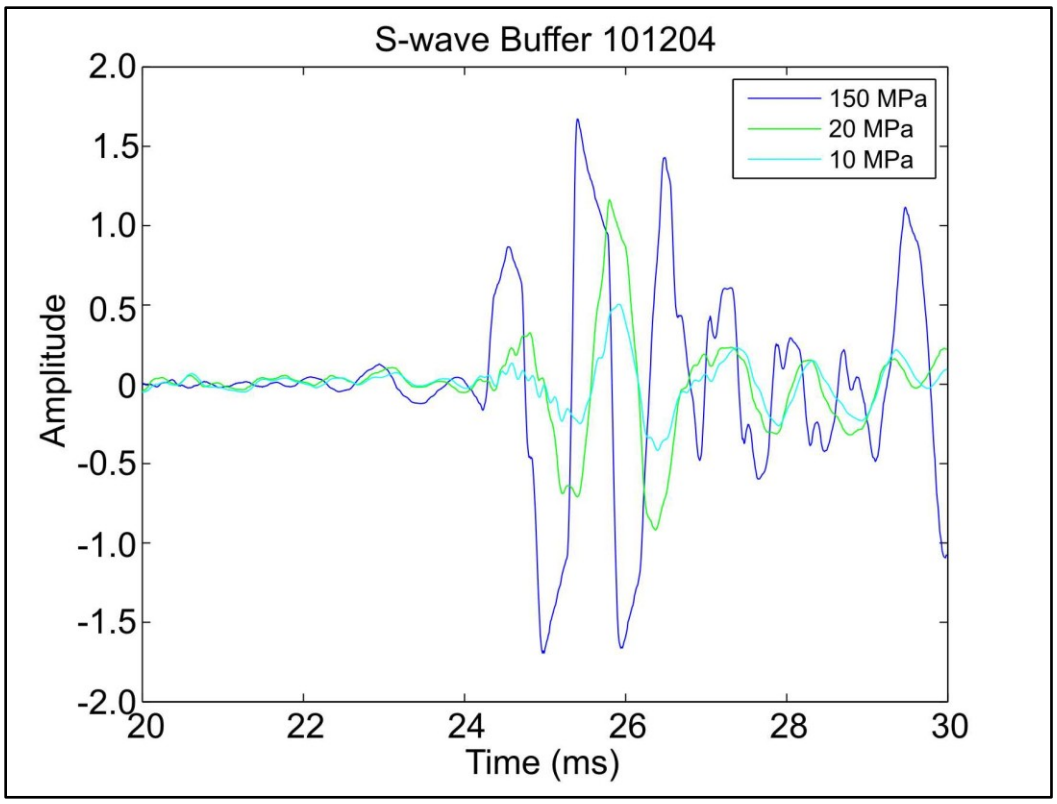

Figure A.3: The waveform transmitted by the buffer arrives earlier, and changes characteristic shape with increasing effective pressure as the buffers couple better to each other (or the sample, if it is present) and the damping material is compressed to a denser form.

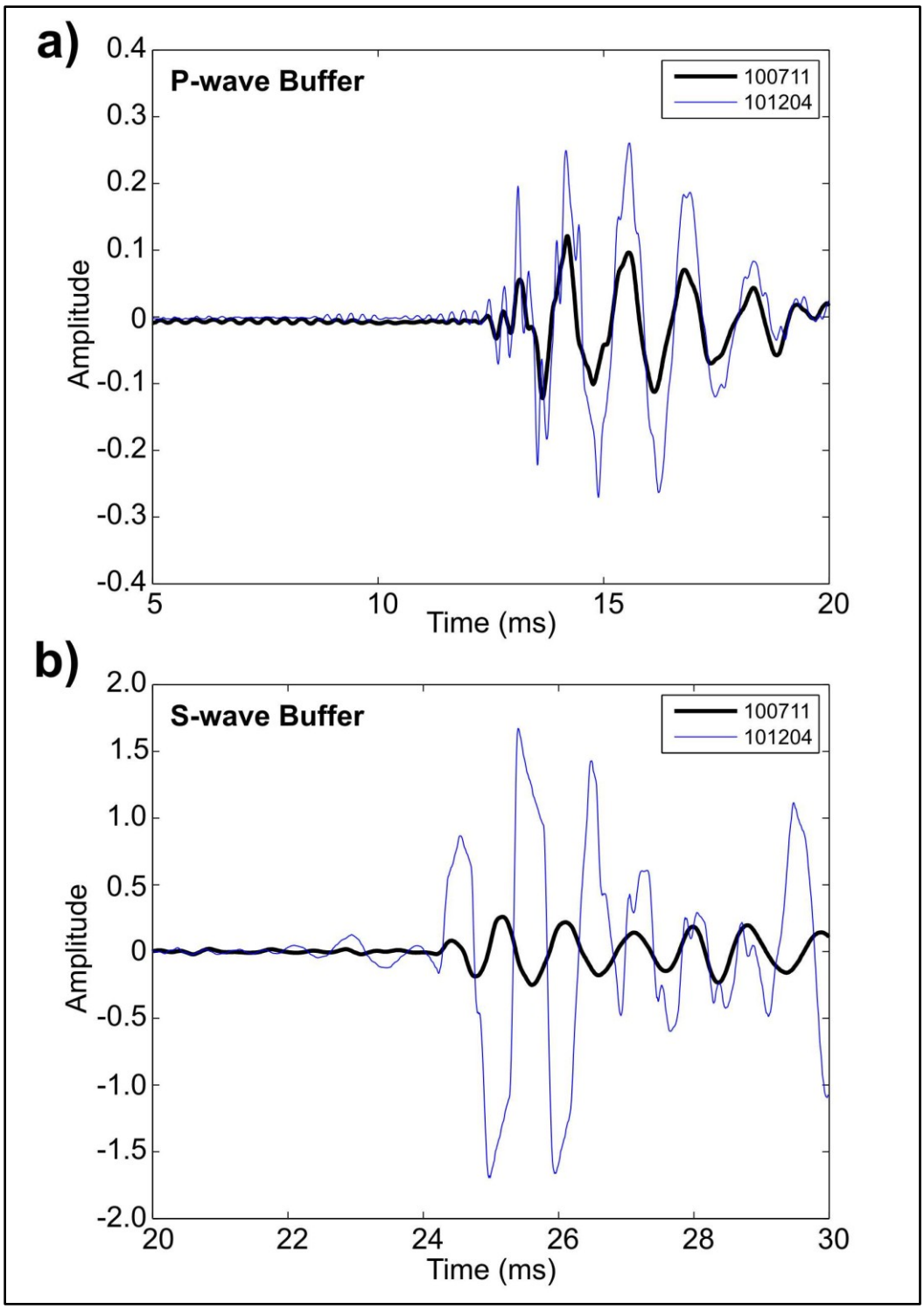

Figure A.4: Different characteristic waveforms of the P- (a) and S-waves (b) of the two transducers used in the experiment.

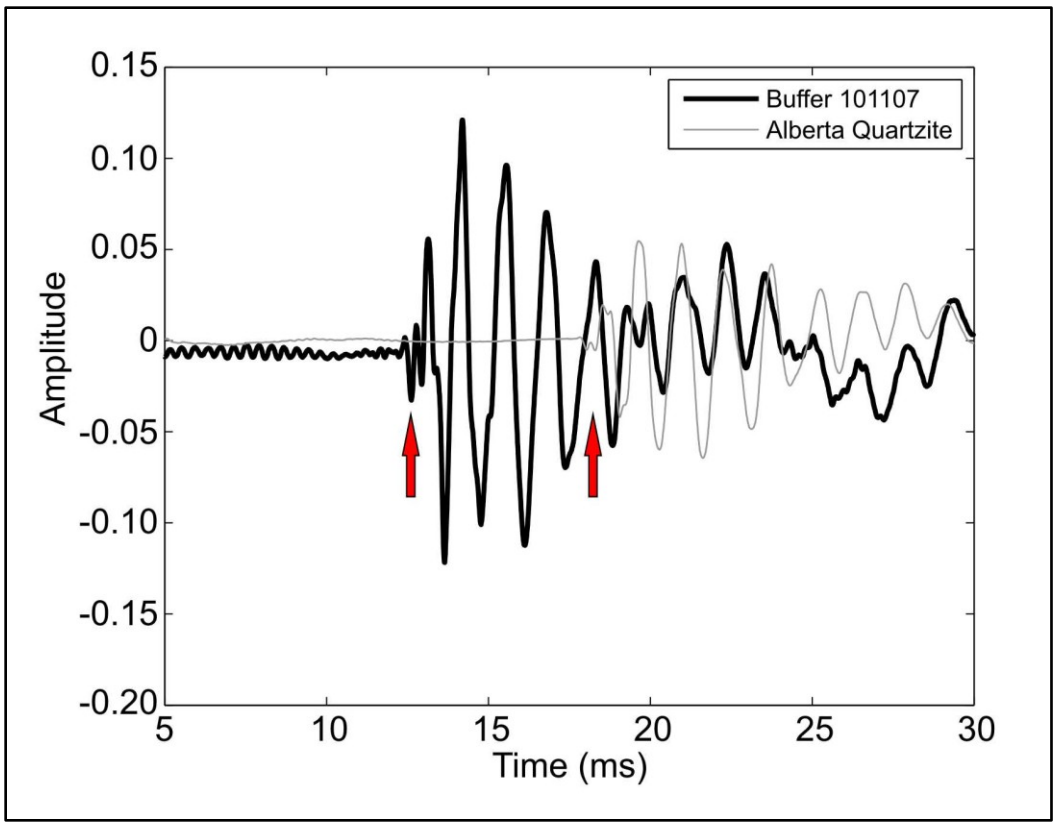

Figure A.5: The final P-wave travel time through the dry Alberta quartzite at 150 MPa of confining pressure is determined by subtracting the travel time through the buffer alone from the total travel time; both first extremums are highlighted with arrows.

through the use of the fused quartz standard travel time through the buffer at equivalent effective pressure (Fig. A.5). In all cases, the first extremum that could be picked through the whole pressure record was used, with the corresponding aspect of buffer waveform picked as the buffer travel time. This was typically the first extremum, but for the S-waves, where there was occasionally P-wave contamination in the record, the second, higher amplitude, extremum was required on some occasions for the dry and argon saturated samples in order to have confidence in the time pick. In order to increase the signal to noise ratio of the first arrival as much as possible, the signal was stacked. An acceptable signal to noise ratio was usually achieved with ~1000 stacks.

A.2 Waveform characteristics

It is necessary to investigate the properties of the ultrasonic wave transmitted through the samples; in particular the frequency content of the nominally 1 MHz piezoelectric ceramics and the induced strain of the measurements. The piezoelectrics are manufactured to have a frequency centred around 1 MHz, although some spread in the frequency content is typically expected. A fast Fourier transform of the P- and S-waves through the buffers at high pressure (150 MPa) shows that while the S-waves are indeed centred around 1 MHz, the transmitted P-waves appear to be slightly lower than the nominal frequency, with a centre frequency around 800 kHz (Fig. A.6). For both the P- and S-waves there is significant higher frequency noise present. The wires are only thinly insulated, as they must pass through feed throughs to enter or exit the pressure vessel, and some of the noise is electrical. Most, however, is acoustic, and it is more pronounced at lower pressures where the coupling between the buffers and sample is

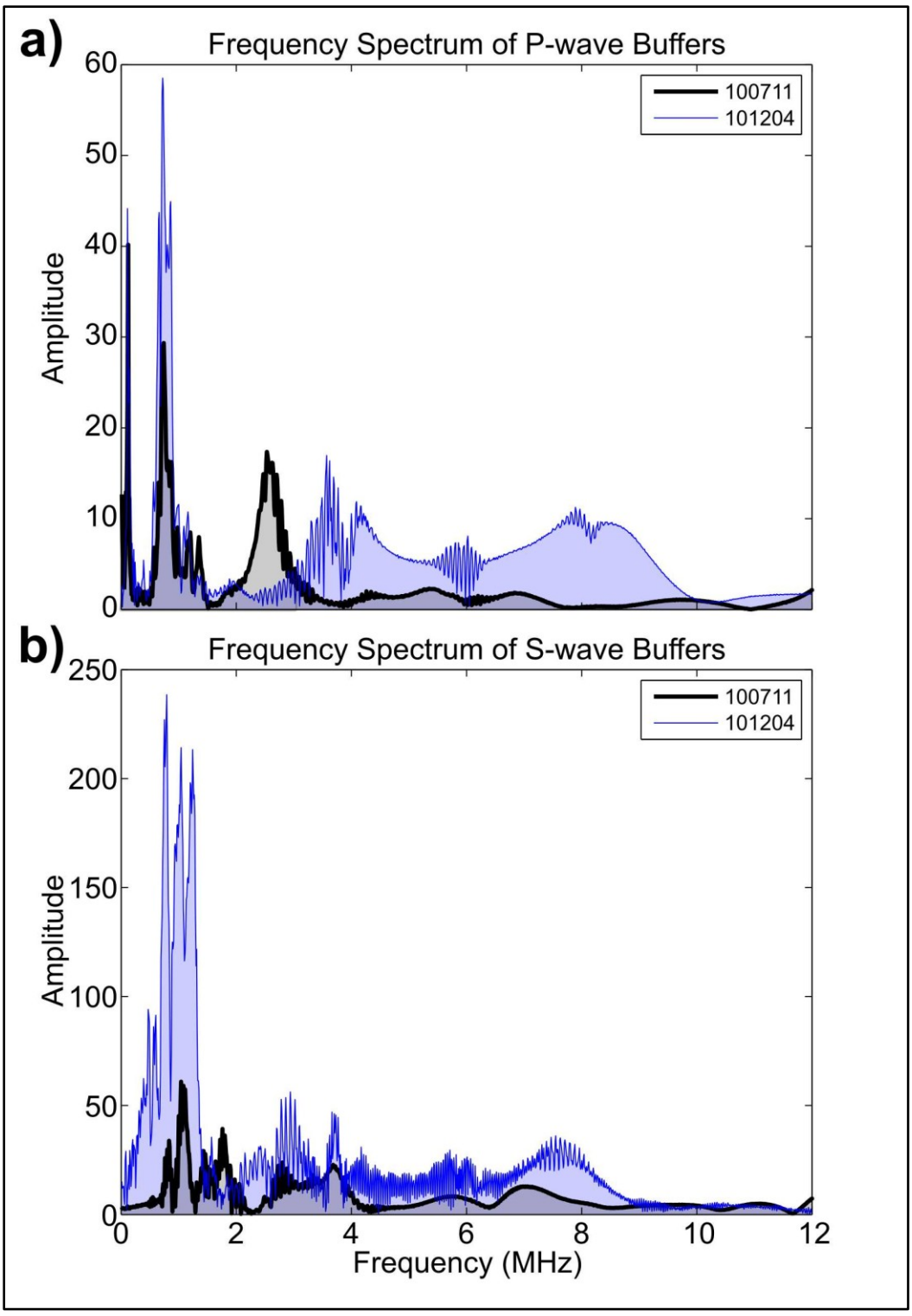

Figure A.6: Frequency content of the transmitted waves from the P- (a) and S-wave (b) buffers at 150 MPa of pressure. The P-wave has a peak around 800 kHz, while the S-wave peaks around 1 MHz; both have significant higher frequency noise.

less firm and allows for more 'bouncing.' In these cases it is occasionally necessary to apply a low pass filter prior to picking travel times; usually removing frequencies >6 MHz. If a bandpass filter is applied to the signal for a given effective pressure, it is applied to the buffer-only record as well in order to maintain consistency in time picks.

The strain induced in the rock samples is more difficult to measure. Seismic velocity measurements are strongly dependent on the magnitude of applied strain (Iwasaki *et al.*, 1978) and it is necessary to ensure laboratory measurements are made in the same strain regime as in-situ seismic techniques. In practice, this typically requires a strain amplitude below ~10^{-6}. The P-wave ceramic is circular in shape and 2 mm thick, with a piezoelectric voltage constant, *g*, of 25 mV·m/N according to the manufacturer. When excited by the PR35 pulse (JSR Ultrasonics, New York), typically the mechanical stress, σ_{ij}, can be calculated:

$$\sigma_{ij} = \frac{V}{d_t g_{ij}} \qquad \text{i,j = 1,2,3} \qquad \text{(A1.1)}$$

using the electric field calculated from the voltage, *V*, and thickness of the ceramic, d_t. Measurements from the almost perfectly elastic aluminum buffers, without a sample, register a voltage of ~10 mV for the P- and S-wave transducers. The stress is on the order of 200 Pa. For the S-wave ceramic, with voltage constant -11 mV·m/N and thickness of 0.8 mm, the stress is somewhat higher, with a magnitude around 1 kPa. The stress is across the surface area of the ceramic; the P-wave is a disk with diameter 18 mm, while the S-wave is a square shape with length and width 15 mm. Although

some dissipation and reflection occurs, the majority of the force is applied to the surface of the cylindrical samples, with diameter 15 mm. The resulting stress is related to the induced strain, ε_{ij} through the Young's modulus, *E*, of the rock by Hooke's Law:

$$\varepsilon_{ij} = \frac{\sigma_{ij}}{E}. \qquad \text{i,j = 1,2,3} \qquad \text{(A1.2)}$$

For the samples in this study, with Young's moduli spanning almost an order of magnitude, from approximately 10-80 GPa, this results in theoretical strains on the order of 10^{-7} to 10^{-8} for the S-wave and ~10^{-8} for the P-wave. These strains are maximums, as they assume complete transmission of the seismic wave. The strains are well within the seismic regime, rendering the ultrasonic measurements appropriate for extrapolation to in-situ seismic results.

Appendix B: A versatile facility for laboratory studies of viscoelastic and poroelastic behaviour of rocks[2]

Ian Jackson[a], Heather Schijns[b], Douglas R. Schmitt[b], Junjie Mu[c], Alison Delmenico[c]

[a] Research School of Earth Sciences, Australian National University, Canberra ACT, Australia

[b] Department of Physics, University of Alberta, Edmonton, Alberta, Canada

[c] Department of Engineering, Australian National University, Canberra ACT, Australia

B.1 Introduction

Because empty (or air-filled) cracks are highly compliant both in shear and compression, crack porosity has a disproportionately large effect on elastic moduli. For example, for the case of a crack porosity ϕ of only 0.001 (i. e. 0.1% by volume) and aspect ratio α of 0.001 (e. g., μm aperture for grain-boundary cracks of mm length in a tight crystalline rock) the bulk and shear moduli, and the associated compressional and shear wave speeds V_P and V_S are estimated to decrease by 44, 26, 20 and 14%, respectively [1, 2].

Saturation of the crack network with a fluid of moderate incompressibility (such as water) has the potential to significantly reduce the crack compliance, particularly in compression. However, there is an additional major complication. The differential compliance of different parts of the pore space (cracks of different aspect ratio and/or

[2] A version of this chapter has been published. Jackson, I., Schijns, H., Schmitt, D.R., Mu, J.J. & Delmenico, A., 2011. A versatile facility for laboratory studies of viscoelastic and poroelastic behaviour of rocks, *Review of Scientific Instruments,* 82.

different orientation relative to the applied stress) will result in a spatially variable pore pressure driving a fluid flux proportional to permeability divided by viscosity. The potential for such redistribution of pore fluid during mechanical loading on sufficiently long timescales means that the effective elastic moduli of cracked and fluid-saturated rocks must inevitably be strongly frequency dependent. With decreasing frequency, the fluid becomes amenable to stress-induced redistribution by bulk fluid flow. The spatial scale, and hence characteristic timescale or frequency, for the stress-induced fluid flow range widely from that of individual grains (~ mm) through the typical dimensions (1-10 cm) of laboratory rock specimens to those of joints in rock masses and seismic wavelengths.

The result is a series of conceptually distinct fluid-flow regimes between which significant partial relaxations of the effective moduli and associated attenuation are expected [3]. Within the saturated-isolated regime, encountered at sufficiently high frequencies, fluid flow even between adjacent parts of the pore space of different orientation or aspect ratio is precluded. However, for somewhat lower frequencies, 'squirt' flow of fluid between adjacent cracks of different orientation is predicted to cause a partial relaxation of the shear modulus [4]. A similar relaxation of the bulk modulus associated with the transition to saturated-isobaric conditions requires the existence of a distribution $p(\alpha)$ of aspect ratios and fluid flow, for example, between cracks and more nearly equant pores. Such dissipation of compressive energy and associated partial relaxation of the bulk modulus are thus vitally important in media containing a fluid phase substantially more compressible than the crystalline matrix (e.g., aqueous fluid or melt) but also in materials containing coexisting low- and high-pressure crystalline phases of different specific volume.

The frequency-dependence of elastic wave speeds and associated attenuation in cracked and fluid-saturated media, predicted by such theoretical models, remains largely untested against experimental data because of the scarcity of experimental measurements at frequencies lower than those (~ MHz) of ultrasonic wave propagation. However, there is growing interest in the development of low-frequency/broadband laboratory methods for the study of such frequency dependence of seismic wave speeds in fluid-saturated rocks[5-9] . Forced-oscillation methods have been intensively used during the past decade in seismic-frequency (mHz-Hz) laboratory studies of high-temperature shear-mode viscoelasticity[10,11], but much less attention has been paid to the relaxation of the bulk modulus. This phenomenon is also experimentally accessible with forced-oscillation methods - involving either oscillating confining pressure[9], alternating compression-extension [5,6,8,12], or flexure.

In extensional oscillation, the oscillating fluid flow between the stressed interior of a rock specimen and an external reservoir, maintained at constant fluid pressure, establishes drained conditions for frequencies < $f_D = kK_f/\eta\phi R^2$ [13-16] – of order Hz for water-saturation of tight crystalline rocks. Here, ϕ and k are the porosity and permeability of a cylindrical rock specimen of radius R, and K_f and η are the fluid incompressibility and viscosity, respectively. For flexural oscillation (as for the torsional mode), there is no stress-induced change in the spatially averaged pore pressure within the specimen (of constant volume), so that draining is not an issue. However, lateral fluid flow between the opposite sides of a flexural-mode specimen instantaneously experiencing compression and extension, will result in poroelastic relaxation more pronounced than for draining in the extensional mode, and at similar frequencies [14].

The dissipation peak, and modulus relaxation, associated with such specimen-scale fluid flow is thus a significant artifact to be anticipated in flexural mode laboratory measurements on fluid-saturated media [13-15]. It can be identified from its characteristic frequency f_D, if the permeability and other parameters appearing in the expression for f_D are known [13,14] with confirmation potentially provided by the expected $f_D \sim R^{-2}$ dependence [15]. Moreover, the characteristic frequency $f_F = K_f \alpha^3 / \eta^3$ for squirt of water between adjacent cracks of aspect ratio α in tight, fine-grained crystalline rock, is expected to exceed f_D by a factor of ~1000. Under such conditions, the relaxations associated with local and global (sample-wide) fluid flow should be widely separated in frequency. Finally, the systematic use of complementary torsional and flexural mode measurements on the same, simple synthetic cracked/porous media such as thermally cracked ceramics and synthetic sandstones of low porosity prepared by sintering glass beads [17], will also help separate the relaxations associated with local and global fluid flow.

Further work, beyond the scope of this study, will focus on the development of such strategies to distinguish between the relaxations associated with fluid flow ('squirt') between adjacent parts of the pore space and sample-wide fluid flow in cracked and fluid-saturated media. Here, however, our purpose is to demonstrate the technical feasibility of sub-microstrain flexural-oscillation methods for use alongside the established torsional mode capability of the ANU rock physics laboratory – for which purpose we use a fused silica control specimen.

B.2 Experimental method

B.2.1 The modified forced-oscillation apparatus

Novel equipment for seismic-frequency torsional forced-oscillation measurements under conditions of simultaneous high pressure and temperature, previously described in detail [10], has recently been modified to provide access also to the flexural oscillation mode by using alternative polarisations of the electromagnetic driver and capacitance displacement transducers (Fig. B.1). The combination of more powerful electromagnetic drivers (incorporating rare-earth magnets) and the same mechanical advantage as available for the torsional mode (Fig. B.1) allows flexural mode measurements with high signal/noise ratio as demonstrated below.

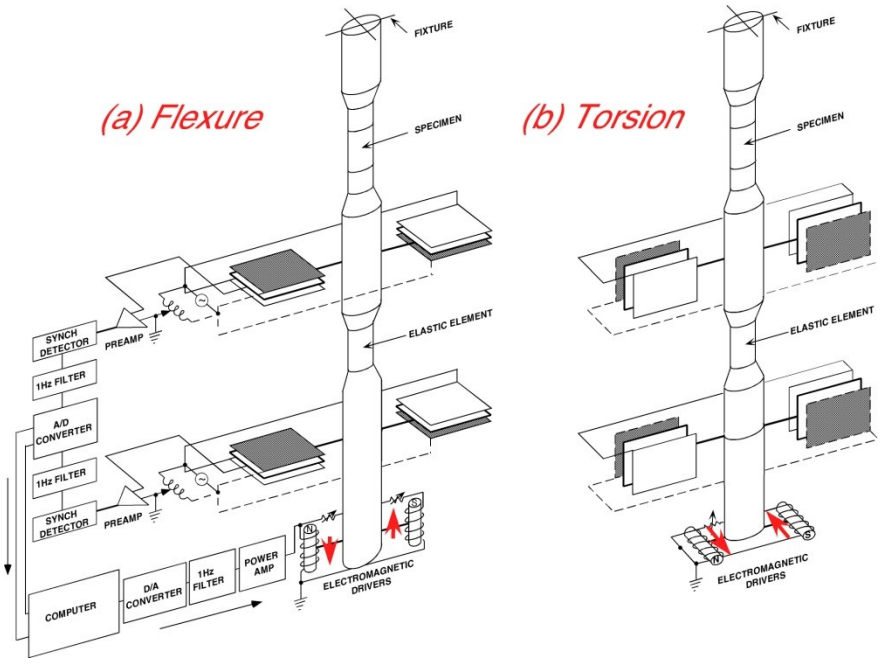

Figure B.1: Experimental arrangement for forced-oscillation studies in (a) flexure and (b) torsion with alternative driver/displacement transducer polarizations.

The distortion of the experimental assembly undergoing forced oscillation is measured by sensitive three-plate capacitance displacement transducers operated in pairs at locations above and below the hollow steel elastic element (Fig. B.1). Diagonally opposite capacitors are connected in parallel (Fig. B.1) in order to maximise the sensitivity to torsional or flexural mode distortions of the column for the alternative driver/transducer polarizations, and to minimize the response to any subsidiary excitation of the flexural or extensional modes, respectively. At each measurement station, the parallel combinations of diagonally opposite capacitors, are connected to a ratio transformer to form an AC bridge, operated at 10 kHz with either 3 or 30 V excitation. Under static operational conditions, the bridge is balanced by adjustment of the transformer ratio. The bridge out-of-balance signal associated with torsional/flexural oscillation is subject to synchronous detection, followed by low-pass (1 Hz) filtering, analogue/digital conversion and digital data acquisition (Fig. B.1a). Calibration of the resulting voltage-versus-time signals is done by measuring the voltage offset associated with reversed switching of the transformer ratio through an appropriate increment. The experimental arrangements, with application to torsional mode measurements, have previously been described in detail [10].

The raw experimental data obtained in flexural oscillation (at periods currently between 1 and 1000 s, although shorter periods to ~ 0.1 s may ultimately prove feasible) are thus sinusoidally time-varying displacements $d_1(t)$ and $d_2(t)$ measured by the parallel combinations of capacitance displacement transducers, located respectively above and below the elastic element (Fig. B.1a). These displacements $d_i(t)$, (i = 1, 2), measured at a distance D from the axis of the specimen assembly at distances $x = l_i$ from the upper,

cantilevered end of the specimen assembly, are related to the flexure $v(x)$ by

$$d_i(t) = Dv'(l_i,t), \qquad \text{(B.1)}$$

$v'(l_i,t)$ being the instantaneous value of the local angle of flexure, i.e. $\partial v/\partial x$.

B.2.2 Pore-fluid system

In anticipation of the application of our forced-oscillation methods to cracked and fluid-saturated rocks and synthetic analogues, we have constructed and tested a system for the delivery, pressurisation and monitoring of pore fluid – either argon gas or condensed pore fluids such as water (Fig. B.2). For this purpose, a cylindrical rock specimen of 15 mm diameter is sandwiched between hollow ceramic and steel pistons enclosed within an annealed copper tube of 0.25 mm wall thickness, that is sealed with an O-ring at either end to exclude the argon pressure medium. The hollow ceramic and steel pistons connect the pores space within the jacketted specimen to the upper and lower pore-fluid reservoirs. This arrangement allows independent variation of confining and pore-fluid pressures to 200 MPa. The capacity to isolate the upstream and downstream reservoirs provides for the in situ measurement of permeability through observation of the return to equilibrium following the imposition of a small fluid-pressure differential between the two reservoirs [18]. The pore-fluid volumometer, previously used in the ANU Rock Physics laboratory, allows measurement of pressure-dependent changes in pore-fluid volume and hence storage capacity [19].

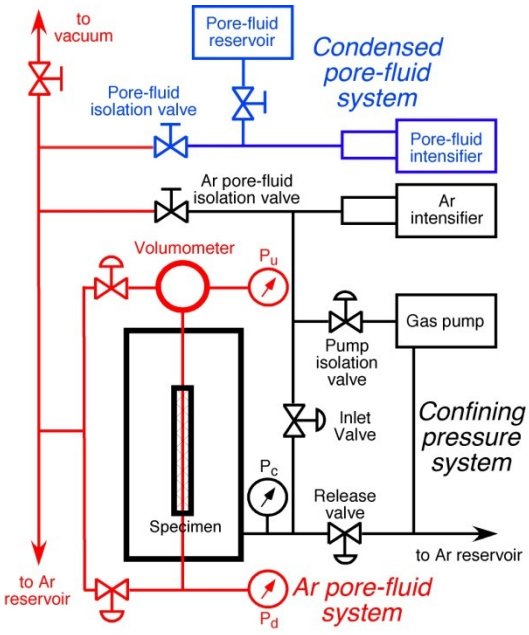

Figure B.2: Arrangements for independent control of the argon confining pressure (black) and either gaseous (argon - red) or condensed (blue) pore fluid pressure.

B.2.3 Specimen assemblies tested in this study

The specimen assemblies employed in trialling the new flexural mode capability consist of cylindrical fused silica specimens sandwiched between disks of annealed copper (Fig. B.3). These components are assembled within a thin-walled sleeve (15.0 mm I.D. $\times$ 15.5 mm O.D.) of annealed copper that is sealed with O-rings against hollow steel members above and below.

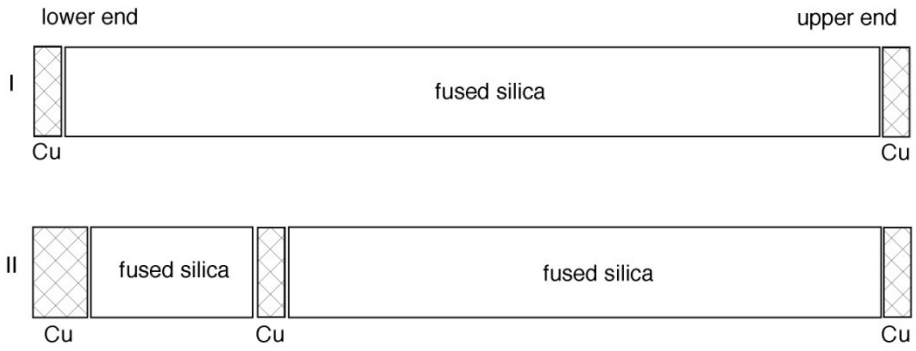

Figure B.3: Experimental assemblies of diameter 15 mm (14.89 mm for fused silica) and total length 338-339 mm, enclosed in Cu sleeves of 0.25 mm wall thickness, that were used in trials of the flexural oscillation technique.

B.2.4 Interim analysis of experimental data

The zero-to-peak displacement amplitudes $|d_1|$ and $|d_2|$ and their relative phase, estimated by Fourier analysis, are first used to calculated the amplitude and phase of the difference signal $d_{12} = d_2 - d_1$, representing the distortion of the elastic element. As an interim measure, pending inversion of the experimental data for the complex Young's modulus of the specimen itself, the results of the flexural oscillation measurements will be presented here as the distortion of the entire specimen assembly comprising the specimen and spacers (Fig. B.3), and the hollow steel members between which they are sandwiched (Fig. B.1). In comparing d_1, a measure of the flexure of the specimen assembly, to that (d_{12}) of the elastic element, we define a normalised flexural 'modulus' S_{NF} as

$$S_{NF} = |d_1/d_{12}| = |d_1/(d_2 - d_1)| \qquad \text{(B.2)}$$

and the loss angle δ (rad) as the phase lag of d_1 relative to d_{12}, reflecting any strain energy dissipation associated with poroelastic or viscoelastic behaviour of the specimen.

The maximum strain amplitude ε_{xx} for the most highly stressed part of the cylindrical surface of the specimen can be estimated from its radius of curvature $R_c = |d^2v/dx^2|^{-1}$, with the curvature d^2v/dx^2 approximated by $v'(l_1)/L_s$, where L_s is the length of the specimen, where the flexure of the specimen assembly is concentrated. Thus, with the help of eq. (B.1), we derive the relationship

$$\varepsilon_{xx} = d_s/2R_c = d_s d_1/2DL_s \qquad \text{(B.3)}$$

where d_s is the diameter of the specimen.

B.3 Numerical modelling

B.3.1 Finite-difference modelling of the flexure of a thin beam

In parallel with the experimental work, we have used numerical modelling methods to simulate the flexural response of the experimental assembly. The static lateral deflection $v(x)$ of a long thin beam ($0 < x < L$) is controlled mainly by the extension/contraction of its constituent longitudinal filaments through the differential equation

$$E(x)I(x)\partial^2 v/\partial x^2 = -M(x) \qquad \text{(B.4)}$$

where E, I and M are respectively the Young's modulus, the diametral moment of inertia of the beam cross-section, and the local bending moment [20]. At this level of approximation, the shear stresses acting at the interfaces between adjacent filaments are ignored, and a finite-difference approach may be used to solve equation (B.4) subject to the appropriate boundary conditions. Implementation of the finite-difference strategy is described in the Appendix.

For comparison with the experimentally determined normalised flexural modulus (eq. 2), we extract from the results of the finite-difference (and finite-element) modelling the corresponding quantity

$$S_{\mathrm{mod}} = |v'(l_1)/[v'(l_2) - v'(l_1)]|. \qquad \text{(B.5)}$$

The significance of S_{mod} as a measure of the mechanical response of the specimen assembly, and ultimately of the specimen itself, is assessed by integrating eq. (B.2) with the local bending moment $M(x)$ appropriately specified by eq. (A3) to obtain

$$v'(x) = M_a \int_0^x dx/[E(x)I(x)] - R_L \int_0^x (L-x)dx/[E(x)I(x)] \qquad \text{(B.6)}$$

In the absence of the terminal reaction force, i.e. for $R_{\mathrm{L}} = 0$, and with the bending moment M_{a} applied at $x = l_3$ within the interval (l_2, L), the local angle of flexure per unit bending moment $v'(x)/M_{\mathrm{a}}$ assumes the simple form

$$v'(x)/(M_a x) = (1/x)\int_0^x dx/[E(x)I(x)] \qquad \text{(B.7)}$$

that is readily interpreted as the integral flexural compliance, $[E(x)I(x)]^{-1}$ being the reciprocal of the flexural rigidity. Appropriately, this integral flexural compliance (eq. B.7) is not weighted by position x along the beam, and increases monotonically with increasing x, and decreases with increasing $E(x)$, as expected from crack closure under increasing confining pressure, for example.

In the presence of a non-zero terminal load R_L only, responsible for a local bending moment $M(x) = R_L(L-x)$, the angle of deflection per unit terminal bending moment is

$$\left|v'(x)/LR_L\right| = \int_0^x (1-x/L)dx/[E(x)I(x)] \qquad \text{(B.8)}$$

which is a different measure of integral flexural compliance, being the integral of the reciprocal flexural rigidity $[E(x)I(x)]^{-1}$ weighted by the fractional length $1 - x/L$ of the mechanical lever. This quantity also increases monotonically with increasing x, and decreases with increasing $E(x)$.

For the propped cantilevered beam, the responses to the applied bending moment M_a and to the terminal reaction force are combined with opposite signs (eq. 6), and the fact that the statically indeterminate reaction force R_L is itself part of the solution (see eqs. A5-A9 of the Appendix), further complicates the situation. Under these circumstances, S_{mod} given by eq. (B.5) becomes

$$S_{\mathrm{mod}} = \{M_a \int_0^{l_1} dx/[E(x)I(x)] - R_L \int_0^{l_1} (L-x)dx/[E(x)I(x)\}/\ldots$$
$$\{M_a \int_{l_1}^{l_2} dx/[E(x)I(x)] - R_L \int_{l_1}^{l_2} (L-x)dx/[E(x)I(x)]\} \quad \text{(B.9)}$$

that cannot be interpreted as a compliance. It is for this reason that we use the neutral term 'normalised flexural modulus' given previously for S_{NF} (eq. B.2).

B.3.2 Finite-element modelling

Complementary finite-element calculations were performed with *Strand7*™ software. A model for the entire experimental assembly was constructed from a total of 23 segments – each of specified geometry and material properties (Young's modulus *E* and shear modulus *G*), with those forming part of the copper-jacketted specimen assembly treated as radially compound, as required. Segments immediately above and below the compliant part of the hollow steel elastic element, involving tapers in outer diameter between 37 and 16 mm diameter, were approximated as hollow cylinders of fixed outer diameter 37 and 16 mm, respectively. The set of nodes at either end of each segment was supplemented with additional nodes at ~ 10 mm spacing within the longer segments in order to facilitate plotting of the computed flexure at appropriate resolution. The linear static solver was used to compute the response, i.e. $v(x)$ and hence S_{mod}, to the application of unit bending moment at $x = l_3$ ($l_2 < l_3 < L$) with the appropriate boundary conditions (Section B.7).

B.3.3. Amplitude of the applied bending moment

The results of the numerical modelling can be combined with flexural-oscillation data to infer the amplitude M_a of the experimentally applied oscillating bending moment as follows. Numerical differentiation of the model deflection $v(x)$ yields the local angle of flexure, e.g. $v'(l_i)$ (i = 1, 2) for *unit* bending moment. The corresponding experimentally derived quantity d_i/D (i = 1, 2, eq. 1) is the response to a bending moment of unknown amplitude M_a. With the entirely reasonable assumption of linearity at low strain amplitudes, we obtain

$$M_a = d_i/Dv'(l_i). \qquad \text{(B.10)}$$

B.4 Results

B.4.1 Results for the Fused silica/Cu assembly I

Representative data, for 16 consecutive cycles of flexural oscillation at 1.28 s period, are shown in Fig. B.4a. The two time series represent the displacements $d_1(t)$ and $d_{12}(t) = d_2(t) - d_1(t)$ associated with the flexural mode distortions of the specimen assembly and elastic element, respectively. Their out-of-phase relationship reflects the fact that the displacements $d_1(t)$ and $d_2(t)$, measured by the transducer pairs above and below the elastic element, are out-of-phase. The implication is that the maximum deflection v of the propped, cantilevered beam, at which the angle of flexure v' changes sign, occurs within the elastic element. Fourier analysis of the time series is used to estimate the amplitude and phase of each of the sinusoidally time-varying displacements $d_i(t)$, and therefore also of their difference $d_{12}(t)$.

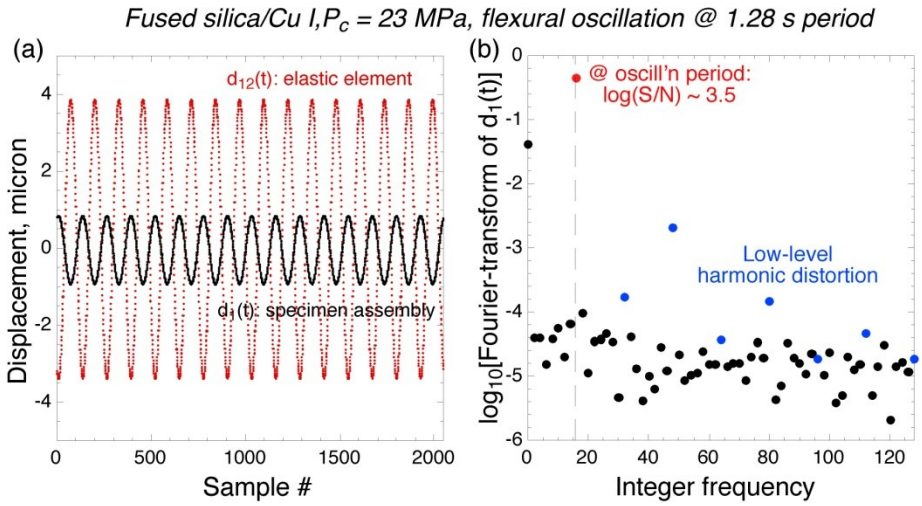

Figure B.4: Representative flexural oscillation results for the Fused silica/Cu assembly I (a) Time series representing the displacements $d_1(t)$ and $d_{12}(t) = d_2(t) - d_1(t)$ for 16 consecutive cycles of oscillation at 1.28 s period and 23 MPa confining pressure. (b) Plot against integer frequency of $\log_{10}$ of the modulus (absolute value) of the discrete Fourier transform of the raw (voltage versus time) data corresponding to $d_1(t)$ data in panel (a).

The Fourier transform plotted in Fig. B.4b shows that the signal amplitude at the driving frequency exceeds the background due to the 12-bit A/D quantisation by a factor of ~3000. The low level harmonic distortion also evident in the Fourier-transformed data is closely consistent on the two displacement channels – suggesting a common origin in non-linear conversion of coil current to force in the electromagnetic drivers.

Such flexural mode measurements have been performed on the Fused silica/Cu I specimen assembly (Fig. B.3) at oscillation periods between 1 and 100 s. As anticipated, the normalised flexural modulus S_{NF} is essentially independent of oscillation period (Fig. B.5a) and the loss angle δ is essentially zero (Fig. B.5b). These observations are

qualitatively consistent with the expectation of ideal elastic behaviour for pressures, and hence normal stresses at the interfaces within the assembly, sufficiently high to ensure effective mechanical coupling.

A more quantitative assessment of the experimental observations is provided by the results of the numerical modelling. Finite-difference calculations performed with progressively finer division of the length L of the beam into N intervals ($100 \leq N \leq 5000$) showed convergence of S_{mod} within 0.02 % for $N \geq 2000$, corresponding to an interval $h \leq$ 0.5 mm.

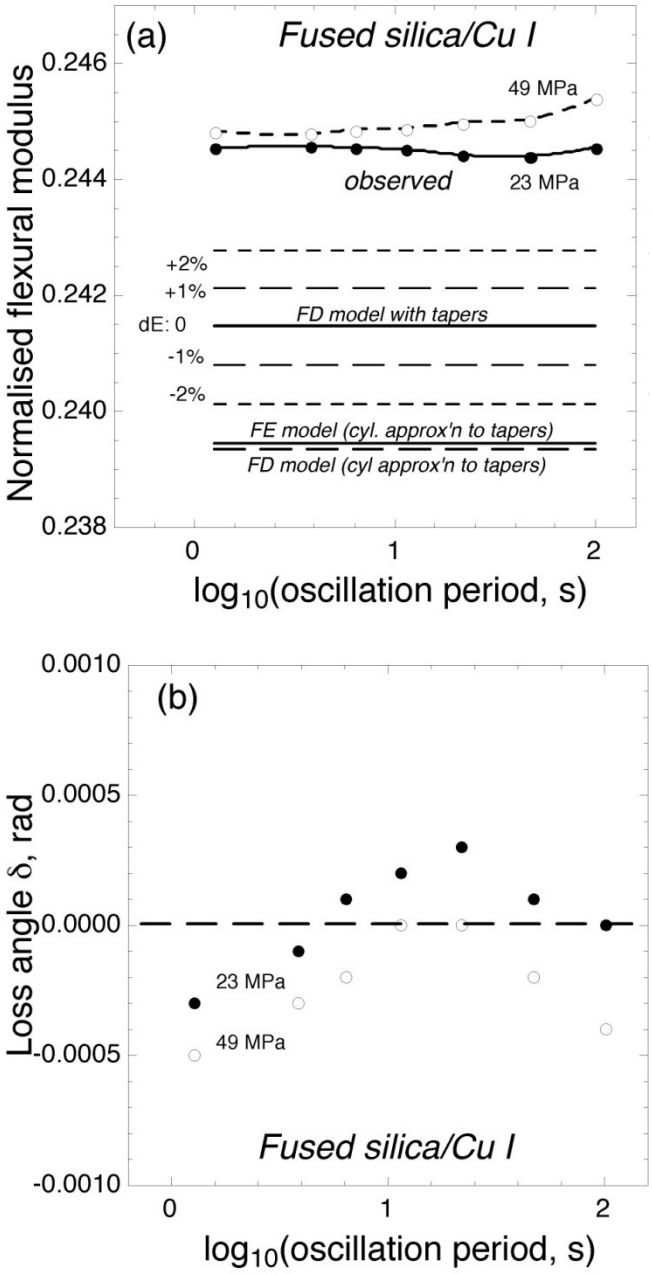

Figure B.5: The results of flexural-oscillation experiments on the Fused silica/Cu assembly I (Fig. B.3) at 23 MPa (with optimal transducer alignment, filled symbols) and at 49 MPa (inferior transducer alignment, open symbols). (a) Normalised flexural modulus S_{NF} versus oscillation period. Data indicated by the plotting symbols and interpolating curves are compared with the outcomes of the finite-difference (FD) and

finite-element (FE) modelling. For the finite-difference modelling of the assembly inclusive of tapers within the elastic element, the solid black line corresponds to the nominal value of the Young's modulus E (73.1 GPa) for fused silica and the broken lines to perturbations δE of ± 1 and ± 2%. For the assembly in which the tapers are approximated by uniform cylindrical segments (see text), the solid and dashed lines represent the results for the alternative finite-element and finite-difference models. (b) Loss angle δ (radian), being the phase lag between the distortion $d_{12}(t)$ of the elastic element and $d_1(t)$ of the specimen assembly.

With N = 2000 and a nominal value E = 73.1 GPa for fused silica [21], the calculated value of S_{mod} is 0.24145, with a sensitivity to the variation of the Young's modulus for fused silica of 9.0×10^{-4} GPa^{-1}, or 0.51% per % change in E). The finite-difference value of S_{mod} is thus 1.2% lower than the average 0.24449(3) of the experimental S_{NF} data at 23 MPa, obtained with near-optimal transducer alignment (Fig. B.5a).

In order to more tightly constrain the elastic properties of the fused silica control specimen, a disk of ~8 mm length was prepared from the recovered Fused silica/Cu assembly I, with faces ground and lapped parallel. The compressional and shear wave speeds, measured by phase comparison ultrasonic interferometry [22] at ~20 MHz, were V_P = 5.937(2) km s^{-1} and V_S = 3.766(2) km s^{-1}, respectively. With a density ρ of 2.2014(2) g cm^{-3} determined by immersion in ethanol, the Young's and shear moduli, E and G, were calculated to be 72.64(5) GPa, and 31.22(3) GPa, respectively – closely consistent with published data (73.1 and 31.2 GPa, respectively) [21].

The possibility that the small but significant discrepancy between measured S_{NF} and calculated S_{mod} might result from the neglect of shear stress in the filament elongation model implemented in the finite-difference calculation was tested through

the complementary finite-element modelling. The results of a finite-element calculation (in which the role of shear stress is explicitly included) are compared with the finite-difference solution $v(x)$ for the Fused silica/Cu I assembly in Fig. B.6. The close consistency between the plotted deflections strongly suggests that allowance for shear stresses contributes negligibly to the flexural stiffness of the beam. The finite-element value for S_{mod} of 0.23943, with the tapers approximated by segments of uniform diameter (as previously described), is closely comparable with the result (0.23933) of the N = 2000 finite-difference calculation for the *same* beam geometry (Fig. B.6). Moreover, finite-difference calculations indicate that the cylindrical approximation to the tapers reduces S_{mod} by 0.9% from 0.24145 to 0.23933. Taken together, these results suggest a finite-element value of S_{mod} for the *tapered* beam of 0.24155, indistinguishable from the result of the finite-element calculation, and 1.2% less than observed in the forced-oscillation experiments (Fig. B.5a).

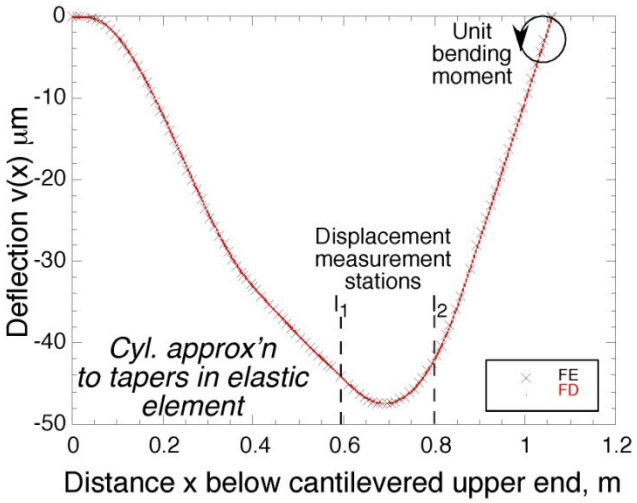

Figure B.6: A comparison of the results of the finite-difference (red symbols) and finite-element (black crosses) modelling, with the tapered segments of the elastic element approximated as hollow cylinders as described in the text. The deflection $v(x)$, induced by a bending moment of 1 Nm applied at $x = l_3$, is plotted as a function of the distance x from the cantilevered upper end of the beam. Displacement transducers measure the local angle of flexure at $x = l_1$ and $x = l_2$, respectively.

The approach outlined in the previous section has been used to infer an amplitude of 0.17 Nm for the bending moment applied in flexural oscillation of the Fused silica/Cu assembly I, and a maximum extensional strain amplitude ε_{xx} of 1.3×10^{-7}.

B.4.2 Results for the Fused silica/Cu assembly II

The sensitivities of the flexural-oscillation results to variation of the argon confining pressure and the magnitude of the oscillating bending moment were assessed

in a more comprehensive series of experiments on another fused silica/Cu assembly (assembly II of Fig. B.3).

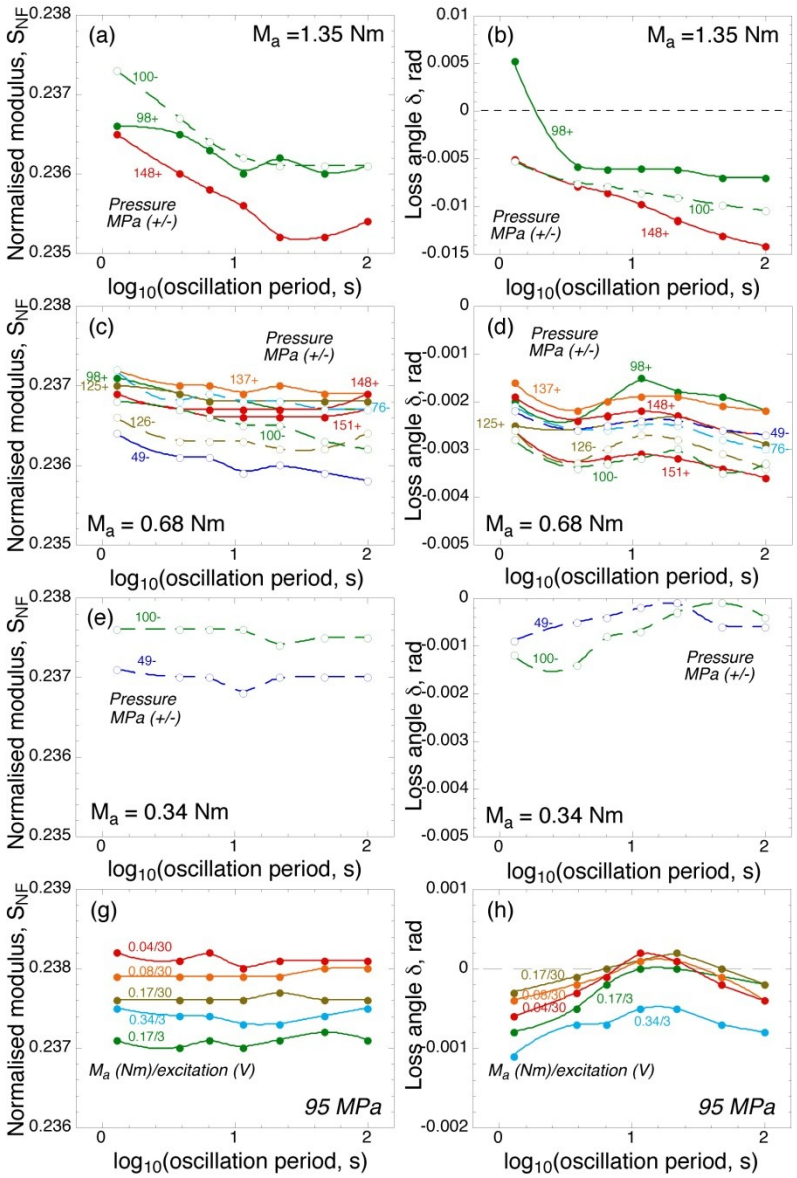

Figure B.7: Flexural-oscillation data for the Fused silica/Cu II assembly, demonstrating the sensitivities of the normalised flexural modulus S_{NF} and loss angle δ to variation of confining pressure and the amplitude of the oscillating bending moment. The symbol '+'

and '-' symbols associated with pressure, label data obtained during pressurisation and depressurisation, respectively. The pair of numbers associated with each curve in panels (g) and (h) represent the amplitude of the bending moment (Nm), and the AC bridge excitation voltage (V), respectively.

The geometry of Fused silica/Cu assembly II is only slightly different from assembly I (Fig. B.3), and accordingly, the values of S_{mod} calculated from the (N =2000) finite-difference models are also closely similar: 0.24378 and 0.24145, respectively. The flexural response experimentally observed for assembly II is also somewhat different than for assembly I, with values of S_{NF} tightly clustered in the range 0.235-0.238, and generally small values of δ ranging between -0.015 and +0.005 rad (Fig. B.7). The effect of pressure was most thoroughly examined with the amplitude of the applied bending moment fixed at 0.68 Nm. Neither S_{NF} nor δ varies significantly with pressure within the range 50-150 MPa (Fig. B.7c & d). However, there may be a measurable influence of the amplitude of the bending moment. For the lowest such amplitudes ($\leq$ 0.17 Nm), a period-independent value of S_{NF} of 0.237-0.238 is combined with a very small, but apparently systematically period-dependent, loss angle in the range -0.0008 < δ < 0.0002 rad (Fig. B.7g & h). For larger amplitudes of the bending moment, S_{NF} becomes somewhat lower (0.235-0.237) and $|\delta|$ somewhat higher (to 0.015 rad), and each of these quantities develops a significant dependence upon oscillation period (Fig. B.7 a-d).

B.5 Discussions/Conclusions

The generally close consistency between the experimentally determined values of the normalised flexural modulus S_{NF} and the corresponding quantity S_{mod} estimated by numerical modelling establishes the viability of the flexural-oscillation method at strain amplitudes as low as 10^{-7}. Failure to observe the stiffening expected of the inclusion of shear stress in the finite-element calculations is attributed to the fact that this effect would be greatest in the least compliant segments of largest diameter, located between the more compliant specimen and elastic element which dominate the overall flexural response of the experimental assembly.

The observed pressure independence of S_{NF} and the near-zero values of the loss angle δ indicate a close approach to perfectly elastic behaviour for each of the Fused silica/Cu test assemblies – suggesting, in particular, that the interfaces in the beam do not cause major complications.

The onset of significant sensitivity of S_{NF} and δ to the amplitude M_a of the bending moment for $M_a \geq 0.68$ Nm, coupled with systematic variations with oscillation period, may result from interaction between the flexing assembly and the dense and viscous argon pressure medium – especially the effect of subsidiary bending moments exerted on the assembly by the central transducer plates (Fig. B.1). Quantification of these effects is the subject of ongoing research. Another direction for future work is assessment of the influence of pressure on the flexural response of the experimental assembly though dimensional changes with their magnified influence on the moment of inertia.

Finally, on the basis of appropriate forward modelling of the flexure of the experimental assembly, we plan to develop a strategy for the inversion of the experimental data S_{NF} and δ for the complex Young's modulus associated with the poroelastic behaviour of cracked and fluid-saturated rocks and simpler synthetic analogues. However, before such inversion can be meaningful, it will be necessary to develop appropriate strategies for identification and modelling of the relaxation associated with specimen-scale fluid flow.

B.6 Acknowledgements

We thank Hayden Miller for assistance with the modifications of the forced-oscillation apparatus, and Zbigniew Stachurski for guidance in the numerical modelling.

B.7 Appendix

B.7.1 The finite-difference strategy for analysis of the filament-elongation model (equation B.3)

For the finite difference calculation, the length L of the entire experimental assembly, treated as a propped compound cantilever, is split into a series of N small intervals (x_{i-1}, x_i) $(i = 1, N)$ each of the same width h. The flexural rigidity $(EI)_i = E(x_i)I(x_i)$ and local bending moment $M_i = M(x_i)$ are specified at each of the x_i $(i = 0, N)$, and we wish to solve for the deflections $v_i = v(x_i)$. With the first and second derivatives of $v(x)$ approximated by the central differences

$$v'(x_i) = (v_{i+1} - v_{i-1})/2h$$

$$v''(x_i) = [(v_{i+1}-v_i)/h - (v_i-v_{i-1})/h]/h = (v_{i-1}-2v_i+v_{i+1})/h^2, \quad \text{(B.a1)}$$

the equations to be solved for the v_i are each of the form

$$v_{i-1} - 2v_i + v_{i+1} = -h^2 M_i/(EI)_i. \quad \text{(B.a2)}$$

The local bending moment $M_i = M(x_i)$ is related to the bending moment M_a applied at $x = l_3$ and the lateral reaction force R_L at the propped end ($x = L$), through an analysis of static equilibrium:

$$M_i = R_L(L - x_i) - M_a \text{ for } 0 \le x_i < l_3 \quad \text{(B.a3)}$$

and

$$M_i = R_L(L - x_i) \text{ for } l_3 < x_i \le L. \quad \text{(B.a4)}$$

The boundary conditions requiring zero deflection at either end of the beam imply that $v_0 = v(x_0) = v_N = v(x_N) = 0$. The further boundary condition

$$v'(x_0) = (v_1 - v_{-1})/2h = 0$$

requires that $v_{-1} = v_1$. Finally the use of $M_N = 0$ in eq. (A2) requires that

$$v_{N-1} - 2v_N + v_{N+1} = -h^2 M_N/(EI)_N = 0$$

so that $v_{N+1} = -v_{N-1}$. There remain N equations (eq. (A2) with $i = 0, N\text{-}1$) as follows.

The finite difference equation for $i = 0$ becomes

$$[h^2L/(EI)_0]R_L + 2v_1 = h^2M_a/(EI)_0. \quad \text{(B.a5)}$$

For arbitrary $i \geq 1$ such that $(0 \leq x < l_3)$,

$$[h^2(L\text{-}x_i)/(EI)_i]R_L + v_{i-1} - 2v_i + v_{i+1} = h^2M_a/(EI)_i. \quad \text{(B.a6)}$$

In particular, for $i = 1$, because $v_0 = 0$,

$$[h^2(L-x_1)/(EI)_1]R_L - 2v_1 + v_2 = h^2M_a/(EI)_1. \quad \text{(B.a7)}$$

For $l_3 < x \leq L$

$$[h^2(L-x_i)/(EI)_i]R_L + v_{i-1} - 2v_i + v_{i+1} = 0. \quad \text{(B.a8)}$$

In particular, for $i = N\text{-}1$, because $v_N = 0$,

$$[h^2(L-x_{N-1})/(EI)_{N-1}]R_L + v_{N-2} - 2v_{N-1} = 0 \quad \text{(B.a9)}$$

Thus, for given applied bending moment M_a, equations (A5-A9) constitute a set of N simultaneous linear equations (for i = 0, N-1) that were solved with Matlab^{TM} code for the N unknowns, being the v_i (i = 1, N-1) along with the statically indeterminate terminal reaction force R_L.

B.8 Endnotes

[1] J. B. Walsh. Journal of Geophysical Research, **74,** 4333 (1969).

[2] I. Jackson. Geol. Soc. Aust. Spec. Publ., **17,** 81 (1991).

[3] R. J. O'Connell & B. Budiansky. Journal of Geophysical Research, **82,** 5719 (1977).

[4] G. M. Mavko & A. Nur. J. Geophys. Res., **80,** 1444, (1975).

[5] J.W. Spencer. J. Geophys. Res., **86**, 1803 (1981).

[6] R.H. Cherry, H.A. Spetzler, H. & J. Paffenholz. Rev. Sci. Instrum. 67, 215 (1995).

[7] C. Lu & I. Jackson. Geophysics, **71,** 147, (2006).

[8] L. Adam, M. Batzle, K. T. Lewallen & K. van Wijk. Journal Geophysical Research, **114,** B06208, (2009).

[9] M. Adelinet, J. Fortin, Y. Gueguen, A. Schubnel & L. Geoffeoy. Geophysical Research Letters, **37,** L02303, (2010).

[10] I. Jackson & M. S. Paterson. PAGEOPH, **141,** 445 (1993).

[11] T. T. Gribb & R. F. Cooper. Rev. Sci. Instrum., **69,** 559 (1998).

[12] L. Li & D. J. Weidner. Rev. Sci. Instrum., **78,** 053902 (2007).

[13] J.E. White. *Geophysics 51*: 742-745 (1986).

[14] K.-J. Dunn. *J. Acoust. Soc. Am. 79*: 1709 (1986).

[15] K.-J. Dunn. *J. Acoust. Soc. Am. 81*: 1259 (1987).

[16] I. Jackson. *In The Australian Lithosphere*, *Geol. Soc. Aust. Spec. Publ. 17*: 81 (1991).

[17] P.A. Berge, B.P. Bonner & J. G. Berryman. *Geophysics 60*: 108 (1995).

[18] W. F. Brace, J. B. Walsh & W. T. Frangos. J. Geophys. Res., **73,** 2225 (1968).

[19] S. Zhang, M. S. Paterson & S. F. Cox. J. Geophys. Res., **99,** 15741 (1994).

[20] S. P. Timoshenko & J. M. Gere. 1973. *Mechanics of Materials*. (Van Nostrand Reinhold, London).

[21] G. W. C. Kaye & T. H. Laby. 1973. *Tables of physical and chemical constants and some mathematical functions*. (*Longman*, London).

[22] I. Jackson, H. Niesler & D. J. Weidner. J. Geophys**.** Res, **86,** 3736, (1981).

Bibliography

Adam, L., Batzle, M. & Brevik, L., 2006. Gassmann's fluid substitution and shear modulus variability in carbonates at laboratory seismic and ultrasonic frequencies, *Geophysics,* 71**,** F173-F183.

Adam, L., Batzle, M., Lewallen, K.T. & van Wijk, K., 2009. Seismic wave attenuation in carbonates, *Journal of Geophysical Research-Solid Earth,* 114**,** 14.

Adam, L. & Otheim, T., 2013. Elastic laboratory measurements and modeling of saturated basalts, *Journal of Geophysical Research-Solid Earth,* 118**,** 840-851.

Adelinet, M., Fortin, J., Gueguen, Y., Schubnel, A. & Geoffroy, L., 2010. Frequency and fluid effects on elastic properties of basalt: Experimental investigations, *Geophysical Research Letters,* 37**,** 4.

Auld, B.A., 1973. Acoustic fields and waves in solids, Wiley-Interscience Publication, New York, pp. 423.

Baechle, G.T., Eberli, G.P., Weger, R.J. & Massaferro, J.L., 2009. Changes in dynamic shear moduli of carbonate rocks with fluid substitution, *Geophysics,* 74**,** E135-E147.

Batzle, M.L., Han, D.H. & Hofmann, R., 2006. Fluid mobility and frequency-dependent seismic velocity - Direct measurements, *Geophysics,* 71**,** N1-N9.

Berge, P.A., Bonner, B.P. & Berryman, J.G., 1995. Ultrasonic velocity porosity relationships for sandstone analogs made from fused glass-beads, *Geophysics,* 60**,** 108-119.

Berryman, J.G., 1999. Origin of Gassmann's equations, *Geophysics,* 64**,** 1627-1629.

Biot, M.A., 1956. Theory of propagation of elastic wave in a fluid-saturated porous solid I. Low frequency range II. Higher frequency range, *Journal of the Acoustical Society of America,* 28**,** 168-191.

Birch, F., 1947. Finite elastic strain of cubic crystals, *Physical Review,* 71**,** 809-824.

Bouzidi, Y. & Schmitt, D.R., 2009. Measurement of the speed and attenuation of the Biot slow wave using a large ultrasonic transmitter, *Journal of Geophysical Research-Solid Earth,* 114.

Brace, W.F., Walsh, J.B. & Frangos, W.T., 1968. Permeability of granite under high pressure, *Journal of Geophysical Research,* 73**,** 2225-2236.

Brown, R.J.S. & Korringa, J., 1975. Dependence of elastic properties of a porous rock on compressibility of pore fluid, *Geophysics,* 40**,** 608-616.

Budiansky, B. & O'Connell, R.J., 1976. Elastic moduli of a cracked solid, *International Journal of Solids and Structures,* 12**,** 81-97.

Cadoret, T., 1993. Effet de la Saturation Eau/Gaz sur les Propriétés Acoustiques des Roches, Ph.D., University of Paris, VII.

Chapman, M., Zatsepin, S.V. & Crampin, S., 2002. Derivation of a microstructural poroelastic model, *Geophysical Journal International,* 151**,** 427-451.

Cherry, R.H., Spetzler, H.A. & Paffenholz, J., 1996. A new wideband (1 mHz to 100 Hz) seismic spectrometer, *Review of Scientific Instruments,* 67**,** 215-221.

Cholach, P.Y., Molyneux, J.B. & Schmitt, D.R., 2005. Flin Flon Belt seismic anisotropy: elastic symmetry, heterogeneity, and shear-wave splitting, *Canadian Journal of Earth Sciences,* 42**,** 533-554.

Crampin, S. & Lovell, J.H., 1991. A decade of shear-wave splitting in the Earth's crust: what does it mean? what use can we make of it? and what should we do next?, *Geophysical Journal International,* 107**,** 387-407.

Darcy, H., 1856. Les Fontaines Publiques de la Ville de DijonDalmont, Paris.

David, E.C., Fortin, J., Schubnel, A., Gueguen, Y. & Zimmerman, R.W., 2013. Laboratory measurements of low- and high-frequency elastic moduli in Fontainebleau sandstone, *Geophysics,* 78**,** D367-D377.

De, G.S., Winterstein, D.F. & Meadows, M.A., 1994. Comparison of P-wave and S-wave velocities and Qs from VSP and sonic long data, *Geophysics,* 59**,** 1512-1529.

Dey-Barsukov, S., Durrast, H., Rabbel, W., Siegesmund, S. & Wende, S., 2000. Aligned fractures in carbonate rocks: laboratory and in situ measurements of seismic anisotropy, *International Journal of Earth Sciences,* 88**,** 829-839.

Douma, J., 1988. The effect of the aspect ratio on crack-induced anisotropy, *Geophysical Prospecting,* 36**,** 614-632.

Dunn, K.J., 1986. Acoustic attenuation in fluid-saturated porous cylinders at low frequencies, *Journal of the Acoustical Society of America,* 79**,** 1709-1721.

Dunn, K.J., 1987. Sample boundary effect in acoustic attenuation of fluid-saturated porous cylinders, *Journal of the Acoustical Society of America,* 81**,** 1259-1266.

Duo, X., Schijns, H., Schmitt, D.R., Heinonen, S., Kukkonen, I.T. & Heikkinen, P., 2009. High Resolution VSP in Outokumpu, *SEG Expanded Abstracts*, Houston, United States, 25-30 Oct

Duo, X., Schijns, H., Schmitt, D.R., Heinonen, S., Kukkonen, I.T. & Heikkinen, P., 2010. High Resolution VSP in Outokumpu, *GeoCanada Expanded Abstracts*, Calgary, Canada, 10-14 May.

Dvorkin, J. & Nur, A., 1993. Dynamic poroelasticity - a unified model with the squirt and the Biot mechanisms, *Geophysics,* 58**,** 524-533.

Dziewonski, A.M. & Anderson, D.L., 1981. Preliminary reference Earth model, *Physics of the Earth and Planetary Interiors,* 25**,** 297-356.

Elbra, T., Karlqvist, R., Lassila, I., Haeggstrom, E. & Pesonen, L.J., 2011. Laboratory measurements of the seismic velocities and other petrophysical properties of the Outokumpu deep drill core samples, eastern Finland, *Geophysical Journal International,* 184**,** 405-415.

Eshelby, J.D., 1957. The determination of the elastic field of an ellipsoidal inclusion, and related problems, *Proceedings of the Royal Society of London Series a-Mathematical and Physical Sciences,* 241**,** 376-396.

Gassmann, F., 1951. Uber die elastizitat pososer medien, *Vier. der Natur. Gesellschaft,* 96**,** 1-23.

Geertsma, J. & Smit, D.C., 1961. Some aspects of elastic wave propagation in fluid-saturated porous solids, *Geophysics,* 26**,** 169-181.

Gerlich, D. & Kennedy, G.C., 1978. 2nd Pressure derivative of elastic-moduli of fused quartz, *Journal of Physics and Chemistry of Solids,* 39**,** 1189-1191.

Gieske, J.H. & Barsch, G.R., 1968. Pressure dependence of elastic constants of single crystalline aluminum oxide, *Physica Status Solidi,* 29**,** 121-&.

Grechka, V. & Kachanov, M., 2006a. Effective elasticity of fractured rocks: A snapshot of the work in progress, *Geophysics,* 71**,** W45-W58.

Grechka, V. & Kachanov, M., 2006b. Seismic characterization of multiple fracture sets: Does orthotropy suffice?, *Geophysics,* 71**,** D93-D105.

Gribb, T.T. & Cooper, R.F., 1998. A high-temperature torsion apparatus for the high-resolution characterization of internal friction and creep in refractory metals and ceramics: Application to the seismic-frequency, dynamic response of Earth's upper mantle, *Review of Scientific Instruments,* 69**,** 559-564.

Hajnal, Z., White, D.J., Takacs, E., Gyorfi, I., Annesley, I.R., Wood, G., O'Dowd, C. & Nimeck, G., 2010. Application of modern 2-D and 3-D seismic-reflection techniques for uranium exploration in the Athabasca Basin, *Canadian Journal of Earth Sciences,* 47**,** 761-782.

Hammer, P.T.C., Clowes, R.M., Cook, F.A., van der Velden, A.J. & Vasudevan, K., 2010. The Lithoprobe trans-continental lithospheric cross sections: imaging the internal structure of the North American continent, *Canadian Journal of Earth Sciences,* 47**,** 821-857.

Hashin, Z. & Shtrikman, S., 1962. A variational approach to the theory of the elastic behaviour of polycrystals, *Journal of the Mechanics and Physics of Solids,* 10**,** 343-352.

Hashin, Z. & Shtrikman, S., 1963. A variational approach to the theory of elastic wave behaviour of multiphase materials, *Journal of the Mechanics and Physics of Solids,* 11**,** 127-140.

Heinonen, S., Heikkinen, P.J., Kousa, J., Kukkonen, L.T. & Snyder, D.B., 2013. Enhancing hardrock seismic images: Reprocessing of high resolution seismic reflection data from Vihanti, Finland, *Journal of Applied Geophysics,* 93**,** 1-11.

Heinonen, S., Schijns, H., Schmitt, D.R., Heikkinen, P.J. & Kukkonen, I.T., 2009. High resolution reflection seismic profiling in Outokumpu. in Outokumpu Deep Drilling Project, 3rd International Workshop, pp. 17-21, ed Kukkonen, I. T. Geological Survey of Finland, unpublished report Q10.2/2009/61, Espoo, Finland.

Hill, R., 1952. The elastic behaviour of a crystalline aggregate, *Proceedings of the Physical Society of London Section A,* 65**,** 349-355.

Hsieh, P.A., Tracy, J.V., Neuzil, C.E., Bredehoeft, J.D. & Silliman, S.E., 1981. A transient laboratory method for determining the hydraulic properties of 'tight' rocks - I. Theory, *International Journal of Rock Mechanics and Mining Sciences,* 18**,** 245-252.

Hudson, J.A., 1980. Overall properties of a cracked solid, *Mathematical Proceedings of the Cambridge Philosophical Society,* 88**,** 371-384.

Hudson, J.A., 1981. Wave speeds and attenuation of elastic-waves in material containing cracks, *Geophysical Journal of the Royal Astronomical Society,* 64**,** 133-150.

Hudson, J.A., 1986. A higher-order approximation to the wave-propagation constants for a cracked solid, *Geophysical Journal of the Royal Astronomical Society,* 87**,** 265-274.

Hudson, J.A., 1994. Overall properties of anisotropic materials containing cracks, *Geophysical Journal International,* 116**,** 279-282.

Iwasaki, T., Tasuoka, F. & Takagi, Y., 1978. Shear moduli of sand under cyclic torsional shear loading, *Soils and Foundations,* 18**,** 39-56.

Jackson, I., 1991. The petrophysical basis for the interpretation of seismological models for the continental lithosphere, *Geological Society of Australia Special Publication,* 17**,** 81-114.

Jackson, I., Niesler, H. & Weidner, D.J., 1981. Explicit correction of ultrasonically determined elastic wave velocities for transducer-bond phase-shifts, *Journal of Geophysical Research,* 86**,** 3736-3748.

Jackson, I. & Paterson, M.S., 1993. A high-pressure, high-temperature apparatus for studies of seismic-wave dispersion and attenuation, *Pure and Applied Geophysics,* 141**,** 445-466.

Jackson, I., Paterson, M.S., Niesler, H. & Waterford, R.M., 1984. Rock anelasticity measurements at high-pressure, low strain amplitude and seismic frequency, *Geophysical Research Letters,* 11**,** 1235-1238.

Jackson, I., Schijns, H., Schmitt, D.R., Mu, J.J. & Delmenico, A., 2011. A versatile facility for laboratory studies of viscoelastic and poroelastic behaviour of rocks, *Review of Scientific Instruments,* 82.

Johnson, D.L. & Plona, T.J., 1982. Acoustic slow waves and the consolidation transition, *Journal of the Acoustical Society of America,* 72**,** 556-565.

Kaye, G.W.C. & Laby, T.H., 1973. *Tables of physical and chemical constants and some mathematical functions,* Longman, London.

Kern, H., Ivankina, T.I., Nikitin, A.N., Lokajicek, T. & Pros, Z., 2008. The effect of oriented microcracks and crystallographic and shape preferred orientation on bulk elastic anisotropy of a foliated biotite gneiss from Outokumpu, *Tectonophysics,* 457**,** 143-149.

Koivisto, E., Malehmir, A., Heikkinen, P., Heinonen, S. & Kukkonen, I., 2012. 2D reflection seismic investigations at the Kevitsa Ni-Cu-PGE deposit, northern Finland, *Geophysics,* 77**,** WC149-WC162.

Kovacs, A., Gorman, A.R., Buske, S., Schmitt, D.R., Eccles, J.D., Toy, V.G., Sutherland, R., Townend, J., Norris, R., Pooley, B., Cooper, J., Bruce, C., Smilie, M., Bain, S., Hellwig, O., Hlousek, F., Hellmich, J., Riedel, M. & Schijns, H., 2011. Imaging the Alpine Fault to depths of more than 2 km - Initial results from the 2011 WhataDUSIE seismic reflection profile, Whataroa Valley, New Zealand, Abstract #T11A-2283, American Geophysical Union Fall Meeting, San Francisco, 5-9 Dec.

Kuster, G.T. & Toksoz, M.N., 1974. Velocity and attenuation of seismic waves in 2 phase media: Part I. Theoretical formulations, *Geophysics,* 39**,** 587-606.

Lassila, I., Karlqvist, R., Elbra, T., Gates, F.K., Pesonen, L.J. & Haeggstrom, E., 2010. Ultrasonic velocity of the upper gneiss series rocks from the Outokumpu deep

drill hole, Fennoscandian shield - Comparing uniaxial to triaxial loading, *Journal of Applied Geophysics,* 72**,** 178-183.

Li, L. & Weidner, D.J., 2007. Energy dissipation of materials at high pressure and high temperature, *Review of Scientific Instruments,* 78.

Liner, C.L. & Fei, T.W., 2006. Layer-induced seismic anisotropy from full-wave sonic logs: Theory, application, and validation, *Geophysics,* 71**,** D183-D190.

Liu, L.G., 1993. Bulk moduli of SiO2 polymorphs: quartz, coesite and stishovite, *Mechanics of Materials,* 14**,** 283-290.

Lu, C., 1996. Shear mode anelasticity of thermally cracked and fluid-saturated rocks, Ph.D., Australian National University.

Lu, C. & Jackson, I., 1998. Seismic-frequency laboratory measurements of shear mode viscoelasticity in crustal rocks - II: Thermally stressed quartzite and granite, *Pure and Applied Geophysics,* 153**,** 441-473.

Lu, C. & Jackson, I., 2006. Low-frequency seismic properties of thermally cracked and argon-saturated granite, *Geophysics,* 71**,** F147-F159.

Lubbe, R., Sothcott, J., Worthington, M.H. & McCann, C., 2008. Laboratory estimates of normal and shear fracture compliance, *Geophysical Prospecting,* 56**,** 239-247.

Luschen, E., Bram, K., Sollner, W. & Sobolev, S., 1996. Nature of seismic reflections and velocities from VSP-experiments and borehole measurements at the KTB deep drilling site in southeast Germany, *Tectonophysics,* 264**,** 309-326.

Mackenzie, J.K., 1950. The elastic constants of a solid containing spherical holes, *Proceedings of the Physical Society of London Section B,* 63**,** 2-11.

Madonna, C. & Tisato, N., 2013. A new Seismic Wave Attenuation Module to experimentally measure low-frequency attenuation in extensional mode, *Geophysical Prospecting,* 61**,** 302-314.

Malehmir, A., Juhlin, C., Wijns, C., Urosevic, M., Valasti, P. & Koivisto, E., 2012. 3D reflection seismic imaging for open-pit mine planning and deep exploration in the Kevitsa Ni-Cu-PGE deposit, northern Finland, *Geophysics,* 77**,** WC95-WC108.

Martinez, J.M. & Schmitt, D.R., 2013. Anisotropic elastic moduli of carbonates and evaporites from the Weyburn-Midale reservoir and seal rocks, *Geophysical Prospecting,* 61**,** 363-379.

Mavko, G. & Jizba, D., 1991. Estimating grain-scale fluid effects on velocity dispersion in rocks, *Geophysics,* 56**,** 1940-1949.

Mavko, G. & Nur, A., 1975. Melt squirt in athenosphere, *Journal of Geophysical Research,* 80**,** 1444-1448.

Mavko, G., Mukerji, T. & Dvorkin, J., 2009. *The rock physics handbook: tools for seismic analysis of porous media,* 2nd edn, Vol., pp. Pages, University Press, Cambridge.

McSkimin, H.J., Andreatch, P. & Thurston, R.N., 1965. Elastic moduli of quartz versus hydrostatic pressure at 25 degrees and -195.8 degrees C, *Journal of Applied Physics,* 36**,** 1624-&.

Meister, R., Robertson, E.C., Werre, R.W. & Raspet, R., 1980. Elastic-moduli of rock glasses under pressure to 8 kilobars and geophysical implications, *Journal of Geophysical Research,* 85**,** 6461-6470.

Milkereit, B., Eaton, D., Wu, J., Perron, G., Salisbury, M., Berrer, E.K. & Morrison, G., 1996. Seismic imaging of massive sulfide deposits .2. Reflection seismic profiling, *Economic Geology and the Bulletin of the Society of Economic Geologists,* 91**,** 829-834.

Mukerji, T. & Mavko, G., 1994. Pore fluid effects on seismic velocity in anisotropic rocks, *Geophysics,* 59**,** 233-244.

Murphy, W.F., 1984. Seismic to ultrasonic velocity drift - intrinsic absorption and dispersion in crystalline rock, *Geophysical Research Letters,* 11**,** 1239-1242.

Neuzil, C.E., Cooley, C., Silliman, S.E., Bredehoeft, J.D. & Hsieh, P.A., 1981. A transient laboratory method for determining the hydraulic properties of 'tight' rocks - II. Application, *International Journal of Rock Mechanics and Mining Sciences,* 18**,** 253-258.

NIST, 2012. NIST Standard Reference Database 203 Web Thermo Tables (WTT) - Professional Edition.

Nye, J.F., 1985. *Physical Properties of Crystals*, Oxford Science Publications, Oxford.

O'Connell, R.J. & Budiansky, B., 1974. Seismic velocities in dry and saturated cracked solids, *Journal of Geophysical Research,* 79**,** 5412-5426.

O'Connell, R.J. & Budiansky, B., 1977. Viscoelastic properties of fluid-saturated cracked solids, *Journal of Geophysical Research,* 82**,** 5719-5735.

Ohno, I., Abe, M., Kimura, M., Hanayama, Y., Oda, H. & Suzuki, I., 2000. Elasticity measurement of silica glass under gas pressure, *American Mineralogist,* 85**,** 288-291.

Peselnick, L., Liu, H.P. & Harper, K.R., 1979. Observations of details of hysteresis loops in Westerly granite, *Geophysical Research Letters,* 6**,** 693-696.

Prioul, R. & Jocker, J., 2009. Fracture characterization at multiple scales using borehole images, sonic logs, and walkaround vertical seismic profile, *AAPG Bulletin,* 93**,** 1503-1516.

Pyrak-Nolte, L.J., Myer, L.R. & Cook, N.G.W., 1990. Transmission of seismic waves across single natural fractures, *Journal of Geophysical Research-Solid Earth and Planets,* 95**,** 8617-8638.

Reuss, A., 1929. Berechnung der Fliebgrenze von Mischkristallen aufgrund der Plastizitatsbedingung fur Einkristalle, *Z. Angew. Math. Mech.,* 9**,** 49-58.

Rice, J.R. & Cleary, M.P., 1976. Some basic stress diffusion solutions for fluid-saturated elastic porous-media with compressible constituents, *Reviews of Geophysics,* 14**,** 227-241.

Saenger, E.H., Kruger, O.S. & Shapiro, S.A., 2004. Effective elastic properties of randomly fractured soils: 3D numerical experiments, *Geophysical Prospecting,* 52**,** 183-195.

Sahay, P.N., 2008. On the Biot slow S-wave, *Geophysics,* 73**,** N19-N33.

Sams, M.S., Neep, J.P., Worthington, M.H. & King, M.S., 1997. The measurement of velocity dispersion and frequency-dependent intrinsic attenuation in sedimentary rocks, *Geophysics,* 62**,** 1456-1464.

Schijns, H., Duo, X., Schmitt, D.R., Kukkonen, I.T. & Heikkinen, P., 2009a. ICDP Outokumpu Borehole Seismic Anisotropy: Measurements and Theoretical Model, *Outokumpu Deep Drilling Project: 3rd International Workshop Programme and Abstracts*, Espoo, Finland, 12-13 Nov.

Schijns, H., Heinonen, S., Schmitt, D.R., Heikkinen, P. & Kukkonen, I.T., 2009b. Seismic refraction traveltime inversion for static corrections in a glaciated shield rock environment: a case study, *Geophysical Prospecting,* 57**,** 997-1008.

Schijns, H., Schmitt, D.R., Heikkinen, P. & Kukkonen, I.T., 2010. Anisotropy of Fractured Mica-rich Schist from Outokumpu, Finland: VSP Measurements, Laboratory Measurements and Theoretical Model, *SEG Expanded Abstracts*, Denver, United States, 17-22 Oct.

Schijns, H., Schmitt, D.R., Heikkinen, P. & Kukkonen, I.T., 2013. Seismic anisotropy in cracked crystalline rock from Outokumpu, Finland, *ASEG Extended Abstracts*, Melbourne, Australia, 11-14 Aug.

Schijns, H., Schmitt, D.R., Heikkinen, P.J. & Kukkonen, I.T., 2012. Seismic anisotropy in the crystalline upper crust: observations and modelling from the Outokumpu scientific borehole, Finland, *Geophysical Journal International,* 189**,** 541-553.

Schijns, H., Schmitt, D.R., Kukkonen, I.T. & Heikkinen, P., 2009c. Seismic Anisotropy Measurements and Theoretical Model of Fractured Rock Using Multi-Depth Multi-Azimuth Walk-Away VSP from Outokumpu, Finland, *SEG Expanded Abstracts*, Houston, United States, 25-30 Oct.

Schijns, H., Schmitt, D.R., Kukkonen, I.T. & Heikkinen, P., 2009d. Seismic Anisotropy Measurements from the ICDP Outokumpu Borehole Compared to Theoretical Model, Abstract #GA21A-01, *Joint Assembly of the American Geophysical Union*, Toronto, Canada, 24-27 May.

Schmitt, D.R., 1999. Seismic attributes for monitoring of a shallow heated heavy oil reservoir: A case study, *Geophysics,* 64**,** 368-377.

Schoenberg, M., 1980. Elastic wave behaviour across linear slip interfaces, *Journal of the Acoustical Society of America,* 68**,** 1516-1521.

Schoenberg, M. & Douma, J., 1988. Elastic wave propagation in media with parallel fractures and aligned cracks, *Geophysical Prospecting,* 36**,** 571-590.

Schoenberg, M. & Sayers, C.M., 1995. Seismic anisotropy of fractured rock, *Geophysics,* 60**,** 204-211.

Schreiber, E. & Anderson, O.L., 1965. Pressure derivatives of sound velocities of polycrystalline alumina (Lucalox), *American Ceramic Society Bulletin,* 44**,** 637-&.

Simmons, G. & Wang, H., 1971. *Single crystal elastic constants and calculated aggregate properties: a handbook,* 2nd edn, Vol., pp. Pages, The MIT Press.

Smithson, S.B., Wenzel, F., Ganchin, Y.V. & Morozov, I.B., 2000. Seismic results at Kola and KTB deep scientific boreholes: velocities, reflections, fluids, and crustal composition, *Tectonophysics,* 329**,** 301-317.

Smyth, J.R. & McCormick, T.C., 1995. Crystallographic data for minerals. *in Mineral Physics and Crystallography, A Handbook of Physical Constants*, pp. 1-17, ed. Ahrens, T. J. AGU, Washington.

Spencer, J.W., 1981. Stress relaxations at low-frequencies in fluid-saturated rocks – attenuation and modulus dispersion, *Journal of Geophysical Research,* 86**,** 1803-1812.

Timoshenko, S.P. & Gere, J.M., 1973. *Mechanics of Materials,* Van Nostrand Reinhold, London.

Tittmann, B.R., Bulau, J.R. & Abdelgawad, M., 1984. Dissipation of elastic waves in fluid saturated rocks, *AIP Conference Proceedings***,** 131-143.

Voigt, W., 1928. Lehrbuch der KristallphysikTeubner-Verlag, Leipzig, Germany.

Walsh, J.B., 1965a. Effect of cracks on compressibility of rock, *Journal of Geophysical Research,* 70**,** 381-389.

Walsh, J.B., 1965b. Effect of cracks on uniaxial elastic compression of rocks, *Journal of Geophysical Research,* 70**,** 399-411.

Walsh, J.B., 1969. New analysis of attenuation in partially melted rock, *Journal of Geophysical Research,* 74**,** 4333-4337.

Watt, J.P. & Peselnick, L., 1980. Clarification of the Hasin-Shtrikman bounds on the effective elastic moduli of polycrystals with hexagonal, trigonal, and tegragonal symmetries, *Journal of Applied Physics,* 51**,** 1525-1531.

White, J.E., 1986. Biot-Gardner theory of extensional waves in porous rods, *Geophysics,* 51**,** 742-745.

White, D.J. & Malinowski, M., 2012. Interpretation of 2D seismic profiles in complex geological terrains: Examples from the Flin Flon mining camp, Canada, *Geophysics,* 77**,** WC37-WC46.

Winkler, K. & Nur, A., 1979. Pore fluids and seismic attenuation in rocks, *Geophysical Research Letters,* 6**,** 1-4.

Winkler, K.W. & Nur, A., 1982. Seismic attenuation - effects of pore fluids and frictional sliding, *Geophysics,* 47**,** 1-15.

Winkler, K.W., 1986. Estimates of velocity dispersion between seismic and ultrasonic frequencies, *Geophysics,* 51**,** 183-189.

Worthington, M.H. & Lubbe, R., 2007. The scaling of fracture compliance. *in Fractured Reservoirs*, pp. 73-82, eds. Lonergan, L., Jolly, R. J. H., Rawnsley, K. & Sanderson, D. J.

Yin, C.S., Batzle, M.L. & Smith, B.J., 1992. Effects of partial liquid gas saturation on extensional wave attenuation in Berea sandstone, *Geophysical Research Letters,* 19**,** 1399-1402.

Zhang, S.Q., Paterson, M.S. & Cox, S.F., 1994. Porosity and permeability evolution during hot isostatic pressing of calcite aggregates, *Journal of Geophysical Research-Solid Earth,* 99**,** 15741-15760.